Volume 2 Issue 2 · 2016
ISSN-2382-641X(print) ISSN-2382-6401(online)

JOURNAL OF SMART CITIES

Editor-in-chief:

Andreas J. Kappos
City, University of London

URBAN DEVELOPMENT SCIENTIFIC PUBLISHING PTE. LTD.

Editorial Board

Volume 2 Issue 2 • 2016 • ISSN-2382-641X(print)
ISSN-2382-6401(online)

Journal of Smart Cities

Editor-in-Chief

Andreas J. Kappos

City University London, United Kingdom

URBAN DEVELOPMENT SCIENTIFIC

PUBLISHING PTE.LTD.

2016 | Volume 2 | Issue 2 | Page: 1-90

Journal of Smart Cities

https://www.udspub.com/ajj/public/index.php/jsc

Contents

REVIEW ARTICLE

Intelligent concrete with self-x capabilities for smart cities

Xin Wang[1], Zhen Li[1], Bing Han[1], Baoguo Han[1*], Xun Yu[2,3], Shuzhu Zeng[1] and Jinping Ou[1,4]

[1] School of Civil Engineering, Dalian University of Technology, Dalian, 116024 China
[2] Department of Mechanical Engineering, New York Institute of Technology, New York, 11568, USA
[3] School of Machinery and Automation, Wuhan University of Science and Technology, Wuhan, 430081 China
[4] School of Civil Engineering, Harbin Institute of Technology, Harbin, 150090 China

Abstract: Intelligent concrete refers to the structural materials which can sense the changes of environment and make suitable responses by altering one or more working parameters in real time. The 'intelligent' properties of concrete are achieved mainly by improving the composition of raw materials or combining some functional materials with concrete matrix, thus leading to the concrete possessing bionic features. Compared to conventional concrete, a properly designed intelligent concrete can be applied to optimize the safety, longevity and function of infrastructures and reduce the life-cycle costs, resource consumption and environment pollution, which will lay a material foundation for building smart cities. In the past few decades, considerable efforts have been put towards the research of intelligent concrete and many innovative achievements have been gained in the development and application of intelligent concrete. Thirteen types of intelligent concrete emphasizing on its self-x capabilities are systematically reviewed in this paper, with attentions to their principles, composition, fabrication, properties, research progress and structural applications. In addition, some comments and prospects for the development of self-x concrete are also discussed.

Keywords: intelligent concrete; self-x capacity; principle; properties; structural applications

*Correspondence to: Baoguo Han, School of Civil Engineering, Dalian University of Technology, Dalian, 116024 China; E-mail: hithanbaoguo@163.com, hanbaoguo@dlut.edu.cn

Received: October 25, 2016; **Accepted:** November 16, 2016; **Published Online:** December 15, 2016

Citation: Wang X, Li Z, Han B, *et al*.,2016, Framing a satellite based asset tracking (SPARTACUS) within smart city technology. *Journal of Smart Cities*, vol.2(2): 1–39. http://dx.doi.org/10.26789/JSC.2016.02.005.

1. Introduction

Since the appearance of Portland cement in 1824, concrete has become the most widely used building materials in the infrastructure construction for its low cost, high compressive strength and extensive adaptability[1]. However, the mechanical properties in terms of toughness, tensile strength and impact resistance of concrete are extremely weak due to its quasi-brittle nature. Meanwhile, the obvious discreteness of raw materials and the complexity of environment conditions lead to the reliability of concrete structures challenged in service. Under the effect of load, temperature, humidity and other factors, the concrete materials are inclined to crack and failure. After a series of engineering disasters caused by material failures in the 1970s and 1980s, researchers realized that the security and reliability of structures may be significantly improved if materials have the capacities of self-sensing, self-adjusting and self-healing to monitor and repair the potential defects. Therefore, the occurrence of catastrophic accidents can be reduced and even avoided. Since then, the intelligent materials, which is defined as 'a material with the function of sensible and controllable to the variation of environment', was developed[2]. And the primary working proce-

sses of the intelligent concrete are illustrated in Figure 1.

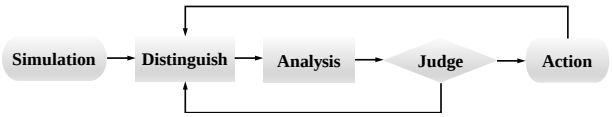

Figure 1. Information flow of intelligent concrete[3]

To date, extensive researches have been performed on various intelligent concretes[4]. The composition, proceeding, property and mechanism, measurement and application of intelligent concretes were widely investigated by experimental study, theoretical analysis and numerical simulation. This paper reviews the research achievements of intelligent concrete, focusing on its principles, properties, research progress and structural applications. Although intelligent concrete has more than ten categories of smart capacity, this review is only focused on the progress in concrete with self-x capabilities, *i.e.*, possessing intrinsically intelligent capabilities as shown in Figure 2. Among the 13 self-x concrete, the first six kinds are the common intelligent concrete written by the order of fabrication, curing and hardened properties. The subsequent seven kinds self-x concrete are the recently developed ones.

2. Self-Compacting Concrete

Self-compacting concrete (SCC) is also named as self-consolidating concrete, self-leveling concrete or vibration free concrete. The prototype of SCC was originally completed by Okamura in 1986. SCC has the advantages of high liquidity, no segregation and bleeding phenomenon compared with traditional concrete. SCC not only has the good ability to go through the space among steel rebars, but also has the ability of levelling under its own gravity which could make compacting concrete structure by itself. Besides, it could have a shorter construction period to enhance efficiency because of the uselessness for vibration[5-7].

Contrast between the mix proportion of SCC and that of conventional concrete is shown in Figure 3[8]. In order to test whether the mix proportion of the concrete is appropriate, some test methods such as U-flow test method, box test method, V-funnel test method and T500 test method were developed. In the U-flow test method as shown in Figure 4, the height that the concrete flowing through the obstacle can represent the degree of compactability of the concrete. If the concrete can flow through a height over 320 mm, the concrete can be judged as SCC. The box test method is appropriate for testing concrete which has higher segregation between mortar and aggregate. If the concrete s determined to have inadequate self-compactability, the mix proportion of the concrete has to be re-iadjusted.

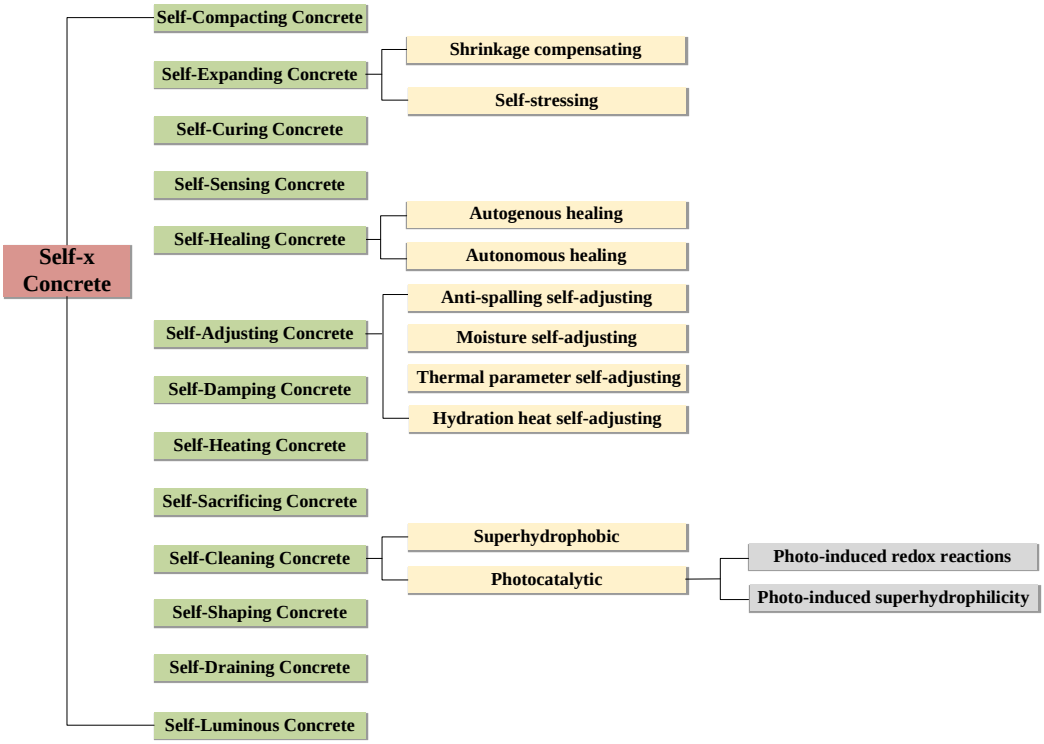

Figure 2. Categories of self-x concrete

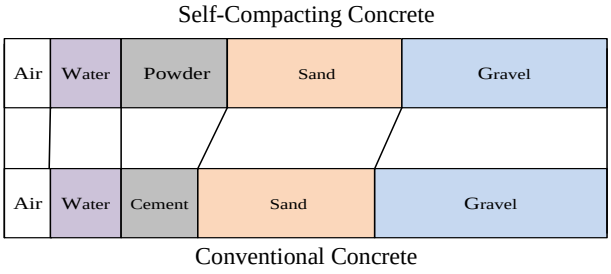

Figure 3. Contrast between the mix proportion of SCC and that of conventional concrete[8]

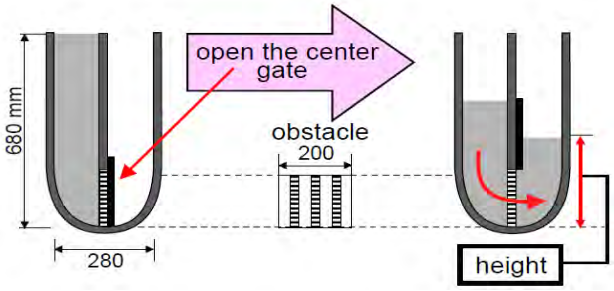

Figure 4. U-flow test[8]

The performance index of SCC is proposed in the Standardization Institute of Chinese Construction Standard 'SCC Application Specification' as shown in Table 1[9].

Table 1. Performance index of SCC

Performance Level	First Class	Second Class	Third Class
Rising height of U-flow/mm	above 320 (Ⅰ barrier)	above 320 (Ⅱ barrier)	above 320 (barrier-free)
Slump flow/mm	650–750	600–700	550–650
T500/s	5–20	3–20	3–20
Time for go through V-funnel/s	10–25	7–25	4–25

The optimal ratio of self-compacting concrete is mainly determined via a large number of orthogonal experiments. The main design properties of the SCC also include compressive strength, tensile strength, elastic modulus, heat of hydration, durability, creep, shrinkage and stiffness[5]. Persson[10] compared the elastic modulus, creep and shrinkage of the SCC with that of traditional concrete after performing a series of studies on strength (fc), and found there is no great difference between them. Nagamoto *et al.* found that the physical properties of the solids in the mortar can greatly affect the decrease extent of the shear deformation in the mortar. The SCC may bring a loss of compaction due to the increasing of the coarse aggregate content above the range G/Glim = 0.50. The relationship between the decrease in compaction and the increase in coarse aggregate is not linear. When the proportion of coarse aggregate to fine aggregate is varied, the amount of super-plasticizer is needed to be adjusted[11]. In addition, it has been proven by many researchers that the SCC is much better than ordinary concrete in durability.

SCC includes a diverse range of mix types with both fresh and hardened properties. It has higher filling rate, better deformability and higher segregation resistance compared with conventional concrete. However, there are still some issues needed to be addressed. For example, the early-age shrinkage of the SCC is large due to low water-binder ratio. This leads to the appearance of cracks. SCC would put great pressure on molds due to its liquidity. In addition, SCC is easier to spall than conventional concrete when it is subjected to high temperature.

3. Self-Expanding Concrete

Volume shrinkage would occur during the hydrating and hardening of Portland cement concrete. Micro-cracks will then generate in consequence of this shrinkage. This is detrimental to hardened concrete. Contrasting to ordinary concrete, expansion instead of shrinkage will appear in self-expanding concrete. Hence, the deficiencies caused by shrinkage can be overcome by the expansion. Normally, self-expanding concrete is divided into the shrinkage compensating concrete and the self-stressing concrete according to its expansive energy. Shrinkage compensating concrete is the concrete which expands to some extent intrinsically to prevent shrinkage cracking. Compared with shrinkage compensating concrete, self-stressing concrete possesses a bigger expansion capacity. It can produce a compressive stress of 2.0–8.0 MPa when the concrete expansion is restrained felicitously by reinforcement or other means.

Self-expanding concrete is mainly fabricated by using expansive constituents such as expansive cements or expansive additives. The expansion ability of concrete is largely depended on the dosage and activity of expansive constituents. Detailed information on the various expansive cements and expansive additives is summarized in Table 2. By mixing original minerals into Portland cement during the process of clinker manufacturing, expansive cement is produced and specified into three types by ASTM (*i.e.*, K, M, and S) according to the different original minerals[12]. On the other hand, for the sake to conveniently adjust

Table 2. Summary of expansive cement and expansive additive

Expansive constituent	Type	Original mineral	Expansion resources
Expansive cement	K	Monosulfate, gypsum, lime	Ettringite
	M	Aluminate clinker and gypsum	Ettringite
	S	Tricalcium aluminate and gypsum	Ettringite
Expansive additive	Calcium sulphoaluminate-based	Sulfoaluminate	Ettringite
	CaO-based	Calcia	Portlandite
	MgO-Based	Magnesia	Brucite
	Air-entraining-based	Iron or aluminum powder, oxidant	Hydrogen, ferrous hydroxide

expansion capacity, expansive mineral are separately produced from cement clinker and then directly mixed into concrete as an expansive additive. Expansion resources of expansive cement and calcium sulphoaluminate-based additive mainly come from the hydration product of acicular ettringite crystals. This kind of self-expanding concrete is the most widely used for the chemical stability of ettringite[13]. CaO-based and MgO-based expansive additives have the merits of low hydration water requirements and high volume expansion ratio. The translation of Calcia (CaO) into Portlandite [$Ca(OH)_2$] results in a volume augmented of 94% in theory, and 97.9% for Magnesia (MgO) becoming Brucite [$Mg(OH)_2$]. Of the two oxides, CaO is intrinsically more reactive compared with MgO. Furthermore, the hydration product of $Ca(OH)_2$ is more soluble than that of $Mg(OH)_2$[14].

Self-expanding concrete has a history of almost eighty years since the invention of expansive cement in 1936, France. It has been demonstrated that self-expanding concrete is a perfect alternative to increase the durability for both new constructions and refurbishment[15]. Shrinkage compensating concrete can effectively mitigate the cracks caused by thermal shrinkage, drying shrinkage and creep. Moreover, the filling effect of expansion products contributes to decreasing porosity and pore diameter, thus improving the density of concrete. Therefore, the major application of shrinkage compensating concrete is in water proofing constructions. Self-stressing concrete is mandatory in the conditions of dense rebar reinforcement or concrete confined in steel tubes, where a large amount of expansion restrained is required. In this way, interfacial bounding strength between concrete and reinforcement is increased and the tensile strength of concrete is substantially elevated[16]. Besides, enhancement of self-stressing capability is found to be achievable by adding fibers to confine the expansion of concrete. In this case, triaxial self-stressing developed by the fiber is beneficial to the enhancement of tensile strength as well as the impact and fatigue resistance of concrete[17]. Recently, hybrid fibers together with MgO expansion additive (MEA) are applied to improve the volume stability of concrete airport runway in high altitude localities in Tibet, China. Results indicate a decreasing expansion of concrete with the increasing content of steel fiber (SF) and fine denier polyacrylonitrile fiber (SP). As shown in Figure 5a, the volume stability of concrete slabs is improved at an early age. Microstructure analysis by scanning electron microscope illustrates that the micro-cracking inside concrete is locally restrained by the surrounding hybrid fibers, as graphed in Figure 5b[18].

Self-expanding concrete is an efficient substitute to improve some structural behaviors of concrete. However, expansion of concrete caused by the formation of ettringite consumes a large amount of water, which is

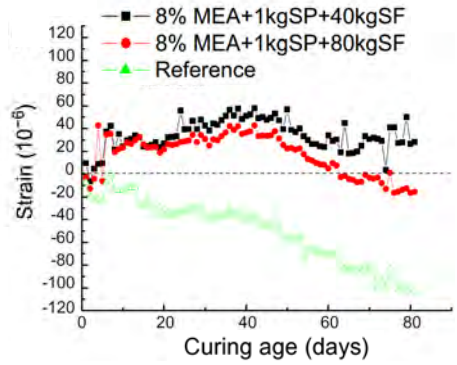

(A)

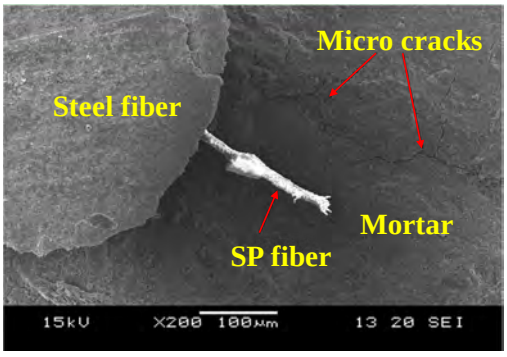

(B)

Figure 5. (a) Strain deformations of concrete added with hybrid fiber; (b) Microstructure of hybrid fiber inside of concrete[18]

strongly reliant on the wet curing[13]. Additionally, ettringite may undergo decomposition at high temperature (over 70 °C), and thus may be unsuitable for mass concrete with high temperature rise[19,20]. Due to the fast hydration of CaO and the relatively high solubility of hydration product $Ca(OH)_2$, the application of CaO-based expansive additive in the concrete for hydraulic structures is forbade[14]. For MgO-based expansive additive, the calcination temperature is a crucial condition for the hydration reactivity of MgO[21]. Once the calcine temperature is higher than needed temperature, dead-burnt MgO may be produced. This may cause heterogeneous expansion, and even lead to the destruction of concrete structure[22-24]. In a word, the negative effect of concrete expansion is required for deep investigation and choosing the effective self- expanding concrete based on the practical engineering demands is extremely important.

4. Self-Curing Concrete

Curing of concrete is essential immediately after the casting of concrete because of potential shrinkage, settlement and thermal deformation at early ages. Properly curing is significant for concrete to satisfy the requirements of mechanical properties and durability. Traditional curing methods like ponding, spraying, covering wet burlap or plastic films are adequate for ordinary concrete. However, these curing techniques may fail in high-performance concrete (HPC). HPC is characterized by low water binder ratio (w/b) and high volume additives such as silica fume, which leads to high strength and density at early age. In this condition, the penetration of external water is difficult and only superficial by traditional curing mode. Consequently, with inherent water insufficient and outer curing water inaccessible to satisfy complete hydration of binder, a series of chemical shrinkage and thereby autogenous shrinkage may cause serious premature crack. This premature crack finally induces the degradation of mechanical properties and durability. Considering these issues, self-curing as a new technology adapting to concrete with low w/b is presented.

Self-curing concrete also known as autogenous curing or internal curing concrete is achieved by incorporating pre-saturated component as internal curing agent. The curing agent is uniformly distributed throughout the matrix and acts as an internal water reservoir. The water within curing agent does not participate in the chemical reaction until a humidity gradient generates after a period of early hydration. Water is transported from curing agent to unhydrated cement by the driving forces of capillary suction, vapor diffusion and capillary condensation for supporting continuous hydration. As a result, the chemical shrinkage and self-desiccation caused by low w/b can be considerably diminished.

The self-curing agent should possess both high water absorption capacity in aqueous solution and desorption rates under pressure. Currently, the most popular curing agents are pre-saturated porous lightweight aggregates (LWA) and super absorbing polymers (SAP). LWA such as ceramsite and pumice is the first used self-curing agent, which typically contains water by weight of 5% to 25%[25]. SAP is described as ‘super’ for its ultra-high water adsorption capacity, which even 1000 times higher than its own weight[26]. The two distinct phases of SAP in dry and swollen are shown in Figure 6.

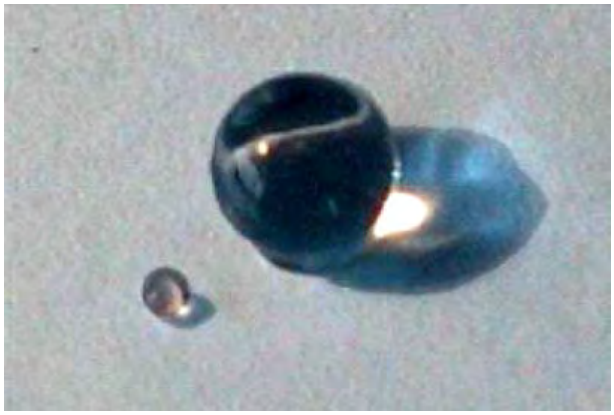

Figure 6. A dry and a swollen SAP[26]

Extensive attention has been attracted to the self-curing concrete in recent half a century and most investigations are conducted based on Powers' model, as illustrated in Figure 7[27,28]. The model systematically expounds the minimal dose of self-curing water needed

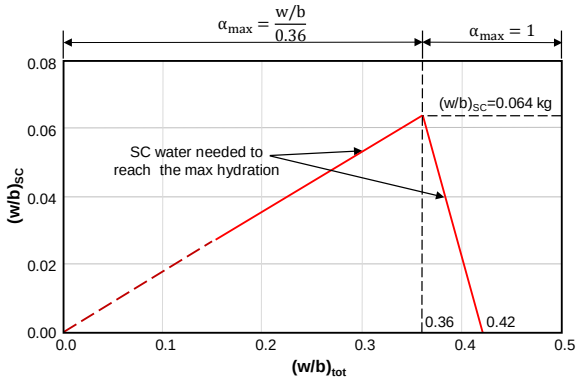

Figure 7. Minimum amount of self-curing water needed to obtain α_{max} during cement hydration

to reach the maximum degree of binder hydration (α_{max}) at a given w/b. As can be seen in Figure 7, α_{max} reaches up to the region of 1.0 (*i.e.*, full hydration of binder) only with w/b equal to or greater than 0.36. Below this value, binder hydration is only partially achieved and the α_{max} under saturated condition is estimated as (w/b)/0.36. Also indicated in Figure 7, fully saturated condition of binder hydration can be achieved with a quantity of self-curing water of 0.064 kg per kilogram of binder.

As mentioned previously, the w/b is generally between 0.30 and 0.40 for HPC. The detrimental deformation caused by autogenous shrinkage can be eliminated through self-curing technology. Here HPC with w/b of 0.30 is employed as an example to elaborate the effect of self-curing agent on the performance of HPC on the basis of Powers' model[29]. In Figure 8(a), at w/b of 0.30 and self-curing water removed, hydration stops at a degree of 0.73 under sealed curing conditions due to the water shortage. Figure 8(b) shows the mixture provided by an extra self-curing water of 3.20% by total water volume to the system. The water in curing agent is then drawn out 'filling the pores' created by chemical shrinkage and proceeds further hydration to 0.77. Once 7.36% water is replenished, hydration degree can reach up to 0.83 and the chemical shrinkage is totally eliminated as illustrated in Figure 8(c). The maximum theoretical degree of hydration increases with the volume of self-curing water, but comes to a limiting value at 7.36% as illustrated in Figure 8(d). This is because that at the hydration degree of 0.83, nearly no void space remains within the hydrating concrete. Therefore, the optimum self-curing water contents is of utter importance for the desired performance of concrete.

In recent twenty years, most investigations indicated that the autogenous shrinkage of concrete was reduced to some extent owing to the incorporation of self-curing agent[26,30-34]. Nevertheless, there are still conflicting results in mechanical properties. Some experiments show an increase in a range of 10%–20% compressive strength of concrete with self-curing agent than that without at 28 d, while others manifest a decrease of 8%–31%[30-36]. This difference may be attributed to the opposite effect of self-curing water. On the one hand, the incorporated self-curing water can improve the degree of binder hydration. On the other hand, excessive self-curing water may result in spherical macropores. Once the negative effect of self-curing water cannot compensate by the positive effect, the mechanical properties

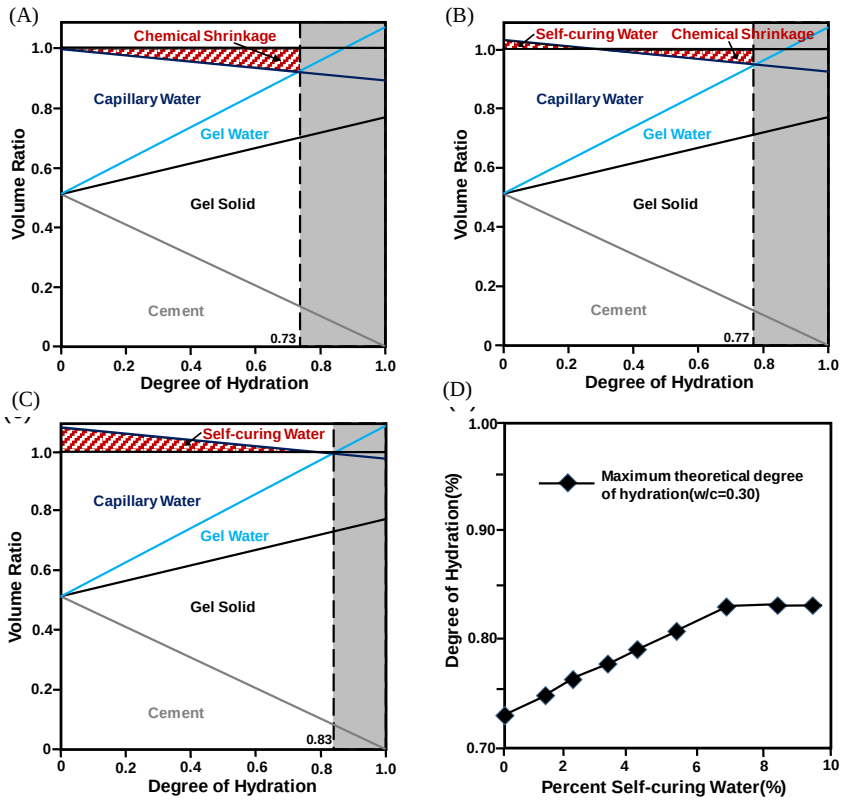

Figure 8. Powers' model showing phase distributions for (a) w/b=0.30 paste (b) 3.20% self-curing water and (c) 7.36% self-curing water. (d) Maximum theoretical degree of hydration as a function of self-curing water[29]

of concrete decreased[37]. Additionally, most findings illustrated an increasing durability of concrete by means of self-curing. For instance, the chloride permeability of concrete goes down contributed by the reduced percolation of interfacial transition zone between cement paste and aggregate[38-40]. The freezing and thawing resistance of concrete can also be improved due to the pores and air voids forming in the matrix after self-curing agent becomes dry[41-43].

Self-curing concrete accompanied with well-designed mechanical properties and outstanding durability has been employed in engineering applications. In January 2005, about 190000 m^3 of self-cured HPC with presoaked LWA was successfully casted in a large railway transit yard in Texas, America. After placing, the flexural strength at 7 d reached 90% to 100% of those required at 28 d as a consequence of improved cement hydration process[44]. Additionally, shrinkage cracks are extremely minimal compared with conventional paving concrete. In 2010, self-curing concrete was used in the construction of 9 bridges by New York Department of Transportation. A special mixture design, which is similar to the one of conventional deck design except for the extra 120 kg/m^3 of fine LWA, was applied. Noticeable increases in strength from 2% to 10% of Count Street Bridge and 15% of Bartell Road Bridge at 28 d were reported[45].

Self-curing method is effective for improving performance of HPC both in laboratory and actual practice. Extensive research demonstrated that self-curing property of concrete can keep autogenous shrinkage from occurring, thus contributes to lower the risk of cracking and prolong the service life of concrete. Nevertheless, following issues are still required to be solved before fully application of self-curing concrete. Firstly, numerous of contradictory results and interpretations exist in mechanical strength and durability. Secondly, the mechanism and efficiency of different curing agents in terms of type, dosage, particle size and spatial distribution are still ambiguous. Finally, more accurate models of the effect of self-curing agent on the concrete performance needed to be put forward.

5. Self-Sensing Concrete

Self-sensing concrete, also known as self-monitoring or self-reporting concrete, refers to the concrete with capacity of sensing its own state (*e.g.*, strain, stress, damage or temperature) without the need of embedded, attached or remote sensors[46]. A moderate amount of functional fillers, with a certain shape and dimension, are incorporated into concrete matrix, and then the insulated concrete becomes conductive. Influenced by the field of force and/or temperature, the conductive path of composite altered due to the variation of concrete microstructure, thus resulting in the changes of electrical properties such as resistance, capacitance, impedance, and voltage. Finally, variation of concrete microstructure is reflected in the electrical signals and can be measured by specified devices, *i.e.*, the concrete possesses self-sensing ability.

Self-sensing concrete is mainly composed of matrix and functional fillers in macro-structure level as shown in Figure 9. The matrix of self-sensing concrete is a generalized concept including concrete, mortar and binder only (Portland cement is the most used). The conductive fillers mainly consist of carbonaceous, metallic and polymer material, among which carbonaceous and metallic fillers are the most widely used and investigated. The properties of commonly used fillers are summarized in Table 3. It has been demonstrated that, some functional fillers can not only improve the conductive characteristic of concrete but can also enhance its mechanical properties and durability[47]. In addition, a more preferable property of self-sensing concrete can be obtained by synergistically use of two or several functional fillers and the positive hybrid effect is pronounced than any of them alone[48].

Excellent electrical property is necessary for self-sensing concrete. Therefore, a fully comprehension about the generation mechanism is the basis of controlling and improving the self-sensing properties of concrete. Unfortunately, the conductive mechanism is

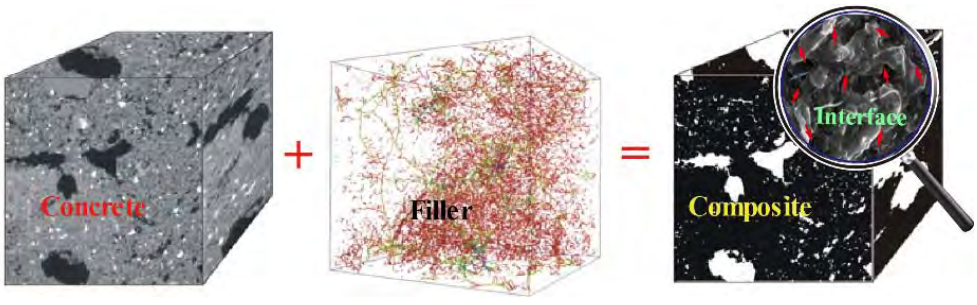

Figure 9. Structure of ISSC[49]

Table 3. Properties of functional fillers

Type	Elastic modulus /GPa	Tensile strength /GPa	Electrical resistivity /(mΩ×cm)	Elongation/%	Advantages	Disadvantages
PAN-based carbon fiber	35–450	2.0–4.5	0.01–1.0	0.4–1.8	High strength, conductivity and stability	Expensive, difficult to disperse
Pitch-based CF	160–800	0.6–3.0	$(1–4) \times 10^{-2}$	0.4–2.5	High strength, conductivity and cheap	Poor impact strength, easy oxidized
Nano-carbon black	–	–	200–1000	–	High conductivity, easily dispersed, cheap	Low strength, high water absorption and pollution
Carbon nanofiber	400–600	2.7–7.0	5.5×10^{-4}	50	High strength, conductivity and stability, cheap	Difficult to disperse
SWCNTs	1000	50–500	–	30–40	High chemical stability	Expensive, difficult to disperse
MWCNTs	300–1000	50–200	$(5–50) \times 10^{-3}$	5–20	High strength and conductivity	Difficult to disperse
Graphite powder	1 060(in-plane)	–	$(4–18) \times 10^{-3}$	–	High electric and thermal conductivity, stability	High dosage, low strength
Steel fiber	0.5–2.1	1.15	$(l.33–2.44) \times 10^{-2}$	1	High strength, durability and sensitivity	High SNR, easy agglomeration and oxidized
Steel slag	–	–	4–50	–	High strength and stability, cheap	Low-purity, low conductivity
Nickel powder	–	–	0.6–1.0	–	High strength, most sensitive, anti-corrosion	Expensive
Nano-TiO_2	–	–	3×10^{-3}	–	High sensitivity	Obvious polarization

SWCNTs: Single-walled carbon nanotubes; MWCNTs: Multi-walled carbon nanotubes; SNR: Signal to Noise Ratio

still debatable and existing interpretations are variable. One of the interpretations accepted by researchers considers the conducting modes in self-sensing concrete are as follows: the electronic and/or hole conduction (*i.e.*, contacting, tunneling and and/or field emission conductions) coming from conductive fillers[50-52]; and the ionic conduction coming from the concrete matrix[53]. While it is noticeable that the hole conduction is only exist in carbonaceous fillers[3,54]. Correspondingly, there are four paths for current transmission: the interior of cement stone, the interface between conductive fillers and cement matrix, the contacted or overlapped conductive fillers, and the conductive network formed by conductive fillers[46]. Concrete self-sensing property may be influenced by multiple factors such as external force, voltage, properties of fillers, water binder ratio, age, water content and service environment, *etc.*[54-58]. For dominating the formation and distribution of conductive networks, filler concentration is a primary parameter affecting the property of self-sensing concrete among those factors. The electrical resistivity of self-sensing concrete changing with filler concentration is depicted in Figure 10. There is a critical composition called percolation threshold[59], beyond which the electrical resistivity is reduced sharply, thus leads to the transformation of concrete from an insulating range to a semi-conductive or conductive range. According to this percolation threshold, the conductive characteristic curves divided into three zones (as shown in Figure 10).

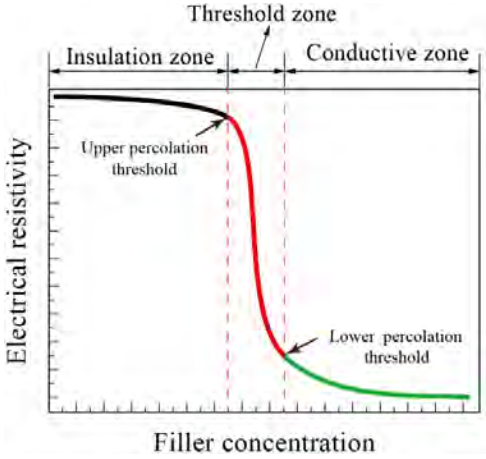

Figure 10. Change of the electrical resistivity along with filler concentration[59]

An insulation zone refers to the curve with highest resistivity, while the part with dramatically decreased resistivity is percolation zone and the last part with stabilized lowest resistivity is conductive zone. Although the conducting modes and paths mentioned above always exist simultaneously, only one or several of them dominate the status of a certain zone depending on the concentration of conductive fillers[60,61].

Up to now, much effort has been devoted into the research on self-sensing concrete. In 1989, a moderate amount of short-cutting carbon fiber was incorporated into the concrete by Chung and found some correlation between the electrical resistivity and interior structure of

the concrete. This marks the beginning of intelligence carbon fiber concrete[62]. Thereafter, the concept of "self-diagnosing" was first proposed by Muto in 1992[63], stated as a concrete possessing the ability of sensing its own damage. Later in 1993, Chung put forward the concept of "smart concrete" and conducted a systematic study on smart concrete for thirty years[64]. Then, the Seebeck effect of carbon fiber reinforced concrete (CFRC) was found by Li in 1998, *i.e.*, an electrical field gradient could be induced by the temperature gradient. CFRC expressed as a stable and repeatable linear relation between thermoelectric force (TEF) and temperature variation (Δt), as illustrated in Figure 11[51]. With different content of carbon fiber, the thermoelectric power can reach up to 18 $\mu V / ℃$ [51]. All of these make it possible for fabricating a temperature sensor by carbon fiber cement-based material[65-67]. Subsequent research found that, a Positive Temperature Coefficient (PTC) or a Negative Temperature Coefficient (NTC) could generate within the conductive concrete and they may alter the development tendency along with different conductive fillers[68,69]. Moreover, a series investigation on various self-sensing concrete towards the mechanical properties, mechanical-sensitive mechanism, temperature-sensitive mechanism, measurement methods and environment influence *etc*., were carried out by researchers, also some prospects about engineering application were given[70-77]. In addition, micron or nano sized functional fillers, especially for fibrous fillers, are inclined to entanglement and agglomerate, which turns their dispersion in concrete into a critical issue[78,79]. To solve this problem, physical dispersion methods (*i.e.*, high-speed shear or ultrasonic dispersion), chemical dispersion methods (*i.e.*, surfactant or dispersant) and the combination of them were widely studied in the past few years[80-81]. It should be pointed out that an appropriate dispersion method can not only increase the electrical properties of concrete, but also improve the strength and durability[47,82-84].

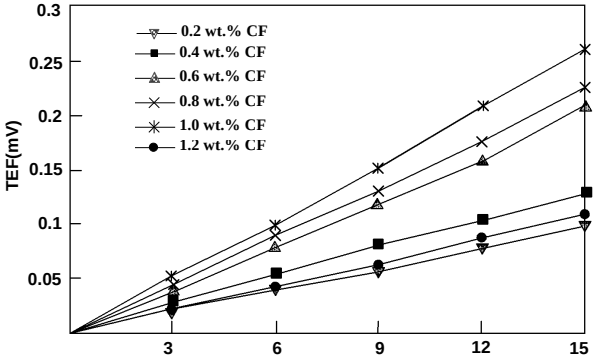

Figure 11. The relationship between temperature and TEF of CFRC[51]

Self-sensing concrete possesses high sensitivity (the strain sensitivity coefficient is several tens or even hundreds, while strain gage is only two[46]), integrating structure and sensing property to a whole system. Depending on the intelligent character, dynamical and timely detection of stress, deformation, temperature, crack and damage can be realized[46,61,66,85-90]. It therefore has a wide application potential in the field of structural health monitoring and traffic detection[49,84,91-93], as shown in Figure 12. This would be helpful for ensuring structural reliability, lowering the cost of construction and maintenance, *etc*.

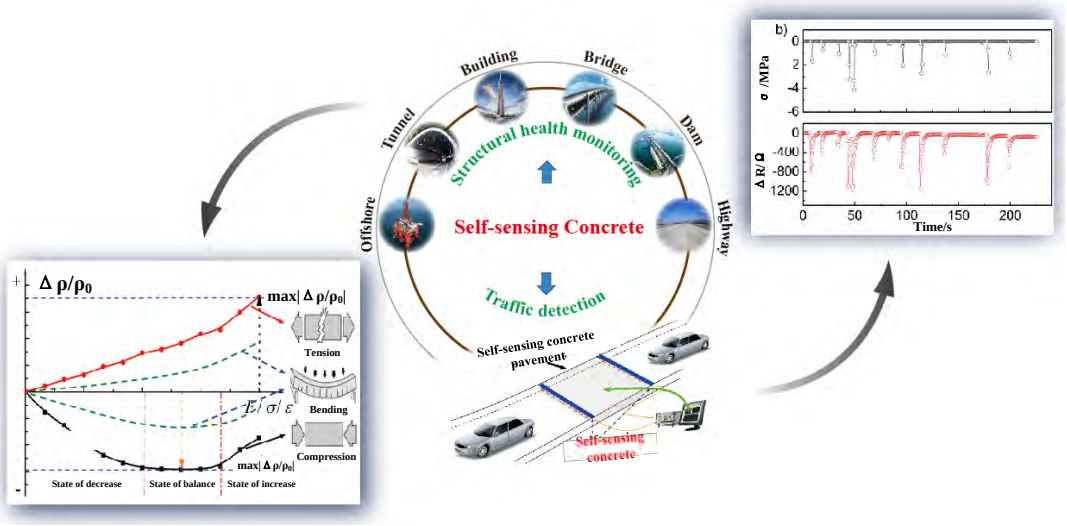

Figure 12. Applications of self-sensing concrete

Although self-sensing concrete has emerged more than three decades, many efforts are needed to promote its development. Under harsh external environment, the electrical properties of self-sensing concrete are unstable and the measurement accuracy is sharply reduced. The sensing behaviors of self-sensing concrete under complex stress condition should be further investigated. Besides, optimization of functional fillers, influence of aggregates and selection of dispersant methods are required to be deeply explored.

6. Self-Healing Concrete

Influenced by inherent characteristics of concrete and complex external environments, the appearance of cracks is inevitable during the molding and service of concrete. Certain paths will be damaged or exhibiting cracks caused by water and aggressive substances intruding into the concrete, thus increasing the risk of various degradations of the material. For reinforced concrete structures, wide cracks may result in the reinforcement exposed to the environment. Consequently, total deterioration of the whole system may occur once the reinforcement starts to corrode or spall[94]. Considering the damages of crack to the concrete durability, crack maintenance is needed for sustained usage. However, repair of crack is very difficult, especially when the cracks are invisible or inaccessible. Inspired by the nature of blood clotting or remolding of fractured bones in living things, the same concept is incorporated into the engineering materials by scientists, making them possess the ability of repairing or healing damage by themselves[95].

As a kind of self-healing material, self-healing concrete is also named self-repairing or self-sealing concrete and the essence is the concrete itself to provide necessary adhesive products which can fill in the cracks when damage happens. In general, self-healing concrete is classified into two categories: autogenous and autonomous healing concrete[96,97].

6.1 Autogenous healing Concrete

The autogenous self-healing concrete is defined as the concrete with ability of sealing itself without external monitoring or human intervention. Cracks within concrete may get repaired in a time because of the continuously hydration of clinker minerals or carbonation of calcium hydroxide [$Ca(OH)_2$]. Self-healing of cracks in the concrete is a combination of complicated chemical, physical and mechanical interactions[98]. Most researchers believe that autogenous self-healing of young concrete is mainly owing to continuously cement hydration, whereas at later ages, self-healing is most attributed to the formation of calcium carbonate ($CaCO_3$)[99,100]. For each autogenous self-healing mechanism of concrete, the presence of water is essential due to its important role in causing chemical reaction and transporting fine particles. If crack widths restricted or crack closure is acquired, autogenous healing could be more effective. It was demonstrated that crack width of maximum 50 μm show complete healing and up to 150 μm show partial recovery of mechanical and transport properties[101]. To improve the ability of autogenous healing of concrete, latent hydraulic and pozzolanic admixture (*i.e.*, fly ash, lime, blast furnace slag) or superabsorbent polymers (SAP) and expansive agent are usually incorporated into concrete[102-106]. Some researchers focused on the autogenous self-healing behaviors of the Ultra PC (UHPC) which is characterized by a low water to cement ratio (close to 0.2) and high content of admixtures. This implies that UHPC has a great amount of anhydrous clinker, and thereby a potential for self-healing by the sustained hydration of binder materials[107,108]. Three-point flexural test and numerical simulation were conducted on the UHPC specimens after initially cracked and cured in the water. The results of 1, 3, 10 and 20 weeks curing are presented in Figure 13 and show a good agreement between simulation and experiment. It can be seen that a fast recovery of global stiffness and a light improvement of resistance have been highlighted with the curing time[109]. On the other hand, arresting crack width by high performance fibers also attributes to the self-healing process. For example, Engineered Cementitious Composites (ECC) as the material involving PVA fiber realize the multiple cracking pattern and average crack width under 60μm[110,111]. Furthermore, concrete reinforced by chemically flax and hemp fibers can control the maximum crack width under 30um, which fully ensures a complete healing of concrete[112,113].

The autogenous self-healing capacity of concrete is an ancient phenomenon acting positively. It is acknowledged as one of the reasons explaining the survival of many old buildings and structures. However, the work of autogenous healing is limited to small cracks and relatively low recovered strength can be offered. Meanwhile, autogenous healing is effective only accompanied with water, which is difficult to control. Thus, too many uncertain factors are needed to be taken into account explicitly and make the design of autogenous self-healing concrete challenging. In this case, the autonomous self-healing concrete is proposed.

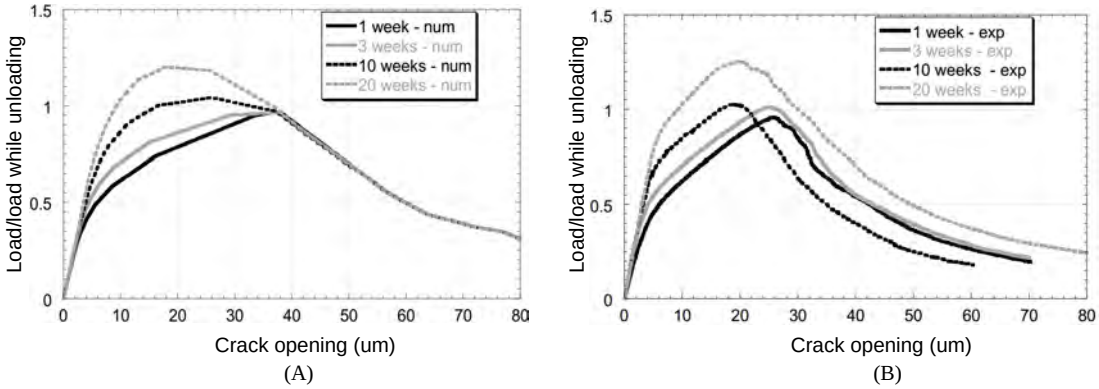

Figure 13. Numerical simulation (a) and experimental result (b) of bending test on healed UHPC concrete specimens[109]

6.2 Autonomous healing Concrete

The autonomous self-healing concrete, sharing the same concept with other artificial self-healing composites, is created by embedding self-healing units composed of container and healing agent in the host concrete. The container is usually hollow fibers and capsules with spherical or cylindrical shape, which both serves as the container of healing agent and acts as barrier to prevent reactions between healing agent and host material. Accordingly, an ideal healing agent is supposed to be able to continuously sense and respond to the damage, and recover the material performance without adverse effect. The autonomous healing process can be divided into two steps as illustrated in Figure 14. Firstly, the healing agent is released into the crack faces through capillary action or gravity once the container is ruptured by the propagating crack. Then, chemical reaction takes place between the healing agent and host material to bond the crack planes together and alter the shape of the crack tip. Finally, the crack propagation may be held back and material properties such as stiffness, fracture toughness and strength may be recovered.

The concept of autonomous healing in concrete was originally proposed by Dry in 1994[115]. The research on self-healing materials becomes flourishing after White published the paper about self-healing in polymer based materials in Nature[114] in 2001. Until now, a wide range of researches are being undertaken on autonomous self-healing concretes. The healing mode is broadly distinguished into three groups: internal hollow tubes, microencapsulation, micro-organisms[116-118]. The merit of hollow tubes healing is that the most used tubes are glass or other brittle material which can effectively release healing agent. For microencapsulation method, the system is simple and the capsules can deal with fractures at different locations because they are dispelrsed uniformly inside the matrix. The biggest advantage

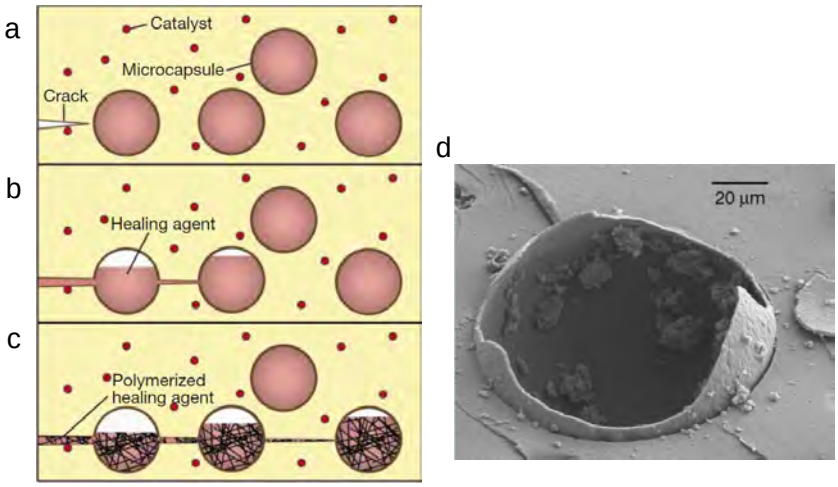

Figure 14. Basic method of the microcapsule approach. (a) Cracks form in the matrix; (b) The microcapsules ruptures, releasing the healing agent into the crack plane; (c) The healing agent contacts the catalyst, bonding the crack faces closed; d-ESEM image showing a ruptured microcapsule[114]

Table 4. Research methods and achievements of autonomous self-healing

Healing strategy	Agent carriers	Healing agent	Way of curing	Results	Reference
Internal encapsulation	Glass/ceramics tube	Cyanoacrylate	Air	Regain 50% strength and stiffness	Tittelboom *et al.*, 2010[119]
	Glass tubes	Epoxy resin	Air	32% higher strength than reference specimen	Thao *et al.*[120]
Microencapsulation	Silica gel shell	Methyl methacrylate	Heating	Recover over 80% fracture toughness	Yang, 2009[121]
	Polyurethane	Na_2SiO_3 solution	$Ca(OH)_2$ matrix	Recover 26% original strength	Pelletier *et al.*[122]
Bacteria	–	Bacillus sphaericus	Water and O_2	Heal crack up to 0.46 mm wide	Jonker *et al.*, 2010[123]
	Polyurethane	Bacterial solution	Contact component	regain 60% strength	Wang *et al.*, 2012[124]

of micro-organisms is that most bacteria are able to induce carbonate precipitation in the micro-crack region, thus repairs cracks with environmentally friendly processes.

Autonomous self-healing concrete is more reliable and not much dependent on the surrounding environment compared to autogenous self-healing concrete. Although autonomous self-healing appears as a great potential approach, it remains a great challenge to extend this idea from investigation to application. Hollow fibers, microencapsulation is difficult to cast in concrete, bacterial activity decreases a lot in the high pH (>12) environment as it presents in concrete. The effect of triggering mechanism of self-healing on the durability, compatibility and mechanical properties of concrete also demands a much deeper research in the future.

7. Self-Adjusting Concrete

Self-adjusting concrete has the ability to adjust its internal structures (*e.g.*, pore structures) and performance (*e.g.*, heat capacity, moisture content and hydration process) under external actions. It mainly includes anti- spalling self-adjusting concrete, moisture self-adjusting concrete, thermal parameter self-adjusting concrete and hydration heat self-adjusting concrete. Self-adjusting concrete not only has the ability to improve the comfort of habitation, but also has the ability to avoid temperature cracks which are due to the hydration heat of cement and concrete spalling caused by high temperature. The researches and applications of self-adjusting concrete have aroused a lot of concern in recent years.

7.1 Anti-Spalling Self-Adjusting Concrete

Concrete is prone to spalling when it encounters high temperature or fire. Anti-spalling self-adjusting concrete, which is consist of synthetic fibers (*e.g.*, polyethylene fibers, polypropylene fibers and polyacrylonitrile fibers) or metal fibers and concrete, can adjust their pore structure and thermal performance (*e.g.*, thermal conductivity and specific heat capacity) according to the outside temperature to prevent spalling. It was first proposed by Goldfein in 1965. The polypropylene fibers were added in the concrete as admixtures[125-127].

Currently, there are two main reasons widely accepted for the concrete spalling at high temperature[128-130]. The first reason is the internal vapor pressure principle. The water vapor is blocked as it escapes from the concrete pore at high temperature. It results in rising the vapor pressure and expansion stress in concrete. Then, the vapor pressure and expansion stress in the concrete increase with the rising ambient temperature. The second reason is the principle of thermal stress. It has been demonstrated that the temperature gradient is generated by a high ambient temperature. The temperature gradient can induce the thermal stress which will lead to concrete spalling eventually.

Synthetic fibers can be added into concrete to solve the concrete spalling caused by vapor pressure principle. The melting point of synthetic fibers ranges from 150 °C to 200 °C generally[131]. Due to the uniformity of the synthetic fibers dispersion and the small volume of fibers, the synthetic fibers would melt and form numerous channels inside the concrete when the temperature reaches the melting point of synthetic fibers. The channels inside the concrete provide opportunities for water evaporating, thus reducing the pressure of concrete and the possibility of concrete spalling[132]. Xiao[133] confirmed the presence of polypropylene fibers can effectively prevent the spalling of HPC through experiments. Kalifa *et al.*[128,134] study the spalling performance and microstructure of polypropylene fiber concrete. According to permeability measurement experiments on the concrete with different fiber content, the vapor pressure inside the concrete is obviously reduced by polypropylene fibers under the high temperature. The pressure versus-time curves have a similar shape with different fiber contents. However, the height of the peaks sharply decreases with increasing fiber content as show in Figure 15. The internal peak pressure is reduced by one-fourth and the pressure gradient decreased in half when the content of polypropylene fibers increases from 0 to 3 kg/m^3. In addition, the fiber dosage of 2 kg/m^3 with

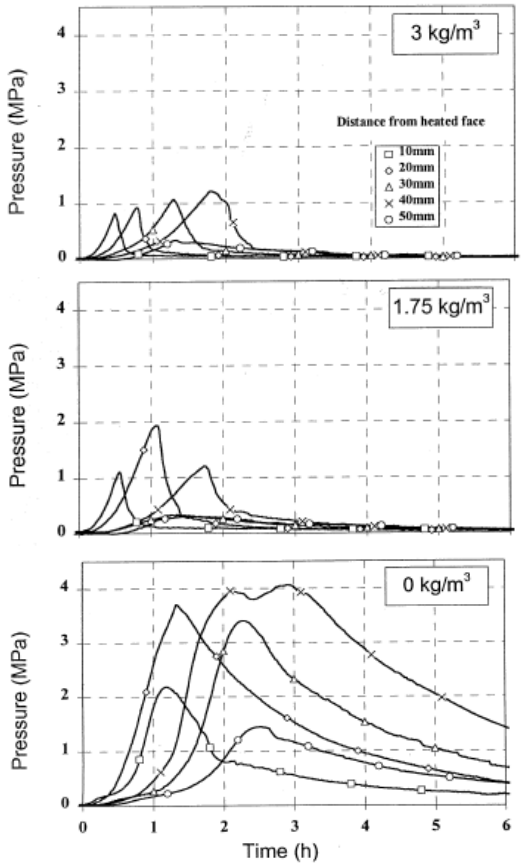

Figure 15. Pressure versus-time curves of concrete with different fiber contents[134]

the fiber length of 20 mm is the optimal for preventing spalling in grade C100 HPC.

Due to the low thermal conductivity of concrete, the temperature difference among the various parts of the concrete structure should be reduced in order to reduce thermal stress of concrete. Because the thermal conductivity of steel is approximately 40 times than that of conventional concrete, steel fibers are often added into the concrete to keep the consistency of temperature rise rate between inner part and the surface of the concrete, thus reducing the concrete spalling.

Although anti-spalling self-adjusting concrete can effectively reduce the possibility of concrete spalling, the durability and the compressive strength of concrete would be weaken because the addition of fibers increases the air content of concrete. Additionally, fibers will reduce the performance of fresh concrete, improving the difficulty of building operations, increasing the cost of tamping[135-137].

7.2 Moisture Self-Adjusting Concrete

Humidity environment not only relates to the durability of infrastructures and energy consumption, but also has greatly effect on healthy problems. In order to make a comfortable and healthy environment, it is important to control moisture level[138]. The moisture self-adjusting concrete is made of concrete with moisture adjusting materials (*e.g.*, zeolite, attapulgite or meerschaum), and can change the moisture content inside it with external humidity[139,140].

The moisture self-adjusting concrete containing zeolite powder was firstly proposed by Japanese scholars. It does not need the help from any artificial energy and equipment, relying on its own moisture absorption and desorption properties. The hydrated silicate calcium of zeolite contains pores in diameter of 1×10^{-10}–9×10^{-10} m. The water vapor adsorption capacity of concrete was improved with porous and multilayered honeycomb structure of zeolite powder, which has larger pore volume and surface area. The moisture self-adjusting concrete made of concrete with zeolite shows a big difference between various humidity conditions. The moisture self-adjusting concrete quickly reaches the moisture content equilibrium state in the low-humidity environment. In the contrast, the moisture content of the moisture self-adjusting concrete increases with time in a saturated humidity environment[141-144].

The working principle diagram of the moisture self-adjusting concrete is shown in Figure 16. When the air relative humidity exceeds a certain value Φ2, the moisture self-adjusting concrete will absorb moisture in the air to prevent from the increasing of the air relative humidity. When the air relative humidity is lower than a certain value Φ1, the moisture self-adjusting concrete will desorb moisture to prevent from the decreasing of the air relative humidity. If the moisture content of the concrete is between U1 and U2, the indoor relative humidity will be maintained within the range of Φ1–Φ2 automatically[145]. Goto *et al.* tested the moisture controlling performance of the moisture self-adjusting

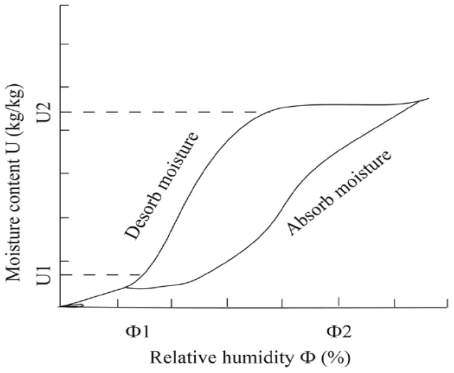

Figure 16. Equilibrium moisture absorption and desorption curves of the moisture self-adjusting concrete[145]

concrete with zeolite tuff. The amount of water vapor adsorption in the concrete containing fly ash can only reach half the amount of the moisture self-adjusting concrete. The water vapor adsorption isotherm of moisture self-adjusting concrete dried at 150 °C showed rapid adsorptive variation within range of 30–50 KH%[146]. Deng *et al*. studied the moisture self-adjusting capacity of the concrete with different concentrations of attapulgite (1% and 2%, respectively). The moisture desorption capacity of concrete increases with concentrations of attapulgite. The moisture desorption capacity of concrete with 2% of attapulgite is 1.8 times than that of concrete with 1% of attapulgite[147]. Li *et al*. made moisture self-adjusting concrete bricks in which the meerschaum-to-cement ratio is 0.144 by weight. The moisture self-adjusting concrete can adjust relative humidity in the test room from 90% to 65% in 4.5 hours[148].

Although the moisture self-adjusting concrete has the great ability to maintain indoor relative moisture in a range of 40%–70%[4], its disadvantages are low mechanical properties and poor durability.

7.3 Thermal Parameter Self-Adjusting Concrete

Thermal parameter self-adjusting concrete is a kind of smart concrete which utilizes the phase change materials (PCMs) to achieve the function of thermal parameter self-adjustment. PCMs have the ability to absorb or release heat when the material changes from solid to liquid and vice versa. Thermal parameter self-adjusting concrete can maintain the temperature near the required temperature for a period of time by reducing the frequency of temperature fluctuation[149-152]. Thermal parameter self-adjusting concrete has great advantages in the field of building energy efficiency compared with the conventional concrete. It can stabilize the indoor temperature through its large specific heat capacity to guarantee the thermal comfort with low-energy when it is used to make exterior walls.

Lane[153] manufactured the thermal parameter self-adjusting concrete by using the method of direct immersion with mirabilite in the 1980s. However, this kind of PCMs has corrosive effect on concrete matrix. Since then, new types of thermal parameter self-adjusting concrete have been developed. Hirayama *et al*.[154] indicated that the specific heat capacity and the thermal mass of the concrete are increased by adding PCMs, and a building fabricated with thermal parameter self-adjusting concrete can reduce the size of air conditioning systems by adjusting the fluctuations of indoor temperature. Hunger *et al*.[155] investigated the specific heat capacity of concrete with different concentrations of PCMs (from 0 to 5wt. %). Thermal conductivity measurements illustrated that the addition of PCMs into the concrete leads to a reduction of thermal conductivity. With the PCMs-to-cement ratios increasing, the concrete specific heat capacity raises up to 3.5 times as the PCM content is 5%. Farid *et al*.[156] performed tests of two concrete slabs made of thermal parameter self-adjusting concrete and conventional concrete under 8 h heating and 16 h discharging heat cycles, respectively. The surface temperature of the conventional concrete slab ranged from 22.5 °C to 36.5 °C, while that of thermal parameter self-adjusting concrete slab ranged from 25.0 °C to 31.5 °C. Castellón *et al*.[157] tested the performances of two small house-sized cubicles. The first cubicle is made of thermal parameter self-adjusting concrete. The other one is made of conventional concrete. The two cubicles with the same characteristics are located next to each other. The cubicle with conventional concrete always keeps a bigger temperature value (2 °C–3 °C) than the cubicle with thermal parameter self-adjusting concrete. While the maximum temperature in the cubicle with conventional concrete is 39 °C, the maximum temperature in cubicle with thermal parameter self-adjusting concrete is only 36 °C. Furthermore, the first cubicle reached the same temperature 2 hours later than the second cubicle as shown in Figure 17.

Although the thermal parameter self-adjusting concrete has better latent heat storage performance, it also has some disadvantages due to PCMs. For example, the PCMs added in concrete prone to leakage when the PCMs become liquid phase. Some kinds of PCMs have a corroding effect on concrete. In addition, the stress produced during the process of phase change of the PCMs can result in damage in the concrete, thus affecting the durability of concrete.

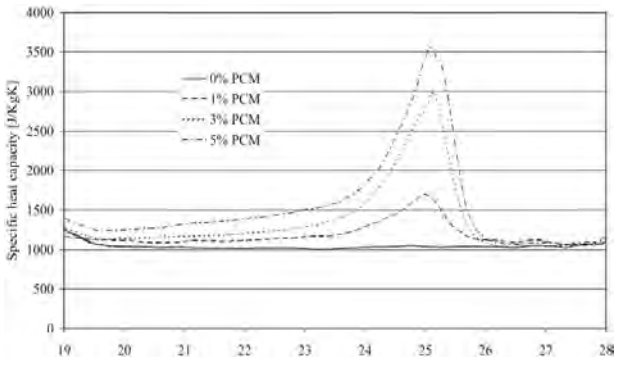

Figure 17. Specific heat capacity of the thermal parameter self-adjusting concrete with different PCM mixes versus temperature[155]

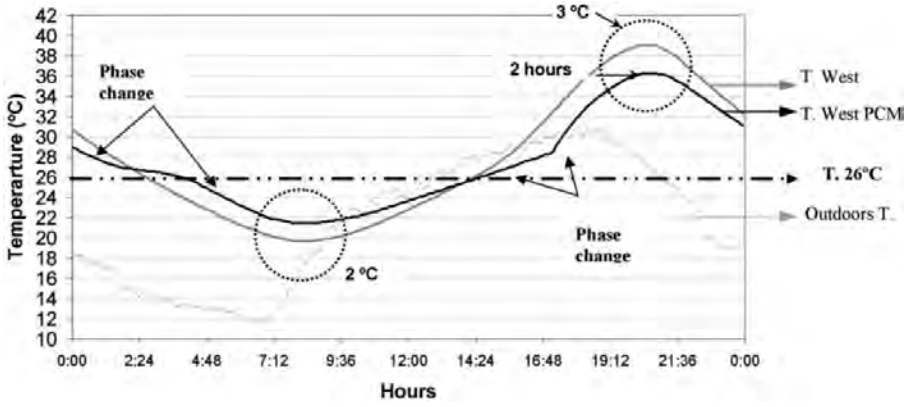

Figure 18. The temperature of the west wall of the two cubicles and the outside temperature[157]

7.4 Hydration Heat Self-Adjusting Concrete

Concrete is prone to emerge brittle failure after cracks due to its low tensile strength. There are many reasons for concrete cracking, but the main reason is the hydration heat of concrete. Hydration heat self-adjusting concrete is made of concrete and functional fillers. The functional fillers mainly consist of mineral admixture, retarders, starch-based polymers, PCMs, *etc*. It can effectively slow down the heat of hydration, thus controlling the temperature cracks in concrete[158,159].

Concretes with low strength and low heat of hydration are mainly used in small-scale projects before 1940s. Since 1940s, the concrete with high strength is used in mass concrete constructions more and more widely. The cracking problem of concrete has been received much attention[160]. On the one hand, cracks can cause the leakage problem of concrete, increasing the maintenance costs of the project. On the other hand, cracks make it easier for corrosive medium entering into the concrete interior, thus affecting the durability of concrete[161]. The study revealed that about 80 percent of the crack in mass concrete constructions is caused by concrete hydration heat. The heat generated by C_3S and C_3A hydration leads to the temperature rise of concrete as shown in Figure 19[162]. Because the dissipation rate of concrete internal hydration heat is slower than the dissipation rate of external heat, the temperature gradients between center and surface of concrete can generate temperature stress. When the temperature stress exceeds the ultimate tensile strength of concrete, the concrete surface will crack according to the principle of expansion and contraction[163].

Adding proper amount of fly ash into concrete decreases the content of C_3S and C_3A in concrete, and the release quantity of hydration heat generated by fly ash is

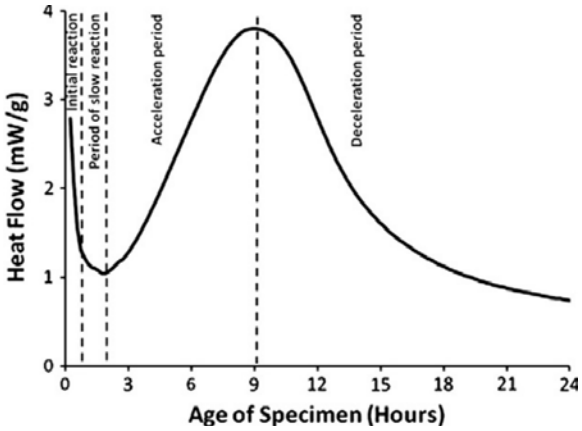

Figure 19. The concrete hydration heat flow curve[162]

far less than that by C_3S and C_3A, thus reducing the release rate and quantity of concrete hydration heat. Yang *et al*.[164] observed that the hydration heat self-adjusting concrete with fly ash can not only slow down the release rate of hydration heat, but also postpone the hydration exothermic peak occurs.

Because the retarders are prone to be adsorbed on the surface of cement particles, adding retarders can improve the stability of the cement particles and restrain the agglomeration of the cement particles. Hydration heat self-adjusting concrete with retarders can effectively delay the hydration of concrete and reduce the temperature cracks in concrete. Many researches showed that the more dosage of the retarders, the stronger ability to slow down the cement hydration heat[165,166].

Hydration heat self-adjusting concrete made of concrete and starch-based polymers is different from the hydration heat self-adjusting concrete with retarders. It could decrease the hydration heat evolution rate without changing the total heat generated. The hydration rate will be affected due to the slow release and adsorption of starch-based polymers on cement particles. The mech-

anism of starch-based polymers on cement particles is shown in Figure 20. Plank *et al*. applied hydration heat self-adjusting concrete in Nanjing International airport project (China). The temperature rise of side wall was controlled within 21 °C as shown in Figure 21[167].

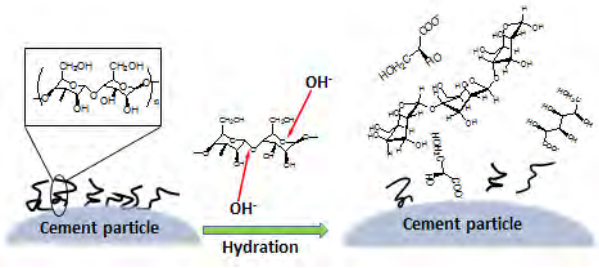

Figure 20. The mechanism action of starch-based polymers on cement particles[167]

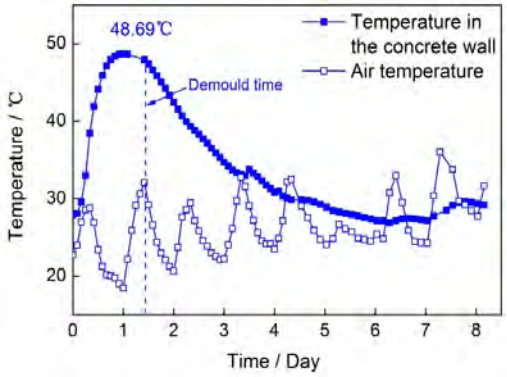

Figure 21. Curve of the temperature in hydration heat self-adjusting concrete wall and air temperature[167]

The hydration heat self-adjusting concrete with PCMs also has the ability to reduce the hydration heat of concrete. When the hydration heat of concrete reaches the melting temperature of the PCMs, the PCMs generate phase transition, thus reducing temperature crack caused by hydration heat of concrete. Xing *et al*.[168] found the hydration heat self-adjusting concrete can effectively adjust the hydration heat of concrete and reduce the peak temperature by 15 °C to 25 °C.

Although the hydration heat self-adjusting concrete could control the temperature cracks at some degree, the additives could weaken the mechanical property of the concrete[169].

8. Self-Damping Concrete

The damping function of the concrete is the capacity of changing vibration energy into other forms of energy. It is very important for reducing vibration in bridges, industrial and civilian infrastructure. Concrete is one of the main materials used in infrastructures, but the low damping property of concrete restricts its use in the structural engineering, especially for the further use in the structures which are under the frequent vibration loads. Therefore, the self-damping concrete is developed in the process of seeking solutions. The self-damping concrete improves its damping property through the introduction of functional fillers such as polymer latex, MWCNTs fibers, silica fume (SF), methylcellulose (MC) and graphite power[170,171].

The damping property of the self-damping concrete which contains polymer latex is due to the dispersing of polymer particles in the concrete. At the same time, it forms three dimensional continuous space network structures which can not only reduce the stress concentration of the concrete effectively, but also increase the capacity of deformation and energy dissipation. Thereby, it can slow down the spread of micro-cracks in the concrete. Wong *et al*.[172] studied the effect of the concentration and type of the polymers on the damping function of the concrete. It has been demonstrated that the damping function of the concrete has improved to varying degrees when the polymer cement ratio is in the context of 0%–25%. The concrete shows better damping function when the polymer cement ratio is in the context of 10%–20%. Fu *et al*.[173] measured the storage modulus, tan δ and loss modulus of the concrete with some admixtures under different temperatures and frequencies. They found the three quantities can be increased by adding latex, methylcellulose or silica fume to concrete. Taking into account energy applications, latex is proposed for use at >1.5 Hz, methylcellulose and silica fume is proposed for use at <1.5 Hz.

The damping property of the self-damping concrete which contains fibers, SF, and graphite power mainly comes from the interface friction and interfacial peeling caused by relative displacement. In addition, the development and extend of the micro-cracks between the matrix and fiber under the effect of tensile stress will produce energy consumption[174]. Luo *et al*.[175] studied the damping ratio of concrete with different concentrations of MWCNTs (weight fraction of MWCNTs, 0, 0.1%, 0.2%, 0.5%, 2.0%) and found MWCNTs in different sizes gather together, thus leading to more multi-phase interfaces and boundaries. The damping ratio of concrete with 0.5% weight fraction of MWCNTs is increased by 24.51% with respect to that of plain concrete (as exhibited in Figure 22). With the increasing of weight fraction of MWCNTs, the damping ratio of concrete has a rising trend. There are more interfaces between concrete and MWCNTs at higher weight

fraction of MWCNTs, which result in greater damping properties of concrete (as shown in Figure 22). Koratkar *et al.*[176] observed that the addition of carbon nanotubes can improve the damping ratio of concrete by 200% compared to the plain concrete. Wang *et al.*[177] reported that the vibration damping ability of concrete can be increased by adding silica fume into concrete. Concrete will reduce the damping ability by adding coarse aggregate or fine aggregate. Therefore, the aggregate proportion designed for reaching high compressive strength may not be able to achieve the effect of vibration damping. Further addition of silica fume can overcome the decreased vibration damping ability of concrete which is due to the adding sand to concrete. The loss tangent of the concrete with silica fume at 0.5 Hz is 0.14, and it is two orders of magnitude higher than that of plain concrete. Xu *et al.*[178] provided a method of increasing the damping ratio of concrete by adding piezo-damping composites. They observed that the damping property of concrete with graphite is obviously better than that of the concrete with epoxy resin. The largest damping loss factor of the concrete is 0.51 at a glass transition temperature of 70 °C when the graphite percentage is 1 wt. % as shown in Figure 23.

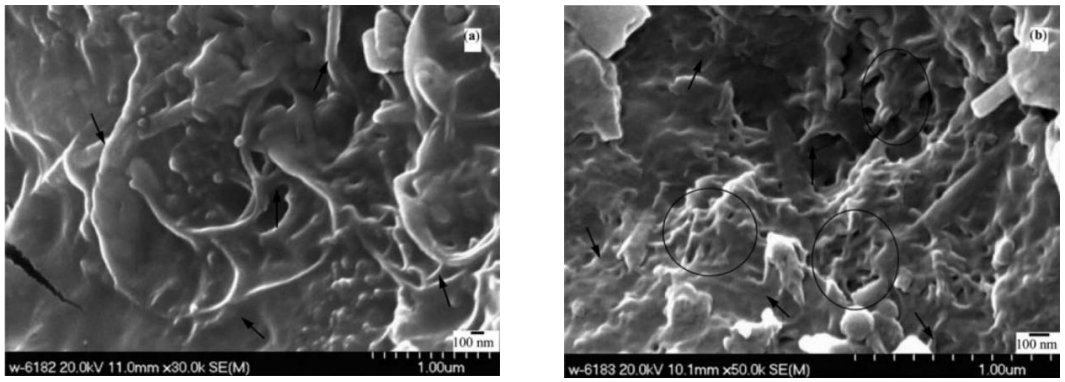

(A) Concrete with 0.5% weight fraction of MWCNTs (B) Concrete with 2.0% weight fraction of MWCNTs

Figure 22. Microstructures of self-damping concrete[175]

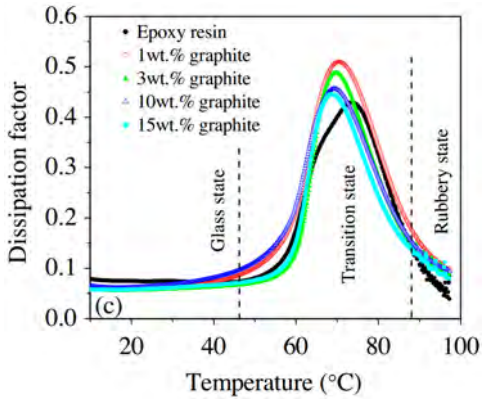

Figure 23. Dissipation factor of self-damping concrete at elevated temperature[178]

Although the self-damping concrete has better damping property than traditional concrete, some filler may decrease the compressive strength of concrete to some extent. In addition, it is lack of systematic research for durability which contains the volume stability, impermeability and frost resistance, *etc*.

9. Self-Heating Concrete

Self-heating property of concrete also relies on the electrical conductivity of concrete, similar to self-sensing concrete. The objective of self-sensing concrete is to detect the variation of concrete through the measurement of electrical signals, while self-heating concrete is to generate heat by applying voltage to concrete based on the Joule law [Equation (1)]. Actually, there is a cross-coupling relationship among the properties of various conductive concretes, as shown in Figure 24 and therefore makes it possible for conductive

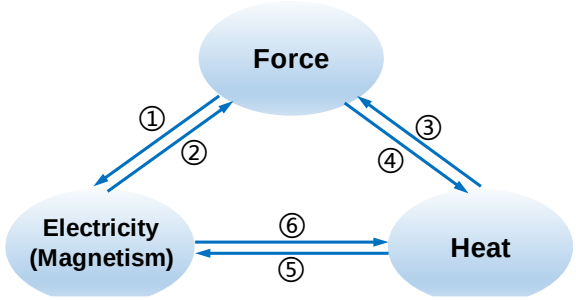

① Mechano-electric effect, ② Electric-mechano effect, ③ Thermo-dynamic effect,
④ Mechano-thermo effect, ⑤ Joule effect, ⑥ Seebeck effect.

Figure 24. Properties and their cross-coupling relationship of various intelligent concrete materials

concretes to possess multiple intelligent characters. In general, conventional concrete is hard to be heated due to its high resistivity. Then, electrically conductive fillers such as carbon fibers, steel fibers, steel shaving, nickel powders and graphite were incorporated to reduce the resistivity of concrete[179-187]. Therefore, the fabrication process of self-heating concrete is basically the same with that of self-sensing concrete.

Characterized by a heating element, conductive concrete is seen as an electric heater, thus self-heating concrete is also called electrothermal concrete. According to the formula of Joule law, resistivity is a dominant criterion which governs the effectiveness of a material for self-heating, particularly in relation to the power and the maximum temperature. There is a rational resistivity value for the concrete[182], *i.e.*, either excessive high or low is undesired for the materials used as heating element. Since an electric element with rather high resistivity would result in an extremely low current in the heating element (unless the voltage is very high). On the contrary, an electric element with excessive low resistivity would require an extremely high current to reach a certain power[186,188]. In addition, the stability of resistivity is a basic requirement for conductive concrete to become self-heating. Only with a stable resistivity, the steady electrothermal power will be attainable. Studies indicated that the resistivity of conductive concrete tended to be stable, on condition that the content of conductive filler closes to or more than the percolation threshold[189-192].

$$Q = I^2Rt \text{ or } P = I^2R \quad (1)$$

Where Q is calorific value, I is current, R is resistance, t is time, P is thermal power.

One of the applications of self-heating concrete is domestic heating. It is realized by substituting self-heating concrete for traditional concrete in the wall or floor and applying voltage to them, and then heat will be emitted continuously from the wall or floor. What's more, this kind of conductive concrete is absolutely safe to human since just a small voltage and current is needed when the concrete works and no electric can be felt even if touch it. A kind of carbon black concrete slabs (CBCS) was used as self-heating flooring material by Sun *et al*.[193]. The investigation manifested that the CBCS was able to raise the temperature of a small room up to 10 °C in 330 min and the distribution of temperature along the height of room was uniform. In addition, the heating system provided by CBCS floor was stable, sustainable and controllable. In former Soviet Union, electric heating floor and furring brick were made by self-heating concrete and they were used for providing heat for residence, factory and greenhouse. Another application of self-sensing concrete is road deicing or snow-melting. In freezing climates, many transportation infrastructures (such as driveways, bridges and airport runways) are prone to ice accumulation. Ice or snow accumulation on these infrastructures may cause a number of dangerous situations for traffic[194]. Therefore, improving the conditions of transportation infrastructures in a timely and high-efficient fashion is imperative. A conclusion of deicing and snow-melting methods used in the past thirty years was made by Yehia and Tuan[181,195]. They pointed out that the traditional snow removal and deicing methods (labor or machine removal and using salt *etc*.) are labor intensive and time-consuming, also will cause damages to both the constructions and the ecological environment. Compared with conventional deicing methods, self-heating concrete has the advantages of high efficiency, no negative effects and without pollution. The idea of employing steel fiber and shaving as conductive fillers was presented by Tuan and a serious of experiments involving deicing on the bridge deck was conducted[183]. After that, self-heating concrete was applied to the Roca Spur highway in American and steel shaving was replaced by graphite (with content of 25%). So far, this self-heating concrete system operates well and no conductivity reduction occurs. Preliminary cost analysis showed that the proposed conductive concrete bridge deck was less expensive than conventional concrete deicing methods[185]. Zhang *et al*.[186] employed nickel particle as conductive fillers and heating elements in concrete. Experimental results indicated that the concrete with nickel particles (12.0 vol. % and 2.6–3.3 μm in diameter) can melt 2 cm thickness of snow in 368 s at an input voltage of 15 V. Several pictures during the snow melting experiment were given in Figure 25. Self-heating concrete was also applied to subway in London to protect passengers from slipping on frozen platform. The self-heating concretes used in platform were characterized by rapidly warmed under low voltage.

However, it should be noted that the self-heating concrete requires high property of heating element including higher thermal rate, high mechanical properties, and stable electrical conductivity. Heating efficiency may be influenced by the factors of ambient temperature, wind speed and thickness of the ice/snow layer. Steel fiber is recommended in concrete which can better meet the requirement in engineering application.

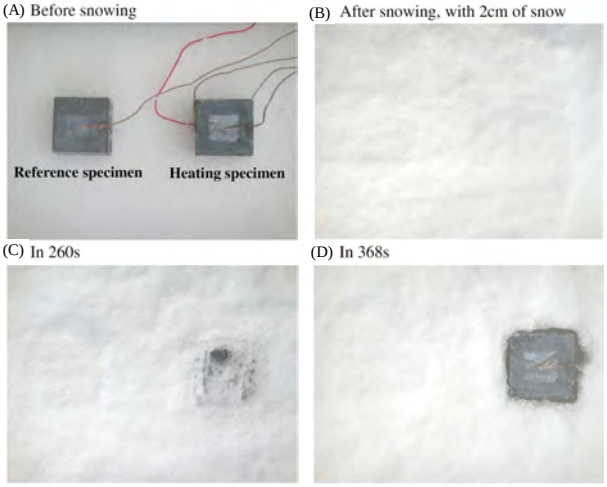

Figure 25. Snow-melting process of the self-heating concrete with nickel powders[186]

Nevertheless, the workability of concrete is inclined to become poor with higher content of steel fiber, also steel fiber is easily to corrosion. Therefore, new type self-heating concrete accompanying higher heating performance and long-term stability is still necessary to develop.

10. Self-Sacrificing Concrete

Self-sacrificing concrete, also called self-sacrificing anodic concrete, refers to the concrete with capacity of sacrificing itself to protect the cathode of impressed current cathodic protection (ICCP) system. Self-sacrificing concrete are made of conductive concrete, such as carbon fiber conductive concrete and steel fiber conductive concrete.

The damage caused by corrosion of the steel reinforcement is a prime factor of concrete corrosion. Cathodic protection (CP) system, in which sacrificial anodes cathodic protection and ICCP is used as two main cathodic protection components to control corrosion, is considered as a leading method for the protection against corrosion in concrete structures. As illustrated in Figure 26[196], in the ICCP systems, a

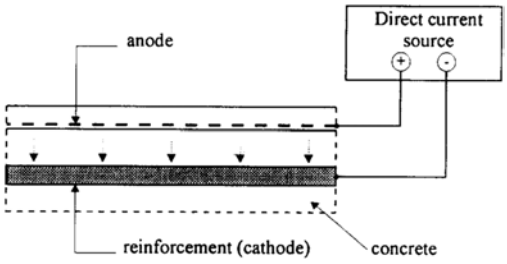

Figure 26. Schematic illustration of cathodic protection reinforcement of a concrete structure[196]

direct current flows through the concrete from a self-sacrificing concrete anode usually laid on the concrete surface to a cathode (*i.e.*, steel reinforcement). The anode connects with the positive terminal of a low voltage direct source, and the cathode connects with the negative terminal. In order to make charge balanced; the anode would lose electrons and be destroyed after about 30 days.

At the beginning of 1970, Stratfull[197] firstly used self-sacrificing concrete as anode in ICCP system, which is applied on a 307 m^2 bridge deck. Cañón *et al.*[198] used the self-sacrificing concrete and Ti-RuO_2 as anodes to build an ICCP system, respectively. Figure 27 shows the method of fabricating self-sacrificing concrete anode. They compared self-sacrificing anode with traditional Ti-RuO_2 anode and measured the chloride concentration profile of different depths, the initial chloride concentration profile, the final chloride concentration profile and the local efficiencies (in decreasing the Cl^- content) as showed in Figure 28(a), while the case of using Ti-RuO_2 as an anode as showed in Figure 28(b). It can be seen from these two figures that the efficiency of a sprayed anode based on self-sacrificing concrete is nearly the same as traditional reference anode (*i.e.*, Ti-RuO_2 mesh).

Figure 27. Device assembly with self-sacrificing concrete anode: (1) Self-sacrificing concrete is sprayed by using a compressed air gun on the surface of the specimen. (2) An absorbent layer of polypropylene is placed recovering the specimen surface. (3) The electrical circuit is installed. The positive pole of the source is connected to the anode, and the negative pole is connected to one of the longitudinal of the specimen reinforcement[198]

Yehia *et al*. used self-sacrificing concrete overlay as an anode to be cast on the top of a bridge deck for preventing reinforcement corrosion. Four slabs with different electrode sizes and spacings were tested. The supplied 2 V voltage provided ample CP in terms of meeting the required 4 hour 100 mV polarization in each slab at each test. Test results are shown in Table 5. It can be seen from Table 5 that there was a significant

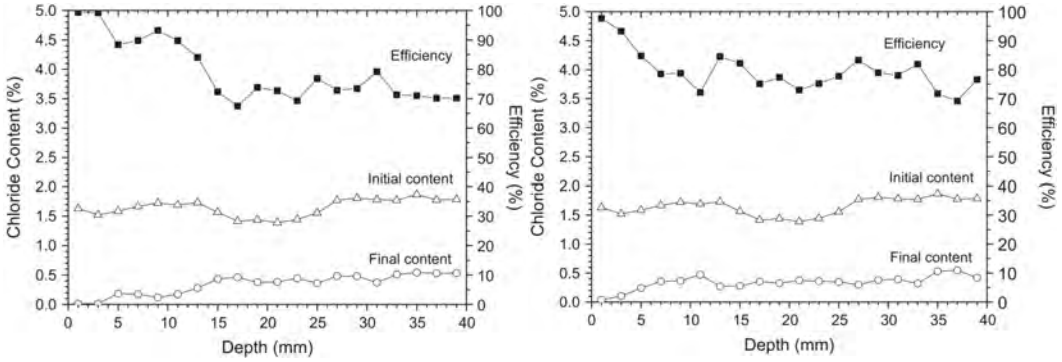

(A) Using self-sacrificing concrete as anode (B) Using Ti-RuO_2 as anode

Figure 28. The chloride concentration profile of different depths and the local efficiencies in decreasing the Cl^- content[198]

Table 5. Electrical resistance, current and polarization of four different self-sacrificing concrete overlay slabs

Specimen	Electrical Resistance/Ω	Current /mA	Area between electrodes/m^2	Current density/mA/m^2	'Instant-off' Voltage/mV	Four-hour Voltage/mV	Polarization /mV	Met NACE Polarization criteria
914 × 914 mm^2 slab	100.00	20.50	0.84	44.13	–900.0	–126.2	773.8	Yes
	100.00	19.96	0.84	42.95	–850.0	–131.6	718.4	Yes
	120.70	16.56	0.84	35.6	–860.0	–139.6	720.4	Yes
	149.60	13.53	0.84	29.17	–970.0	–152.9	817.1	Yes
	175.00	11.41	0.84	24.5	–1077.0	–159.6	917.4	Yes
1067 × 1067 mm^2 slab	105.70	18.89	1.14	27.13	–840.0	–106.5	733.5	Yes
	100.00	20.18	1.14	28.95	–860.0	–101.9	758.1	Yes
	147.90	13.53	1.14	19.37	–850.0	–139.9	710.1	Yes
	185.50	10.86	1.14	15.61	–970.0	–150.9	819.1	Yes
	223.70	8.93	1.14	12.81	–850.0	–166.4	683.6	Yes
1219 × 1219 mm^2 slab	84.56	23.65	1.49	24.22	–830.0	–101.7	728.3	Yes
	104.20	19.33	1.49	19.8	–830.0	–145.6	684.4	Yes
	143.80	12	1.49	19.8	–830.0	–145.6	684.4	Yes
	185.50	8.53	1.49	8.72	–1052.0	–156.0	896.0	Yes
1524 × 1524 mm^2 slab	127.40	15.79	2.3	9.47	–810.0	–197.4	612.6	Yes
	149.14	13.39	2..3	7.97	–1015.0	–229.1	785.9	Yes

polarization during 4 hour period. The 100 mV polarization criterion was met and hydrogen discharge was limited. In this ICCP system, the anode is destroyed after about 30 days, while through the removal of the destroyed concrete overlay, a new self-sacrificing concrete coating could be paved. As a result, the anode could continue to protect the bridge decks[199].

Self-sacrificing concrete has a promising application prospect due to the following advantages: (1) its construction is relatively easy. It can be sprayed with a compressed air gun and used as coating to treat sizable vertical surfaces such as structural supports, especially structural concrete elements with complex shapes; (2) it not only has the structural function, but also has the replaceable function; (3) it is low-cost compared with other types of anode. However, there exist some issues needed to be addressed, such as long-term poor stability and durability of anode materials and rectifiers, limitation to monitor and to maintain the system, insufficient understanding of fundamental technology with regards to the self-sacrificing concrete, and degradation of the mechanical properties during service life of the self-sacrificing concrete.

11. Self-Cleaning Concrete

Self-cleaning concrete is the concrete with abilities of resisting wetting by liquids or cleaning hazardous substance in the surface of concrete by itself. To obtain self-cleaning concrete, two strategies are usually applied: superhydrophobic and photocatalytic.

Solid materials are divided as hydrophilic and hydrophobic according to the water contact angel (WCA). Contact angel is described as the angel between solid surface and the tangent line of liquid phase in the surface of solid phases. For a contact angel more than 90°, hydrophobic behavior is deemed to appear and a contact angel less than 30° could denote the hydrophilic phenomenon. Superhydrophobic and superhydrophibic surfaces are the subclasses of hydrophobic and hydrophibic surfaces, respectively. The contact angels formed by water droplets upon superhydrophobic surface are usually over than 150°, and those upon superhydrophibic surfaces are less than 10°, as shown in Figure 29. Normal concrete is a porous material which can absorb water and therefore considered as hydrophilic material.

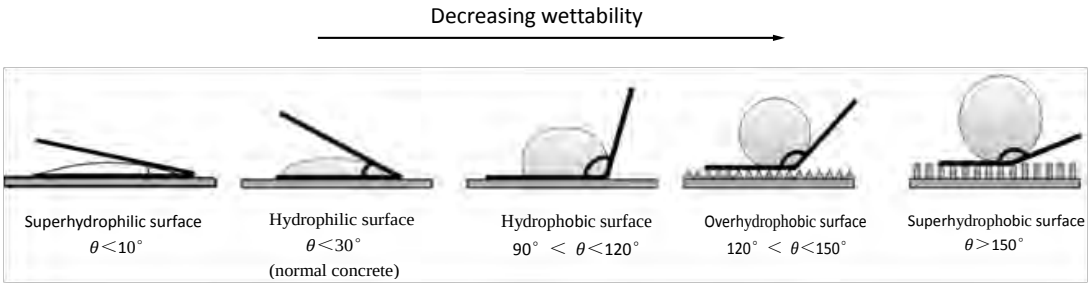

Figure 29. Superhydrophilic, hydrophibic, hydrophobic, overhydrophobic, superhydrophobic surface.

11.1 Superhydrophobic Concrete

Superhydrophobic self-cleaning concrete is a novel of biomimetic inventions[200], whose inspiration comes from the Lotus Effect[95,201]. It is well known that leaves of lotus plant can remain clean and free of contaminants, although the habitats are mainly muddy rivers and lakes. This phenomenon is attributed to the superhydrophobic nature of lotus leaves, as illustrated in Figure 30. The direct contacts between water and lumps that existed on the lotus leaf can drive the water split into plenty of small spherical droplets. Then the bead could roll and tumble off the leaf even with the slightest angles. Simultaneously dirt particles and small insects are pack up as bead goes. Thus self-cleaning is realized and this process is named the Lotus Effect[95].

The superhydrophobicity of materials is determined by the geometry and chemical constitution of material surface[202]. Usually, a specified micro and nano-structure morphology formed by the combination of high surface roughness and low surface energy is employed to achieve the superhydrophobicity[203]. It is found that the superhydrophobic self-cleaning ability of concrete can be achieved by incorporating some admixtures into concrete[204,205]. The admixtures have been reported to increase the concrete hydrophobicity including nanoparticles, oil, wax and water resistant polymers *etc.*[206,207]. Batrakov concluded that hydrogen can be released by the reacting of hydroxyl groups of CH and siloxane-based admixtures such as polymethylhydrosiloxane (PMHS) due to the Si-H bond of admixtures. As a consequence, small (10–100 μm) and well dispersed air voids are created throughout the concrete[208]. The walls of these voids are then coated by submicron or nano-sized particles and a hierarchical surface roughness is produced to achieve superhydrophobic properties within the hardened cement phase/paste (Figure 31)[209]. To obtain an optimum performance, more than 70% of the PMHS should be dispersed to the level of under 1 μm[200]. As a result, the surfaces of the voids are covered by the hydrophobic particles, providing the effect of superhydrophobic hybridization. The idea of mixing superhydrophobic admixture with ECC to form an ultra-durable material-superhydrophobic ECC (SECC) was proposed by Sobolev[209,210]. The investigation demonstrated that the incorporation of superhydrophobic admixtures in ECC was beneficial for improving flexural toughness without adverse influence on the compressive strength. This reinforcement effect was achieved by the addition of admix

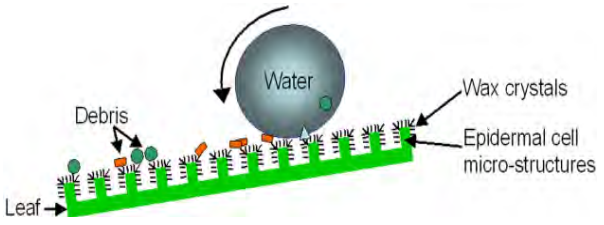

Figure 30. Water forms droplets on the tips of the epidermal protrusions and collects pollutants, dirt and small insects as it rolls off the leaf[95]

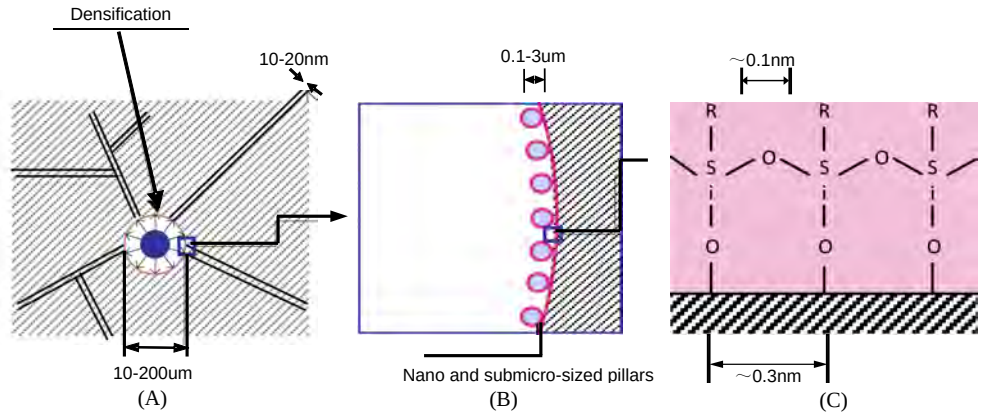

Figure 31. How the superhydrophobic hybridization of concrete works. (a) PHMS admixture, (b) Engineered superhydrophobic pore surface, (c) self-assembly of hydrophobic 2D network on the pore/pillar surface[209]

tures including 25% PMHS along with 4.4% polyvinyl alcohol surfactant and small quantities of submicron sized particles. And this composition of admixtures was proved to be the most ideal admixture since small and well dispersed air voids were created within the concrete.

The superhydrophobic self-cleaning concrete can not only clean the surface of concrete but also decrease the water absorption and permeability. Thereby durability of concrete can be optimized by the characteristic of superhydrophobicity which makes concrete valuable in the long run of construction for reducing the restore costs. Furthermore, superhydrophobic property of concrete can also play roles in reducing the accumulated snow or ice on the road in cold regions[211]. However, most of superhydrophobic admixtures mixed into concrete may lower the strength of concrete.

11.2 Photocatalytic Concrete

Photocatalysts material is related to the materials which can catalyze chemical reaction with the involvement of light illumination[212]. Photocatalytic property of self-cleaning concrete is mainly achieved through introducing photocatalysts into it. Currently, TiO_2 is the most widely investigated and used photocatalysts for the advantages of highly stable property in the dark, strong oxidizing ability under ultraviolet (UV) lighting, low cost and innoxious. The crystallographic TiO_2 exists in three forms: brookite, rutile and anatase. Compared with other two forms, the anatase crystal is proved to be the most photocatalytically active due to the spherical particles and large specific surface area[213].

One of the photocatalytic mechanisms is photo-induced redox reactions[214]. As a semiconductor material, the electronic structure of TiO_2 is characterized by a filled conduction band (CB) and an empty valence band (VB), which are distinguished by a band gap of energy (ΔE). Without enough photonic excitation $(i.e., h_v < \Delta E)$, the photocatalyst is at the ground state and the electrons are confined in the range of VB, as shown in Figure 32(a). However, once a photon containing the energy equal to or larger than $\Delta E (i.e., h_v \geqslant \Delta E)$ is absorbed by TiO_2, the electrons will overcome the band gap barrier and move to the CB area. The activation and transition of the electrons lead to holes (electron vacancy) left in the VB zone, as shown in Figure 32(b). For the formation of highly active electrons (e^-) in the CB and positive holes (h^+) in the VB, electron-hole pairs is then generated [as shown in Equation (2)].

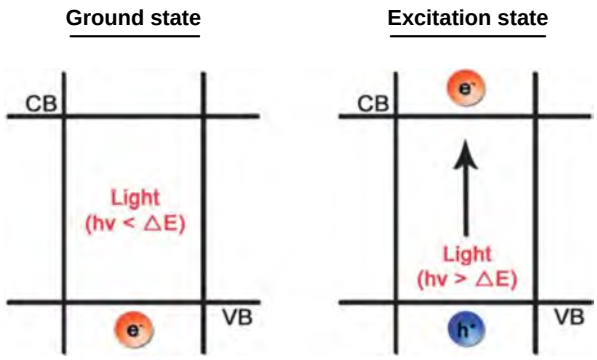

Figure 32. Schematic diagram of photo-excitation process on TiO_2 surface[215]

There are three possible routes for the reaction of formed electron-hole pairs, as shown in Figure 33: (1) electron-hole pairs may recombine on the surface or

within the photocatalyst (recombination) [Equation (2)]; (2) electrons spread onto the surface of photocatalyst and react with oxygen molecules (O_2), producing reactive oxygen radicals (–O, $–O_2$, $–O_3$), (photoreduction) [Equation (3)]; and (3) holes oxidize water molecules (H_2O) or adsorb hydroxide ions ($OH^–$) forming highly oxidizing hydroxyl radicals (–OH) (photooxidation) [Equation (4)]. The generated –O, $–O_2$, $–O_3$ and –OH can react with contaminants producing carbon dioxide, water or other harmless substances (Figure 33).

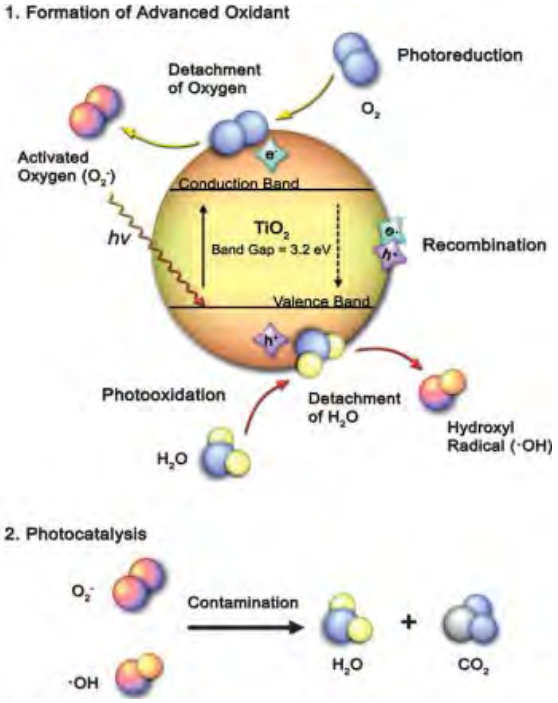

Figure 33. Schematic diagram of TiO_2 photocatalysis[215]

$$TiO_2 + h \rightarrow e^- + h^+ \quad (2)$$

$$e^- + h^+ \rightarrow TiO_2 \quad (3)$$

$$e^- + O_2 \rightarrow O_2^- \quad (4)$$

$$h^+ + H_2O \rightarrow OH + H^+ \quad (5)$$

Another mechanism for photocatalysis is photo-induced superhydrophilicity (Figure 34)[216,217]. The atomic binding energy of Ti and O is weakened due to the generation of $e^–$ and h^+ pairs after UV irradiation. Therefore, a Ti-O-Ti bond will be broken by water molecules easily and form two new Ti-OH bonds (Figure 34). Then, the external surface of TiO_2 becomes superhydrophilic and forms a sheet-like layer of moisture under water and UV irradiation. Thus a transparent protector against dirt is developed. In fact, TiO_2 film is not only hydrophilic but also amphiphilic after UV irradiation. Therefore adsorbed stains like oil can also be washed away when water rinsed over the superhydrophilic TiO_2[216,218].

Actually, the macroscopic manifestation of self-cleaning is a combined effect of photo-induced redox reactions and photo-induced superhydrophilicity. Although the redox reaction and superhydrophilicity are different processes, they could work simultaneously and are difficult to distinguish which is more important for achieving self-cleaning property. Several of novel applications have been developed depending on the synergetic effect of these two photocatalysis mechanisms. Concrete incorporated with nano-TiO_2 is successfully applied in the infrastructures like walls and pavements. It has proven very effective for cleaning of building appearance, disinfecting air of indoor and reduction of urban pollutants[214,219,220]. On one hand, the applications of TiO_2 concrete can maintain the aesthetic and luster of the building surface. For instance, a white photocatalytic concrete involving TiO_2 has been employed for the construction of the Dives in Misericordia Church in Rome, Italy (completed in 2003). During six years monitoring, only a slight difference of lightness values between internal and external walls was observed for the church in Rome. On the other hand, pavements made by the concrete containing nano-TiO_2 could trigger photocatalytic degradation of pollutant, such as nitrogen oxides

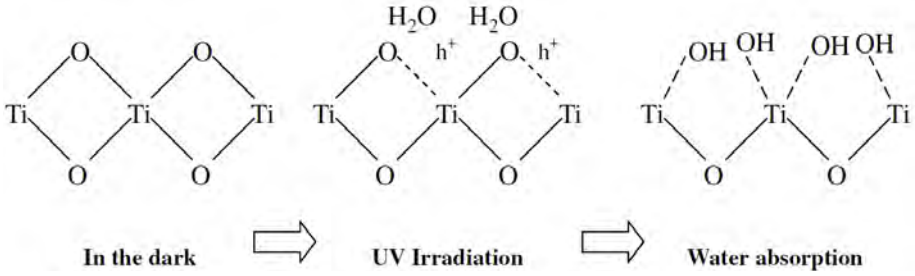

Figure 34. Photo-induced hydrophilic TiO_2 surface

(NO_X), volatile organic compounds (VOCs), aldehydes exhausted from combustion engine and industrial emissions. Detrimental NO_X can be transformed into uninjurious nitrate ions (NO_3^-) by TiO_2 and the final products of NO_3^- are easily washed away by the rains, as illustrated in Figure 35[221]. Poon and Cheung[222] evaluated the removal rate of NO by the paving blocks consisting of cement materials and TiO_2. The results indicated that an optimum mix design incorporating cement, sand, recycled glass and 10% TiO_2 could achieve a NO removal rate of 4.01 mg/hm^2. Another typical investigation of NO removed by the photocatalytic paving blocks obtained in laboratory is diagramed in Figure 36[223]. A block located in the center of Bergamo (Italy) city was re-paved using photocatalytic concrete paving blocks with a total area of about 12,000 m^2. An air monitoring campaign was then conducted for two weeks and showed an average decrease of NOx by 45% in daily time from 9 am to 5 pm[224]. In Guerville (France), three artificial street canyons covered by photocatalytic mortar were built to evaluate the performance against pollution. Continuous monitoring of NO_X was taken and showed that the NO_X concentrations observed in the TiO_2-treated canyon were 36.7-82.0% lower than that control canyons[225]. Additionally, the versatile nano-TiO_2 photocatalytic reactions can also eliminate the harmful organisms like bacteria and virus. Therefore, high standard hygiene demand can be satisfied in some venues where sterile conditions are extremely crucial.

The greatest advantage of photocatalytic self- cleaning concrete is the simple reaction conditions, which just requires sunlight, oxygen, water and TiO_2[213]. It is important that TiO_2 is well compatible with concrete without any adverse effect on mechanical properties. However, once they are used in real-life applications, the durability and efficiency of the photocatalytic self-cleaning concrete is still needed to be improved[226]. Furthermore, whether it is safe to apply the photocatalytic materials, especially the possible health effects of the by-products formed in incomplete photo-oxidation is still a controversy question[227].

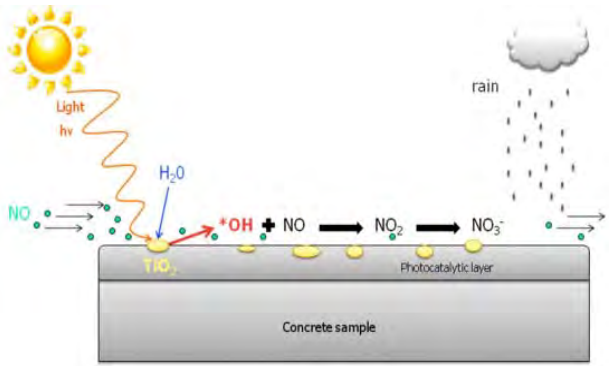

Figure 35. Illustration of the photocatalytic process[221]

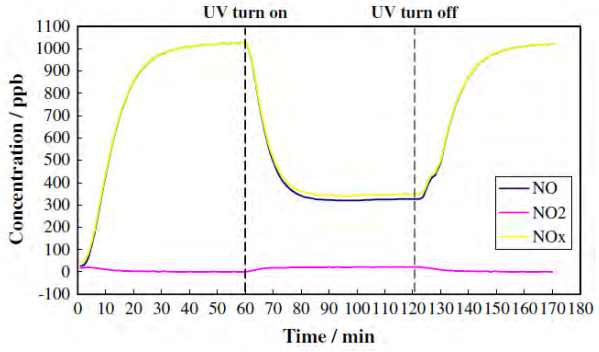

Figure 36. Photocatalytic NO_X removal results of photocatalytic paving block obtained in laboratory[223]

12. Self-Shaping Concrete

Three dimensional printing (3DP) technology, started in the late 1980's in Japan, has undergone rapid development in the last thirty years. As a subgroup of additive manufacturing process, three dimensional solid objects would be directly printed by 3DP technology from a digital model[228]. 3DP can meet the demand to manufacture any desired geometry shapes with the advantage of reducing material consumption and the associated labor force. To date, this technology has been successfully used in medical, aerospace and automotive manufacturing, *etc.*[229]. It is also promising for printing architectural and structural components.

A concrete printing machine and its delivery system are shown in Figure 37. The main operation principle

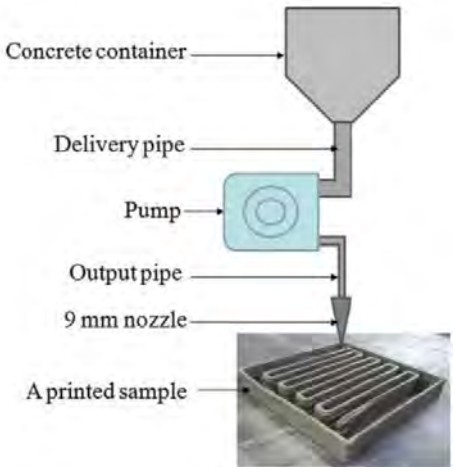

Figure 37. Schematic of concrete delivery system[230]

of 3DP concrete is that the nozzle circumnavigates following the predetermined paths with fresh concrete extruded out of it one layer at a time. When all layers are stacked one atop another, a completed 3D structure component is finished. Since framework and vibration are needless, concrete employed in 3DP is expected to combine the features of spray concrete with self-compacting concrete. So far, there is not a uniform definition for this special concrete and "self-shaping concrete" is named here based on its working process.

Self-shaping concrete as the "ink" of 3D printer, its workability is critical to the quality of printed constructions. The concrete should easily pass through the pipe-pump-nozzle system to extrude small concrete filaments. Meanwhile, sufficient adhesion and rigidity are required for concrete to print structures with a certain height or layers but no detrimental deformation occurs. From the point of rheology view, a relatively higher viscosity and lower yield stress are beneficial for concrete to achieve good plasticity. Moreover, the concrete should provide short setting time and high early strength[231]. As is well-known, the workability of concrete is mainly dominated by the mix proportions (*i.e.*, cementitious binder-aggregate ratio, water-binder ratio and the usage of admixture). Experiments based on the rheological approaches had been conducted by Le *et al.*[230] to achieve the optimum mix design of a high performance fiber-reinforced fine-aggregate self-shaping concrete. And the effects of admixtures such as retarder dosage, accelerator dosage and superplasticizer dosage on the workability and the variation of workability with time have also been studied. Since the structure of small concrete filaments is stacked layer by layer, the anisotropic structure is likely to act as small voids in their interlayers, leading to the weakened structural capability. Le *et al.*[232] tested the mechanical properties of self-printing concrete invented earlier in reference[230] and the results indicated that its mechanical strength significantly depends on the orientation of the load relative to the layers. The bond strength between concrete filaments can also largely influence the hardened properties of concrete. Plaster cementitious material with major ingredients of plaster, vinyl polymer and carbohydrate, humectant and water was adopted to print 3D concrete specimens and then the mechanical properties of these specimens were studied by Feng [as shown in Figure 38(a)]. Similar to the conclusions of Le *et al.*, there exists an apparent orthotropic behavior in the mechanical properties of specimens. Based on the experimental results, a model for the stress-strain relationship was proposed from uniaxial compressive test as shown in Figure 38(b)[233]. Gibbons applied rapid hardening Portland cement (RHPC) along with 3% PVA as powder and demineralized water as liquid to optimize the resolution and robustness of the uncured specimens. The measured modulus of rupture (MOR) value was apparently increased due to the reduced porosity after the specimens immersed in water for curing[234].

The application of 3DP technology has been reported in US, China and Europe in recent years. Architectural components showed in Figure 39 were constructed by different concrete printing technique in different country[235]. In 2015, an apartment block with five stories was shaped using glass fiber reinforced concrete by a Chinese company in Shanghai. And it is stated that the houses in apartment block were in full compliance with the relevant national standards[236]. Surprisingly, American scientists with the National

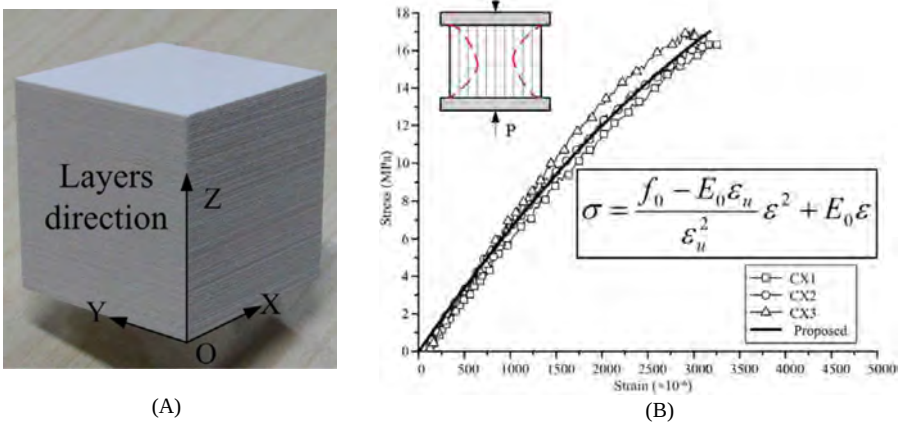

(A) (B)

Figure 38. (a) 3D printing concrete specimen; (b) stress-strain relationship under compression[233]

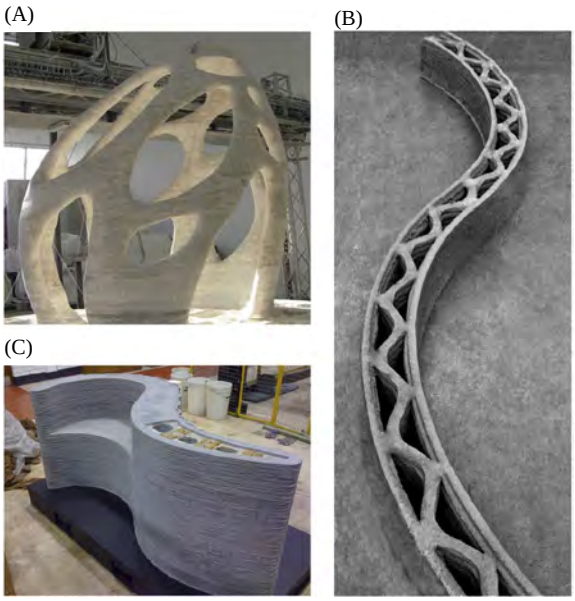

Figure 39. Examples of full scale builds from each process, (a) D-Shape, top left, (b) Contour Crafting, right and (c) Concrete Printing, bottom left[235]

Aeronautics and Space Agency (NASA) attempt to apply such a technique to build extraterrestrial settlement infrastructures using lunar soil as the raw material[237]. Simulations and experimental tests in vacuum condition have been conducted by European scientists to verify the feasibility of idea stated above[238].

Although 3D printing of full-scale construction is a new concept, it will create a new era of sustainable infrastructure. Structures with complex shapes can be fabricated by self-shaping concrete for its unnecessary of formwork and vibration. Thus, it can be realized in prompting construction speed, reducing labor force and engineering cost. However, there are a few studies focusing on the design and properties of this type of concrete. Self-shaping concrete requires good plasticity, short setting time, high early strength and it should bear its own weight and dynamic load during printing without distinct deformation. All these requirements cannot be satisfied simultaneously by conventional concrete design approaches. Further research should be conducted in the choice of raw materials, mix proportion design and the usage of admixtures.

13. Self-Draining Concrete

Self-draining concrete is the concrete containing interconnected voids inside to allow air or water moving through it. This kind of concrete is also known as pervious, porous and permeable concrete. When self-draining concrete is utilized as paving material, water is easy to percolate through paving matrix into the subsoil beneath. Thus, it is beneficial for conserving storm water and recharging groundwater.

Self-draining concrete is mainly consisted by cement paste and uniform coarse aggregate, little or no fine aggregate. A model for the structure of self-draining concrete is shown in Figure 40. The skeleton of concrete is formed by coarse aggregate and they are bound together by a limited amount of cement paste. Without the filling effect of fine aggregate, plenty of open voids exist among coarse aggregates and the typical size of voids ranges from 2 mm to 8 mm[239].

Excellent water permeability is the primary goal for designing self-draining concrete. In numerous studies, the water permeability of concrete has been proven to increase with increasing porosity. However, the compressive strength of concrete shows an adverse tendency with porosity[240-242]. In order to balance the conflict of permeability and compressive strength, the porosity of concrete is usually designed as 15%–25%

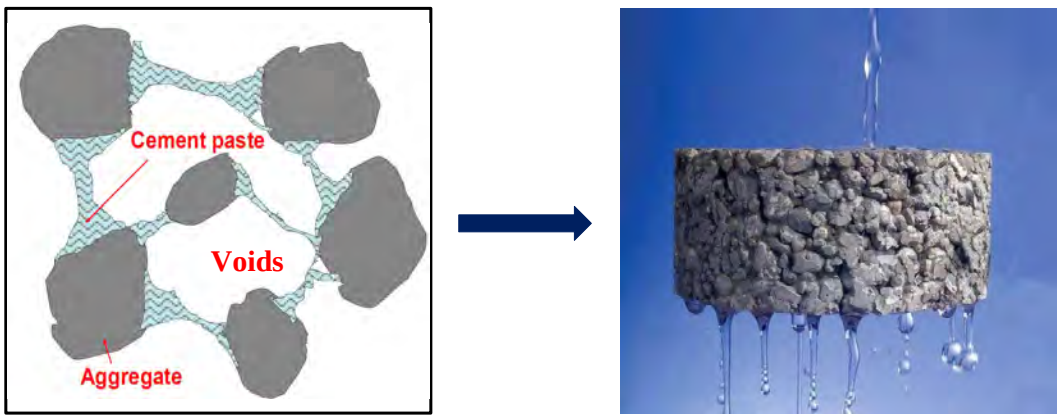

(A) (B)

Figure 40. (a) Model of self-draining concrete; (b) schematic diagram of permeability

based on the correlation between porosity and permeability, porosity and compressive strength, as shown in Figure 41. In this case, the compressive strength of concrete locates in 2.8–28.0 MPa at 7 d and water permeability coefficient range from 0.2 to 5.4 mm/s[243].

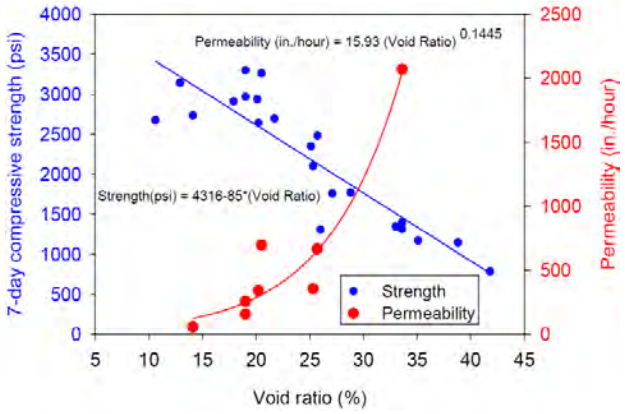

Figure 41. Relationship between strength, void ratio and permeability for several trial mixes of pervious concrete[244]

The concept of self-draining concrete has been around for nearly 60 years and it is often used under paving to help aid drainage. Since 1980s, self-draining concrete has been widely used in parking lots, squares, pedestrian walkways and other areas with light traffic. Recently, a UK building material company named Lafarge Tarmac has developed a new type of self-draining concrete with crushed granite as coarse aggregate. This concrete is permeable enough to let average 600 L/(min·m^2) water through to the ground level, as shown in Figure 42[245]. However, the application of self-draining concrete is still limited in heavy traffic roads by the relatively low strength[246-248]. Based on the structure model in Figure 1a, once the concrete is subjected to loading, the load will be transferred among the aggregates by cement paste. Although the strength of

Figure 42. Test of permeability of self-draining concrete[245]

aggregate is high enough, the cement paste and the interfacial transition zone (ITZ) are relatively weak for the thin binding layer. Therefore, the concrete always fails at the cement paste and ITZ. To improve the mechanical strength of pervious concrete while maintaining its high porosity, two methods are proposed. One is to increase the cement paste binder area. Smaller sized aggregate are employed to increase the number of particles per unit volume of concrete. The specific surface of aggregate and the binding area are then increased resulting in the improved strength. The other is to enhance the strength of cement binder. Except for applying high strength cement and reducing water cement ratio, supplementary materials such as silica fume, organic intensifiers and other special chemical reinforcing agents are usually used[249-250].

Self-draining concrete plays a key role in water purification and alleviating the drainage burden of sewage system. The Environmental Protection Agency of the United States has recognized the usage of self-draining concrete as one of the best management practices in storm-water conservation. In addition, the special porous structure of self-draining concrete generates excellent performance in antiskid, thermal insulation and acoustic absorption. However, the defects of poor mechanical strength and freeze-thaw resistance need to be paid enough attention. Besides, the open voids of the self-draining concrete structures prone to clogging and periodic cleaning or replace should be considered.

14. Self-Luminous Concrete

Recently, self-luminous concrete was developed in Michoacan University (Mexico) by Rubio *et al.* Self-luminous concrete (also called light-emitting cement) is solar-powered material that traps solar energy during the daytime and emits light at night. The whole process completes without consuming any electricity[251].

Conventional concrete is an opaque substance. When water is mixed with cement, crystal flakes are formed that doesn't allow light to pierce its interior. In order to address this issue, researchers paid much attention on modifying the micro-structure of cement aiming to eliminate the crystals. Eventually, a translucent gel-like substance enabling the adsorption of solar energy during the day and converting the energy into light at night was developed[251]. Detailed information about the compositions of raw materials and fabrication methods applied in self-luminous concrete is unavailable on the internet, since this new concrete

Figure 43. Self-luminous concrete could illuminate dark roads, highways without electricity[251,252]

is being patented.

Self-luminous concrete can be used in illuminating roads, pavements and bicycle lanes. Currently, this concrete is available in emitting blue and green light. Additionally, the brightness can be fine-tuned to meet the application requirements. Predictably, the role of self-luminous concrete in reducing the utilization of road lamp and decreasing the traffic accidents rate is of great significance in the future.

Most of the fluorescent materials are made of plastic and will be degraded by ultraviolet radiation after a few years. However, the researchers claimed that self-luminous concrete is sun resistant and its lifespan is estimated for as long as 100 years.

15. Conclusions

As a strong, versatile and economical material, concrete has been utilized in constructions world widely. It will still remain to be the indispensable and uppermost building materials for a long time in the future. Concrete has been endowed with new functions continually during the development and utilization. Intrinsically intelligent capacity of self-x concrete achieved new functions through combining traditional concrete with functional fillers or improving the composition of raw materials. This paper systematically introduced the intelligent concrete with performances of self-compacting, self-expanding, self-curing, self-sensing, self-healing, self-adjusting, self-damping, self-heating, self-sacrificing, self-cleaning, self-shaping, self-draining and self-luminous.

Intelligent concrete, as an innovative technology in the field of construction materials, injects novel vitality for construction materials despite challenges. The development of intelligent concrete will promote the application of concrete to a broader prospect and produce enormous socioeconomic performance. However, as an emerging technology, the investigation on intelligent concrete is still in primary stage and the following issues are needed to be solved before large-scale application.

(1) Properties of functional fillers are the key factors for achieving intelligence of concrete. Therefore, further exploration and exploitation of suitable functional fillers is crucial. The nanotechnology and bionic technology may provide inspiration for seeking more efficient functional fillers.

(2) Mechanical properties and durability of intelligent concrete are needed to be deeply analyzed. It is necessary for studying the intelligent concrete in a state of multi-axial stress, since existing investigations are always confined in the range of uniaxial stress which is far from the engineering applications. Moreover, the effect of different environment factors on the functionality and durability of intelligent concrete should be further researched.

(3) Although there are numerous reasonable explanations and forecasting models, the mechanism of intelligent concrete is still ambiguous due to the complex system of intelligent concretes in multi-component, multi-phase, and multi-scale characteristics. Therefore, more precise constitutive model based on advanced experimental facilities and numerical analysis is needed to be established for describing and predicting the behaviors of intelligent concrete.

(4) Lack of unitary criterion makes it difficult for intelligent concrete to be normatively designed and tested, and further limits the applications. Thus, a uniform standard providing method, guidance and specification for the research and application of intelligent concrete is urgent to be established.

In general, intrinsically intelligent concrete is an in-

terdisciplinary field involving bionics, physics, chemistry, material science and civil engineering, *etc*. Therefore, cross-disciplinary collaboration and communication among researchers with different expertise will be of utmost importance to fulfill further investigation on intelligent concrete. The utilization of intelligent concrete is a logical choice for maintaining sustainable development of concrete constructions and developing intelligent infrastructures, thus building Smart Cities and Smarter Planet. Undoubtedly, intelligent concrete will bring a deep revolution to the field of construction materials and infrastructures. Its widespread applications will make beneficial effects on society, economics and environment in the future.

Conflict of Interest and Funding

The authors declared that they have no conflicts of interest to this work.

The authors thank the funding supported from the National Science Foundation of China (51578110 and 51428801).

References

1. Aitcin P C, 2000, Cements of yesterday and today: Concrete of tomorrow, *Cement and Concrete Research*, vol.30(9): 1349–1359. http://dx.doi.org/10.1016/S0008-8846(00)00365-3
2. Spillman Jr W B, Sirkis J S and Gardiner P T, 1996, Smart materials and structures: What are they? *Smart Materials and Structures*, vol.5(3): 247. https://doi.org/10.1088/0964-1726/5/3/002
3. Sun M, Li Z and Liu Q, 2002, The electromechanical effect of carbon fiber reinforced cement, *Carbon*, vol.40(12): 2273–2275. http://dx.doi.org/10.1016/S0008-6223(02)00189-6
4. Han B, Wang Y, Dong S, *et al*., 2015, Smart concretes and structures: A review, *Journal of Intelligent Material Systems and Structures*, vol.26(11): 1303–1345. https://doi.org/10.1177/1045389X15586452
5. The Self-Compacting Concrete European Project Group, 2005, The European Guidelines for Self-Compacting Concrete, viewed (01/15/2016), http://www.efnarc.org/pdf/SCCGuidelinesMay2005.pdf
6. Domone P L, 2007, A review of the hardened mechanical properties of self-compacting concrete, Cement and Concrete Composites, vol.29(1): 1–12. http://dx.doi.org/10.1016/j.cemconcomp.2006.07.010
7. Najim K B and Hall M R, 2010, A review of the fresh/hardened properties and applications for plain- (PRC) and self-compacting rubberised concrete (SCRC), Construction and Building Materials, vol.24(11): 2043–2051. http://dx.doi.org/10.1016/j.conbuildmat.2010.04.056
8. Okamura H and Ouchi M, 2003, Self-compacting concrete, *Journal of Advanced Concrete Technology*, vol.1(1): 5–15.https://doi.org/10.3151/jact.1.5
9. CECS 203：2006 (2006), Technical Specifications for self compacting concrete Application, Standardization Institute of Chinese Construction Standard, Beijing, China.
10. Persson B, 2001, A comparison between mechanical properties of self-compacting concrete and the corresponding properties of normal concrete, *Cement and Concrete Research*, vol.31(2): 193–198. http://dx.doi.org/10.1016/S0008-8846(00)00497-X
11. Nagamoto N and Ozawa K, 1999, Mixture properties of self-compacting, high-performance concrete, *ACI Special Publication*, vol.172: 623–636.
12. Kesler C E and Pfeifer D W, 1970, Expansive cement concretes-present state of knowledge.
13. Nagataki S and Gomi H, 1998, Expansive admixtures (mainly ettringite), *Cement and Concrete Composites*, vol.20(2–3): 163–170. http://dx.doi.org/10.1016/S0958-9465(97)00064-4
14. Wu Z W and Zhang H Z, 1990, Expansive concrete, China Railway Publishing House, Beijing, China. (in Chinese)
15. Carballosa P, Calvo J G and Revuelta D, *et al*., 2015, Influence of cement and expansive additive types in the performance of self-stressing and self-compacting concretes for structural elements, Construction and Building Materials, vol.93: 223–229. http://dx.doi.org/10.1016/j.conbuildmat.2015.05.113
16. Klein A, Karby T and Polivka M, 1961, Properties of an expansive cement for chemical prestressing, *ACI Materials Journal*, vol.58: 59.
17. Lees J M, Gruffydd-Jones B and Burgoyne CJ, 1995, Expansive cement couplers: A means of pre-tensioning fibre-reinforced plastic tendons, *Construction and Building Materials*, vol.9(6): 413–423. http://dx.doi.org/10.1016/0950-0618(95)00070-4
18. Huang K, Deng M, Mo L, *et al*., 2013, Early age stability of concrete pavement by using hybrid fiber together with MgO expansion agent in high altitude locality, *Construction and Building Materials*, vol.48: 685–690. http://dx.doi.org/10.1016/j.conbuildmat.2013.07.089
19. Yan P and Qin X, 2001, The effect of expansive agent and possibility of delayed ettringite formation in shrinkage-compensating massive concrete, *Cement and Concrete Research*, vol.31(2): 335–337. http://dx.doi.org/10.1016/S0008-8846(00)00453-1
20. Yan P, Zheng F, Peng J, *et al*., 2004, Relationship be-

tween delayed ettringite formation and delayed expansion in massive shrinkage-compensating concrete, *Cement and Concrete Composites*, vol.26(6): 687–693. http://dx.doi.org/10.1016/S0958-9465(03)00060-X

21. Mo L, Deng M and Tang M, 2010, Effects of calcination condition on expansion property of MgO-type expansive agent used in cement-based materials, *Cement and Concrete Research*, vol.40(3): 437–446. http://dx.doi.org/10.1016/j.cemconres.2009.09.025
22. Mehta P K and Pirtz D, 1980, Magnesium oxide additive for producing selfstress in mass concrete, In 7th International Congress on the Chemistry of Cement Vol. III, Paris, 6–9.
23. Mo L, Deng M, Tang M, *et al*., 2014, MgO expansive cement and concrete in China: Past, present and future, *Cement and Concrete Research*, vol.57: 1–12. http://dx.doi.org/10.1016/j.cemconres.2013.12.007
24. Chatterji S, 1995, Mechanism of expansion of concrete due to the presence of dead-burnt CaO and MgO, *Cement and Concrete Research*, vol.25(1): 51–56. http://dx.doi.org/10.1016/0008-8846(94)00111-B
25. Weber S and Reinhardt H W, 1997, A new generation of high performance concrete: Concrete with autogenous curing, *Advanced Cement Based Materials*, vol.6(2): 59–68. http://dx.doi.org/10.1016/S1065-7355(97)00009-6
26. Jensen O M and Hansen P F, 2001, Water-entrained cement-based materials: I. Principles and theoretical background, *Cement and Concrete Research*, vol.31(4): 647–654. http://dx.doi.org/10.1016/S0008-8846(01)00463-X
27. Powers T C and Brownyard T L, 1946, Studies of the physical properties of hardened Portland cement paste. Bulletin 22.
28. Neville A M, 1995, Properties of concrete, Wiley Press.
29. Henkensiefken R, Castro J, Bentz D, *et al*., 2009, Water absorption in internally cured mortar made with water-filled lightweight aggregate, *Cement and Concrete Research*, vol.39(10): 883–892. http://dx.doi.org/10.1016/j.cemconres.2009.06.009
30. Jensen O M and Hansen P F, 2002, Water-entrained cement-based materials: II. Experimental observations, *Cement and Concrete Research*, vol.32(6): 973–978. http://dx.doi.org/10.1016/S0008-8846(02)00737-8
31. Geiker M R, Bentz D P and Jensen O M, 2004) Mitigating autogenous shrinkage by internal curing, *ACI Special Publications*: 143–154.
32. Piérard J, Pollet V and Cauberg N, *et al*., 2006, Mitigating autogenous shrinkage in HPC by internal curing using superabsorbent polymers, In RILEM proceedings PRO, 97–106.
33. Craeye B, 2006, Reduction of autogenous shrinkage of concrete by means of internal curing, Master Dissertation, Ghent University (in Dutch).
34. Bentz D P, 2007, Internal curing of high-performance blended cement mortars, *ACI Materials Journal*, vol.104: 408.
35. Lura P, 2003, Autogenous deformation and internal curing of concrete: TU Delft, Delft University of Technology.
36. Craeye B, Geirnaert M and De Schutter G, 2011, Super absorbing polymers as an internal curing agent for mitigation of early-age cracking of high-performance concrete bridge decks, Construction and Building Materials, vol.25(1): 1–13. http://dx.doi.org/10.1016/j.conbuildmat.2010.06.063
37. Hasholt M T, Jensen O M, Kovler K, *et al*., 2012, Can superabsorent polymers mitigate autogenous shrinkage of internally cured concrete without compromising the strength? *Construction and Building Materials*, vol.31: 226–230. http://dx.doi.org/10.1016/j.conbuildmat.2011.12.062
38. Bentz D P, 2009, Influence of internal curing using lightweight aggregates on interfacial transition zone percolation and chloride ingress in mortars, *Cement and Concrete Composites*, vol.31(5): 285–289. http://dx.doi.org/10.1016/j.cemconcomp.2009.03.001
39. Liu X, Chia K S and Zhang M, 2010, Development of lightweight concrete with high resistance to water and chloride-ion penetration, *Cement and Concrete Composites*, vol.32(10): 757–766.
40. Liu X, Chia K S and Zhang M, 2011, Water absorption, permeability, and resistance to chloride-ion penetration of lightweight aggregate concrete, *Construction and Building Materials*, vol.25(1): 335–343. http://dx.doi.org/10.1016/j.conbuildmat.2010.06.020
41. Bentz D P and Jensen O M, 2004, Mitigation strategies for autogenous shrinkage cracking, Cement and Concrete Composites, vol.26(6): 677–685. http://dx.doi.org/10.1016/S0958-9465(03)00045-3
42. Lura P, Ye G, Cnudde V, *et al*., 2008, Preliminary results about 3D distribution of superabsorbent polymers in mortars, In Proc Int Conf Microstructure-related durability of cementitious composites, RILEM Pro, 1341–1348.
43. Oh B H, Cha S W, Jang BS, *et al*., 2002, Development of high-performance concrete having high resistance to chloride penetration, *Nuclear Engineering and Design*, vol.212(1–2): 221–231. http://dx.doi.org/10.1016/S0029-5493(01)00484-8
44. Villarreal V H and Crocker D A, 2007, Better pavements through internal hydration, *Concrete International*, vol.29: 32–36.
45. Bentz D P and Weiss W J, 2011, Internal curing: A 2010 state-of-the-art review: US Department of Commerce,

National Institute of Standards and Technology. https://doi.org/10.6028/NIST.IR.7765

46. Sun S, Yu X and Han B, 2014, Sensing mechanism of self-monitoring CNTs cementitious composite, *Journal of Testing and Evaluation*, vol.42(1): 1–5. https://doi.org/10.1520/JTE20120302
47. Vera-Agullo J, Chozas-Ligero V, Portillo-Rico D, *et al*., 2009, Mortar and concrete reinforced with nanomaterials, *Nanotechnology in Construction*, vol.3: 383–388.
48. Banthia N, Djeridane S and Pigeon M, 1992, Electrical resistivity of carbon and steel micro-fiber reinforced cements, *Cement and Concrete Research*, vol.22(5): 804–814. http://dx.doi.org/10.1016/0008-8846(92)90104-4
49. Han B, Ding S and Yu X, 2015, Intrinsic self-sensing concrete and structures: A review, *Measurement*, vol.59: 110–128. http://dx.doi.org/10.1016/j.measurement.2014.09.048
50. Han B, Han B and Yu X, 2009, Experimental study on the contribution of the quantum tunneling effect to the improvement of the conductivity and piezoresistivity of a nickel powder-filled cement-based composite, *Smart Materials and Structures*, vol.18, 065007(7pp). http://dx.doi.org/10.1088/0964-1726/18/6/065007
51. Sun M, Li Z, Mao Q, *et al*., 1998, Study on the hole conduction phenomenon in carbon fiber-reinforced concrete, *Cement and Concrete Research*, vol.28(4): 549–554.http://dx.doi.org/10.1016/S0008-8846(98)00011-8
52. Han B, Han B, Yu X, *et al*., 2011, Ultrahigh pressure-sensitive effect induced by field emission at sharp nano-tips on the surface of spiky spherical nickel powders, *Sensor Letters*, vol.9: 1629–1635. https://doi.org/10.1166/sl.2011.1719
53. Han B, Zhang K, Yu X, *et al*., 2012, Electrical characteristics and pressure-sensitive response measurements of carboxyl MWNT/cement composites, *Cement and Concrete Composites*, vol.34: 794–800. http://dx.doi.org/10.1016/j.cemconcomp.2012.02.012
54. Han B, Zhang L, Sun S, et al., 2015, Electrostatic self-assembly CNT/NCB composite fillers reinforced cement-based materials with multifunctionality, Composites Part A: Applied Science and Manufacturing, vol.79: 103–115. http://dx.doi.org/10.1016/j.compositesa.2015.09.016
55. Han B, Yu X, Kwon E, *et al*., 2012, Effects of CNT concentration level and water/cement ratio on the piezoresistivity of CNT/cement composites, *Journal of Composite Materials*, vol.46(1): 19–25. http://dx.doi.org/10.1177/0021998311401114
56. Kim H, Park I and Lee H, 2014, Improved piezoresistive sensitivity and stability of CNT/cement mortar composites with low water-binder ratio, *Composite Structures*, vol.116: 713–719. http://dx.doi.org/10.1016/j.compstruct.2014.06.007
57. Han B, Yu X, Kwon E, et al., 2010, Piezoresistive MWNTs filled cement-based composites, Sensor Letters, vol.8(2): 344–348.https://doi.org/10.1166/sl.2010.1275
58. Materazzi A L, Ubertini F and D'Alessandro A, 2013, Carbon nanotube cement-based transducers for dynamic sensing of strain, *Cement and Concrete Composites*, vol.37: 2–11. http://dx.doi.org/10.1016/j.cemconcomp.2012.12.013
59. Stauffer D and Aharony A, 1994, Introduction to percolation theory: CRC press.
60. Han B, Zhang L, Zhang C, *et al*., 2016, Reinforcement effect and mechanism of carbon fibers to mechanical and electrically conductive properties of cement-based materials, *Construction and Building Materials*, vol.125: 179–189. http://dx.doi.org/10.1016/j.conbuildmat.2016.08.063
61. Dong S, Han B, Ou J, *et al*., 2016, Electrically conductive behaviors and mechanisms of short-cut super-fine stainless wire reinforced reactive powder concrete, *Cement and Concrete Composites*, vol.72:48–65. http://dx.doi.org/10.1016/j.cemconcomp.2016.05.022
62. Chen P and Chung D, 1993, Carbon fiber reinforced concrete as an electrical contact material for smart structures, *Smart Materials and Structures*, vol.2(1): 181. https://doi.org/10.1088/0964-1726/2/1/004
63. Muto N, Yanagida H, Nakatsuji T, *et al*., 1992, Design of intelligent materials with self-diagnosing function for preventing fatal fracture, *Smart Materials and Structures*, vol.1(4): 324. https://doi.org/10.1088/0964-1726/1/4/007
64. Fu X and Chung D, 1998, Radio-wave-reflecting concrete for lateral guidance in automatic highways, *Cement and Concrete Research*, vol.28(6): 795–801. http://dx.doi.org/10.1016/S0008-8846(98)00057-X
65. Sun M, Li Z, Mao Q, *et al*., 1998, Thermoelectric percolation phenomena in carbon fiber-reinforced concrete, *Cement and Concrete Research*, vol.28(12): 1707–1712. http://dx.doi.org/10.1016/S0008-8846(98)00161-6
66. Sun M, Li Z, Mao Q, *et al*., 1999, A study on thermal self-monitoring of carbon fiber reinforced concrete, *Cement and Concrete Research*, vol.29(5): 769–771. http://dx.doi.org/10.1016/S0008-8846(99)00006-X
67. Sun M, Li Z, Liu Q, *et al*., 2000, A study on thermal self-diagnostic and self-adaptive smart concrete structures, *Cement and Concrete Research*, vol.30(8): 1251–1253.http://dx.doi.org/10.1016/S0008-8846(00)00284-2
68. García-Macías E, D'Alessandro A, Castro-Triguero R, *et al*., 2017, Micromechanics modeling of the electrical conductivity of carbon nanotube cement-matrix composites. *Composites Part B: Engineering*, vol.108: 451–

469.http://dx.doi.org/10.1016/j.compositesb.2016.10.025
69. Wen S and Chung D, 2001, Cement-based thermocouples, *Cement and Concrete Research*, vol.31(3): 507–510.http://dx.doi.org/10.1016/S0008-8846(00)00391-4
70. Han B, Wang Y, Sun S, *et al.*, 2014, Nanotip-induced ultrahigh pressure-sensitive composites: principles, properties and applications, *Composites Part A: Applied Science and Manufacturing*, vol.59: 105–114. http://dx.doi.org/10.1016/j.compositesa.2014.01.005
71. Han B, Guan X and Ou J, 2007, Electrode design, measuring method and data acquisition system of carbon fiber cement paste piezoresistive sensors, *Sensors and Actuators A: Physical*, vol.135(2): 360–369. http://dx.doi.org/10.1016/j.sna.2006.08.003
72. Han B, Yu X and Ou J, 2010, Effect of water content on the piezoresistivity of MWNT/cement composites, *Journal of Materials Science*, vol.45(14): 3714–3719. https://doi.org/10.1007/s10853-010-4414-7
73. Han B, Zhang K, Burnham T, *et al.*, 2013, Integration and road tests of aself-sensing CNT concrete pavement system for traffic detection, *Smart Materials and Structures*, vol.22, 015020 (8pp). http://dx.doi.org/10.1088/0964-1726/22/1/015020
74. Han B, Sun S, Ding S, *et al.*, 2015, Review of nanocarbon-engineered multifunctional cementitious composites, *Composites Part A: Applied Science and Manufacturing*, vol.70: 69–81. http://dx.doi.org/10.1016/j.compositesa.2014.12.002
75. Han B, Han B and Ou J, 2009, Experimental study on use of nickel powder-filled Portland cement-based composite for fabrication of piezoresistive sensorswith high sensitivity, *Sensors and Actuators: A physical*, vol. 149(1): 51–55. http://dx.doi.org/10.1016/j.sna.2008.10.001
76. Ou J and Han B, 2009, Piezoresistive cement-based strain sensors and self-sensing concrete components, *Journal of Intelligent Material Systems and Structures*, vol.20 (3): 329–336. http://dx.doi.org/10.1177/1045389X08094190
77. Han B, Han B, Yu X, *et al.*, 2009, Piezoresistive characteristic model of nickel/cement composites based on field emission effect and inter-particle separation, *Sensor Letters*, vol.7(6): 1044–1050. https://doi.org/10.1166/sl.2009.1232
78. Fu X, Lu W and Chung D, 1998, Improving the strain-sensing ability of carbon fiber-reinforced cement by ozone treatment of the fibers, *Cement and Concrete Research*, vol.28(2): 183–187. http://dx.doi.org/10.1016/S0008-8846(97)00265-2
79. Wang W, Dai H and Wu S, 2008, Mechanical behavior and electrical property of CFRC- strengthened RC beams under fatigue and monotonic loading.*Materials Science and Engineering A*, vol.479: 191–196. http://dx.doi.org/10.1016/j.msea.2007.06.046
80. Wang S, Liang R, Wang B, *et al.*, 2009, Dispersion and thermal conductivity of carbon nanotube composites, *Carbon*, vol.47(1): 53–57. http://dx.doi.org/10.1016/j.carbon.2008.08.024
81. Konsta-Gdoutos M S, Metaxa Z S and Shah S P, 2010, Highly dispersed carbon nanotube reinforced cement based materials, *Cement and Concrete Research*, vol.40(7): 1052–1059. http://dx.doi.org/10.1016/j.cemconres.2010.02.015
82. Han B, Zhang K, Yu X, *et al.*, 2011, Fabrication of piezoresistive CNT/CNF cementitious composites with superplasticizer as dispersant, *Journal of Materials in Civil Engineering*, vol.24(6): 658–665. https://doi.org/10.1061/(ASCE)MT.1943-5533.0000435
83. Han B, Yu X and Ou J, 2011, Multifunctional and smart carbon nanotube reinforced cement-based materials, *Nanotechnology in Civil Infrastructure*: 1–47.
84. Han B, Yu X and Ou J, 2014, Self-sensing concrete in smart structures: Elsevier.
85. Chen P W and Chung D, 1995, Carbon-fiber-reinforced concrete as an intrinsically smart concrete for damage assessment during dynamic loading, *Journal of the American Ceramic Society*, vol.78(3): 816–818. https://doi.org/10.1111/j.1151-2916.1995.tb08254.x
86. Zhang L, Ding S, Sun S, *et al.*, 2016, Chapter 2: Nano-scale behavior and nano-modification of cement and concrete materials. Book: Advanced Research on Nanotechnology for Civil Engineering Applications, Publisher: IGI Global, Editors: Anwar Khitab, Waqas Anwar. 28–79.
87. Han B, Yu Y, Han B, *et al.*, 2008, Development of a wireless stress/strain measurement system integrated with pressure-sensitive nickel powder-filled cement-based sensors, *Sensors and Actuators: A physical*, vol.147(2): 536–543. http://dx.doi.org/10.1016/j.sna.2008.06.021
88. Han B and Ou J, 2007, Embedded piezoresistive cement-based stress/strain sensor, *Sensors and Actuators: A physical*, vol.138(2): 294–298. http://dx.doi.org/10.1016/j.sna.2007.05.011
89. Wang W, Wu S and Dai H, 2006, Fatigue behavior and life prediction of CFRC under cyclic flexural loading, *Materials Science and Engineering*, vol.434: 347–351. http://dx.doi.org/10.1016/j.msea.2006.07.080
90. Wu S, Dai H and Wang W, 2007, Effect of CFRC layers on the electrical properties and failure mode of RC beams strengthened with CFRC composites, *Smart Materials and Structures*, vol.16(6): 2056–2062. http://dx.doi.org/10.1088/0964-1726/16/6/008
91. Han B, Sun S，Ding S, *et al.*, 2015, Chapter 8: Nano

carbon materials filled cementitious composites: fabrication, properties and application. Book: Innovative Developments of Advanced Multifunctional Nanocomposites in Civil and Structural Engineering, Publisher: Elsevier, Editors: Kenneth J. Loh, Satish Nagarajaiah. 153–181.

92. Han B, Yu X and Kwon E, 2009, A self-sensing carbon nanotube/cement composite for traffic monitoring, *Nanotechnology*, vol.20(44): 445501. https://doi.org/10.1088/0957-4484/20/44/445501
93. Han B, Zhang K, Yu X, *et al*., 2011, Nickel particle-based self-sensing pavement for vehicle detection, *Measurement*, vol.44(9): 1645–1650. http://dx.doi.org/10.1016/j.measurement.2011.06.014
94. Yunovich M and Thompson NG, 2003, Corrosion of highway bridges: Economic impact and control methodologies, *Concrete International*, vol.25: 52–57.
95. Poole B, 2012, Biomimetics: Borrowing from biology, viewed September 9, 2012, http://www.thenakedscientists.com/HTML/articles/article/biomimeticsborrowingfrombiology/
96. Zwaag S, 2008, Self healing materials: An alternative approach to 20 centuries of materials science: Springer Science+ Business Media BV.
97. Ghosh S K, 2009, Self-healing materials: fundamentals, design strategies, and applications: John Wiley and Sons.
98. Kishi T, Ahn T H, Hosoda A, *et al*., 2007, Self-healing behavior by cementitious recrystallization of cracked concrete incorporating expansive agent, In First international conference on self-healing materials. Springer, Dordrecht.
99. Edvardsen C, 1999, Water permeability and autogenous healing of cracks in concrete, *ACI Materials Journal*, vol.96: 448–454.
100. Neville A, 2002, Autogenous healing-a concrete miracle? *Concrete International*, vol.24: 76–82.
101. Yang Y Z, Lepech M D, Yang E H, *et al*., 2009, Autogenous healing of engineered cementitious composites under wet-dry cycles, *Cement and Concrete Research*, vol.39(5): 382–390. http://dx.doi.org/10.1016/j.cemconres.2009.01.013
102. Termkhajornkit P, Nawa T, Yamashiro Y, *et al*., 2009, Self-healing ability of fly ash–cement systems, *Cement and Concrete Composites*, vol.31(3): 195–203. http://dx.doi.org/10.1016/j.cemconcomp.2008.12.009
103. Van Tittelboom K, Gruyaert E, Rahier H, *et al*., 2012, Influence of mix composition on the extent of autogenous crack healing by continued hydration or calcium carbonate formation, *Construction and Building Materials*, vol.37: 349–359. http://dx.doi.org/10.1016/j.conbuildmat.2012.07.026
104. Snoeck D, Steuperaert S, Van Tittelboom K, *et al*., 2012, Visualization of water penetration in cementitious materials with superabsorbent polymers by means of neutron radiography, *Cement and Concrete Research*, vol.42(8): 1113–1121. http://dx.doi.org/10.1016/j.cemconres.2012.05.005
105. Snoeck D and De Belie N, 2015, Repeated autogenous healing in strain-hardening cementitious composites by using superabsorbent polymers, *Journal of Materials in Civil Engineering*, vol.28(1): 4015086. https://doi.org/10.1061/(ASCE)MT.1943-5533.0001360
106. Yildirim G, Sahmaran M and Ahmed HU, 2014, Influence of hydrated lime addition on the self-healing capability of high-volume fly ash incorporated cementitious composites, *Journal of Materials in Civil Engineering*, vol.27(6): 4014187. https://doi.org/10.1061/(ASCE)MT.1943-5533.0001145
107. Granger S, Loukili A, Pijaudier-Cabot G, *et al*., 2007, Experimental characterization of the self-healing of cracks in an ultra high performance cementitious material: Mechanical tests and acoustic emission analysis, *Cement and Concrete Research*, vol.37(4): 519–527. http://dx.doi.org/10.1016/j.cemconres.2006.12.005
108. Jacobsen S and Sellevold EJ, 1996, Self healing of high strength concrete after deterioration by freeze/thaw, *Cement and Concrete Research*, vol.26(1): 55–62. http://dx.doi.org/10.1016/0008-8846(95)00179-4
109. Granger S, Pijaudier-Cabot G and Loukili A, 2007, Mechanical behavior of self-healed ultra high performance concrete: from experimental evidence to modeling, In The 6th international conference on fracture mechanics of concrete and concrete structures, Catalina, Italy.
110. Li V C, Wang S and Wu C, 2001, Tensile strain-hardening behavior of polyvinyl alcohol engineered cementitious composite (PVA-ECC), *ACI Materials Journal*, vol.98: 483–492.
111. Dhawale A W and Joshi V P, 2013, Engineered cementitious composites for structural applications, *International journal of application or Innovation in Engineering & Management*, vol.2: 198–205.
112. Snoeck D and De Belie N, 2012, Mechanical and self-healing properties of cementitious composites reinforced with flax and cottonised flax, and compared with polyvinyl alcohol fibres, *Biosystems Engineering*, vol.111(4): 325–335. http://dx.doi.org/10.1016/j.biosystemseng.2011.12.005
113. Snoeck D, Smetryns P and De Belie N, 2015, Improved multiple cracking and autogenous healing in cementitious materials by means of chemically-treated natural fibres, *Biosystems Engineering*, vol.139: 87–99. http://dx.doi.org/10.1016/j.biosystemseng.2015.08.007
114. White S R, Sottos N R, Geubelle P H, *et al*., 2001, Autonomic healing of polymer composites, *Nature*, vol.409:

794–797. https://doi.org/10.1038/35057232

115. Dry C, 1994, Matrix cracking repair and filling using active and passive modes for smart timed release of chemicals from fibers into cement matrices, *Smart Materials and Structures*, vol.3(2): 118. https://doi.org/10.1088/0964-1726/3/2/006
116. Mihashi H, Kaneko Y, Nishiwaki T, *et al*., 2001, Fundamental study on development of intelligent concrete characterized by self-healing capability for strength, *Transactions of the Japan Concrete Institute*, vol.22: 441–450.
117. Ramachandran S K, Ramakrishnan V and Bang S S, 2001, Remediation of concrete using micro-organisms, *ACI Materials Journal*, 98: 3–9.
118. Ramakrishnan V, 2007, Performance characteristics of bacterial concrete—a smart biomaterial, In Proceedings of the First International Conference on Recent Advances in Concrete Technology, 67–78.
119. Van Tittelboom K and De Belie N, 2010, Self-healing concrete: Suitability of different healing agents, Int. J. 3R's 1: 12–21.
120. Thao T D P, 2011, Quasi-brittle self-healing materials: numerical dodelling and applications in civil engineering, PhD thesis, National University of Singapore, Singapore.
121. Yang Z, Hollar J, He X, *et al*., 2011, A self-healing cementitious composite using oil core/silica gel shell microcapsules, *Cement and Concrete Composites*, vol. 33(4): 506–512. http://dx.doi.org/10.1016/j.cemconcomp.2011.01.010
122. Pelletier M M, Brown R, Shukla A, *et al*., 2011, Self-healing concrete with a microencapsulated healing agent, *Technical Report*, Kingston.
123. Jonkers H M, Thijssen A, Muyzer G, *et al*., 2010, Application of bacteria as self-healing agent for the development of sustainable concrete, *Ecological Engineering*, vol.36(2): 230–235. http://dx.doi.org/10.1016/j.ecoleng.2008.12.036
124. Wang J, Van Tittelboom K, De Belie N, *et al*., 2012, Use of silica gel or polyurethane immobilized bacteria for self-healing concrete, *Construction and Building Materials*, vol.26(1): 532–540. http://dx.doi.org/10.1016/j.conbuildmat.2011.06.054
125. Chan Y N, Luo X and Sun W, 2000, Compressive strength and pore structure of high-performance concrete after exposure to high temperature up to 800 °C, *Cement and Concrete Research*, vol.30(2): 247–251. http://dx.doi.org/10.1016/S0008-8846(99)00240-9
126. Peng G, Yang W, Zhao J, *et al*., 2006, Explosive spalling and residual mechanical properties of fiber-toughened high-performance concrete subjected to high temperatures, *Cement and Concrete Research*, vol.36(4): 723–727. http://dx.doi.org/10.1016/j.cemconres.2005.12.014
127. Kodur V, Cheng F, Wang T, *et al*., 2003, Effect of strength and fiber reinforcement on fire resistance of high-strength concrete columns, *Journal of Structural Engineering*, vol.129(2): 253–259. https://doi.org/10.1061/(ASCE)0733-9445(2003)129:2(253)
128. Kalifa P, Menneteau F and Quenard D, 2000, Spalling and pore pressure in HPC at high temperatures, *Cement and Concrete Research*, vol.30(12): 1915–1927. http://dx.doi.org/10.1016/S0008-8846(00)00384-7
129. Hertz K D, 1992, Danish investigations on silica fume concretes at elevated temperatures, *ACI Materials Journal*, vol.89: 345–347.
130. Ahmed G N and Hurst J P, 1997, An analytical approach for investigating the causes of spalling of high-strength concrete at elevated temperatures, In International Workshop on Fire Performance of High-Strength Concrete, 13–14.
131. Han C, Hwang Y, Yang S, *et al*., 2005, Performance of spalling resistance of high performance concrete with polypropylene fiber contents and lateral confinement, *Cement and Concrete Research*, vol.35(9): 1747–1753. http://dx.doi.org/10.1016/j.cemconres.2004.11.013
132. Lau A and Anson M, 2006, Effect of high temperatures on high performance steel fibre reinforced concrete, *Cement and Concrete Research*, vol.36(9): 1698–1707. http://dx.doi.org/10.1016/j.cemconres.2006.03.024
133. Xiao J and Falkner H, 2006, On residual strength of high-performance concrete with and without polypropylene fibres at elevated temperatures, *Fire Safety Journal*, vol.41(2): 115–121. http://dx.doi.org/10.1016/j.firesaf.2005.11.004
134. Kalifa P, Chene G and Galle C, 2001, High-temperature behaviour of HPC with polypropylene fibres: From spalling to microstructure, *Cement and Concrete Research*, vol.31(10): 1487–1499. http://dx.doi.org/10.1016/S0008-8846(01)00596-8
135. Chen B and Liu J, 2004, Residual strength of hybrid-fiber-reinforced high-strength concrete after exposure to high temperatures, *Cement and Concrete Research*, vol.34(6): 1065–1069. http://dx.doi.org/10.1016/j.cemconres.2003.11.010
136. Xiao J and König G, 2004, Study on concrete at high temperature in China—an overview, *Fire Safety Journal*, vol.39(1): 89–103. http://dx.doi.org/10.1016/S0379-7112(03)00093-6
137. Poon C S, Shui Z H and Lam L, 2004, Compressive behavior of fiber reinforced high-performance concrete subjected to elevated temperatures, *Cement and Concrete Research*, vol.34(12): 2215–2222. http://dx.doi.org/10.1016/j.cemconres.2004.02.011
138. Hou G, Ji Z, Wang J, , *et al*., 2008, Domestic and abroad

research status of humidity-control materials. Materials Review 22(8):78-81 (in Chinese)

139. Zhang H and Yoshino H, 2010, Analysis of indoor humidity environment in Chinese residential buildings, *Building and Environment*, vol.45(10): 2132–2140. http://dx.doi.org/10.1016/j.buildenv.2010.03.011
140. Jensen O M and Hansen P F, 1999, Influence of temperature on autogenous deformation and relative humidity change in hardening cement paste, *Cement and Concrete Research*, vol.29(4): 567–575. http://dx.doi.org/10.1016/S0008-8846(99)00021-6
141. Nehdi M and Hayek M, 2005, Behavior of blended cement mortars exposed to sulfate solutions cycling in relative humidity, *Cement and Concrete Research*, vol. 35(4): 731–742. http://dx.doi.org/10.1016/j.cemconres.2004.05.032.
142. Vu D, Wang K, Bac B H, *et al*., 2013, Humidity control materials prepared from diatomite and volcanic ash, *Construction and Building Materials*, vol.38: 1066– 1072. http://dx.doi.org/10.1016/j.conbuildmat.2012.09.040
143. Arundel A V, Sterling E M, Biggin J H, *et al*., 1986, Indirect health effects of relative humidity in indoor environments, *Environmental Health Perspectives*, vol.65: 351.https://doi.org/10.1289/ehp.8665351
144. Horikawa T, Kitakaze Y, Sekida T, *et al*., 2010, Characteristics and humidity control capacity of activated carbon from bamboo, *Bioresource Technology*, vol.101(11): 3964–3969. http://dx.doi.org/10.1016/j.biortech.2010.01.032
145. Wang J and Wang Z, 2007, Advances in humidity-controlling composite materials, *Materials Review*, vol.6: 13 (in Chinese)
146. Goto K and Terao S, 2005, Structures and humidity controlling performances of zeolite-cement hardened body, *Journal of the Ceramic Society of Japan*, vol.113 (1323): 739–742.https://doi.org/10.2109/jcersj.113.736
147. Deng L, Zheng B, and Fu L. 2007, Studies on the self-humidity controlling characteristic of cement-based composite material modified by attapulgite, *Non-Metallic Mines*, vol.4: 10.
148. Li Z, Wei F and Liu W, 2011, Manufacture on building blocks of humidity-controlling composite materials used in greenhouse, In Materials for Renewable Energy & Environment (ICMREE), 2011 International Conference on IEEE, 1125–1128.
149. Kuznik F, Virgone J and Noel J, 2008, Optimization of a phase change material wallboard for building use, *Applied Thermal Engineering*, vol.28(11–12): 1291–1298. http://dx.doi.org/10.1016/j.applthermaleng.2007.10.012
150. Regin A F, Solanki S C and Saini J S, 2008, Heat transfer characteristics of thermal energy storage system using PCM capsules: A review, *Renewable and Sustainable Energy Reviews*, vol.12(9): 2438–2458. http://dx.doi.org/10.1016/j.rser.2007.06.009
151. Khudhair A M and Farid M M, 2004, A review on energy conservation in building applications with thermal storage by latent heat using phase change materials, *Energy Conversion and Management*, vol.45(2): 263–275.http://dx.doi.org/10.1016/S0196-8904(03)00131-6
152. Pérez-Lombard L, Ortiz J and Pout C, 2008, A review on buildings energy consumption information, *Energy and Buildings*, vol.40(3): 394–398. http://dx.doi.org/10.1016/j.enbuild.2007.03.007
153. Lane G A, 1983, Solar heat storage: Latent heat materials. CRC Press.
154. Hirayama Y, Jolly S and Batty W J, 1997, Investigation of thermal energy storage within building thermal mass in northern Japan through dynamic building and building services simulation, In Proceedings of Seventh International Conference on Thermal Energy Storage, Sapporo, Japan, 355–360.
155. Hunger M, Entrop A G, Mandilaras I, *et al*., 2009, The behavior of self-compacting concrete containing micro-encapsulated phase change materials, *Cement and Concrete Composites*, vol.31(10): 731–743. http://dx.doi.org/10.1016/j.cemconcomp.2009.08.002
156. Farid M and Kong W J, 2001, Underfloor heating with latent heat storage. Proceedings of the Institution of Mechanical Engineers, Part A: Journal of Power and Energy 215: 601–609.
157. Castellón C, Medrano M, Roca J, *et al*., 2007, Use of microencapsulated phase change materials in building applications, ASHRAE, Project ENE2005-08256-C02-01/ALT.
158. Zach J, Sedlmajer M, Hroudova J, *et al*., 2013, Technology of Concrete with Low Generation of Hydration Heat, *Procedia Engineering*, vol.65: 296–301. http://dx.doi.org/10.1016/j.proeng.2013.09.046
159. Chu I, Lee Y, Amin M N, *et al*., 2013, Application of a thermal stress device for the prediction of stresses due to hydration heat in mass concrete structure, *Construction and Building Materials*, vol.45: 192–198. http://dx.doi.org/10.1016/j.conbuildmat.2013.03.056
160. De Rojas M S, Luxán M P D, Frías M, *et al*., 1993, The influence of different additions on portland cement hydration heat, *Cement and Concrete Research*, vol.23(1): 46–54.http://dx.doi.org/10.1016/0008-8846(93)90134-U
161. Kim J K, Kim K H and Yang J K, 2001, Thermal analysis of hydration heat in concrete structures with pipe-cooling system, *Computers and Structures*, vol.79(2): 163–171. http://dx.doi.org/10.1016/S0045-7949(00)00128-0
162. Bullard J W, Jennings H M, Livingston R A, *et al*., 2011, Mechanisms of cement hydration, *Cement and Concrete*

Research, vol.41(12): 1208–1223. http://dx.doi.org/10.1016/j.cemconres.2010.09.011

163. Pane I and Hansen W, 2005, Investigation of blended cement hydration by isothermal calorimetry and thermal analysis, *Cement and Concrete Research*, vol.35(6): 1155–1164. http://dx.doi.org/10.1016/j.cemconres.2004.10.027
164. Yang H, Tan L L and Dong W J, 2001, Influence of fly ash and superplasticizer on the heat of hydraion in cement, *Concrete*, vol.12: 9–12 (in Chinese)
165. Nocuń-Wczelik W and Czapik P, 2013, Use of calorimetry and other methods in the studies of water reducers and set retarders interaction with hydrating cement paste, *Construction and Building Materials*, vol.38: 980–986. http://dx.doi.org/10.1016/j.conbuildmat.2012.09.048
166. Pang X, Boontheung P and Boul PJ, 2014, Dynamic retarder exchange as a trigger for Portland cement hydration, *Cement and Concrete Research*, vol.63: 20–28. http://dx.doi.org/10.1016/j.cemconres.2014.04.007
167. Plank J, Sakai E, Miao C W, *et al*., 2015, Chemical admixtures—Chemistry, applications and their impact on concrete microstructure and durability, *Cement and Concrete Research*, vol.78(A): 81–99. http://dx.doi.org/10.1016/j.cemconres.2015.05.016
168. Xing J J and Guan X J, 2006, Study on the control over the cement hydration heat of the phase change materials, *Research & Application of Building Materials*, vol.6: 4–6 (in Chinese).
169. Rahhal V and Talero R, 2005, Early hydration of Portland cement with crystalline mineral additions, *Cement and Concrete Research*, vol.35(7): 1285–1291. http://dx.doi.org/10.1016/j.cemconres.2004.12.001
170. Orak S, 2000, Investigation of vibration damping on polymer concrete with polyester resin, *Cement and Concrete Research*, vol.30(2): 171–174. http://dx.doi.org/10.1016/S0008-8846(99)00225-2
171. Ou J, Liu T and Li J, 2008, Dynamic and seismic property experiments of high damping concrete and its frame models, *Journal of Wuhan University of Technology-Mater. Sci. Ed*., vol.23: 1–6.
172. Wong W G, Fang P and Pan J K, 2003, Polymer effects on the vibration damping behavior of cement, *Journal of Materials in Civil Engineering*, vol.15(6): 554–556. https://doi.org/10.1061/(ASCE)0899-1561(2003)15:6(554)
173. Fu X and Chung D D L, 1996, Vibration damping admixtures for cement, *Cement and Concrete Research*, vol.26(1): 69–75. http://dx.doi.org/10.1016/0008-8846(95)00177-8
174. Wen S and Chung D, 2000, Enhancing the vibration reduction ability of concrete by using steel reinforcement and steel surface treatments, *Cement and Concrete Research*, vol.30(2): 327–330. http://dx.doi.org/10.1016/S0008-8846(99)00238-0
175. Luo J, Duan Z, Xian G, *et al*., 2015, Damping performances of carbon nanotube reinforced cement composite, *Mechanics of Advanced Materials and Structures*, vol.22(3): 224–232. https://doi.org/10.1080/15376494.2012.736052
176. Koratkar N, Wei B Q and Ajayan P M, 2002, Carbon nanotube films for damping applications, *Advanced Materials*, vol.14(13–14): 997–1000. https://doi.org/10.1002/1521-4095(20020705)14:13/14%3C997::AID-ADMA997%3E3.0.CO;2-Y
177. Cui X, Sun S, Han B, , *et al*., 2017 Mechanical, thermal and electromagenetic properties of nano graphite platelets modified cementitious composites. *Composites Part A: Applied Science and Manufacturing*, 93:49-58. http://dx.doi.org/10.1016/j.compositesa.2016.11.017
178. Xu D, Cheng X, Guo X, *et al*., 2015, Design, fabrication and property investigation of cement/polymer based 1–3 connectivity piezo-damping composites, *Construction and Building Materials*, vol.84(1): 219–223. http://dx.doi.org/10.1016/j.conbuildmat.2015.03.043
179. Xie P and Beaudoin J J, 1995, Electrically conductive concrete and its application in deicing, *ACI Special Publication*, vol.154: 399–418.
180. Yehia S, Tuan C Y, 1999, Conductive concrete overlay for bridge deck deicing, *ACI Materials Journal*, vol.96(3): 382–391.
181. Yehia S, Tuan C Y, Ferdon D, *et al*., 2000, Conductive concrete overlay for bridge deck deicing: mixture proportioning, optimization, and properties, *ACI Materials Journal*, vol.97: 172–181.
182. Hou Z, Li Z and Tang Z, 2003, Finite element analysis and design of electrically conductive concrete for roadway deicing or snow-melting system, *ACI Materials Journal*, vol.100: 469–476.
183. Tuan C Y, 2004, Electrical resistance heating of conductive concrete containing steel fibers and shavings, *ACI Materials Journal*, vol.101: 65–71.
184. Tuan C Y and Yehia S, 2004, Evaluation of electrically conductive concrete containing carbon products for deicing, *ACI Materials Journal*, vol.101: 287–293.
185. Baldwin K, 1998, Electrically conductive concrete: properties and potential. *Construction Canada*, 98: 28– 29.
186. Zhang K, Han B and Yu X, 2011, Nickel particle based electrical resistance heating cementitious composites, *Cold Regions Science and Technology*, vol.69(1): 64–69. http://dx.doi.org/10.1016/j.coldregions.2011.07.002
187. Wu J, Liu J and Yang F, 2015, Three-phase composite conductive concrete for pavement deicing, *Construction and Building Materials*, vol.75: 129–135.

http://dx.doi.org/10.1016/j.conbuildmat.2014.11.004

188. Chung D D L, 2004, Self-heating structural materials, *Smart Materials and Structures*, vol.13(3): 562. https://doi.org/10.1088/0964-1726/13/3/015
189. Chen P and Chung D D L, 1995, Improving the electrical conductivity of composites comprised of short conducting fibers in a nonconducting matrix: The addition of a nonconducting particulate filler, *Journal of Electronic Materials*, vol.24(1): 47–51. https://doi.org/10.1007/BF02659726
190. Zhou X, Yang Z J, Chang C, *et al*., 2011, Numerical assessment of electric roadway deicing system utilizing emerging carbon nanofiber paper, *Journal of Cold Regions Engineering*, vol.26(1): 1–15. https://doi.org/10.1061/(ASCE)CR.1943-5495.0000033
191. Xie P, Gu P and Beaudion J J, 1996, Electrical percolation phenomena in cement composites containing conductive fibers, *Journal of Materials Science*, vol.31(15): 4093–4097. https://doi.org/10.1007/BF00352673
192. Gomis J, Galao O, Gomis V, *et al*., 2015, Self-heating and deicing conductive cement. Experimental study and modeling, *Construction and Building Materials*, vol.75: 442–449. http://dx.doi.org/10.1016/j.conbuildmat.2014.11.042
193. Sun M, Mu X, Wang X, *et al*., 2008, Experimental studies on the indoor electrical floor heating system with carbon black mortar slabs, *Energy and Buildings*, vol.40(6): 1094–1100. http://dx.doi.org/10.1016/j.enbuild.2007.10.009
194. Li S and Ye X, 2009, Study on the bridge surface deicing system in Yuebei section of Jingzhu highway, *International Journal of Business and Management*, vol. 3(12): 116.http://dx.doi.org/10.5539/ijbm.v3n12p116
195. Yehia S, Tuan C Y, Ferdon D, *et al*., 2000, Conductive concrete overlay for bridge deck deicing: mixture proportioning, optimization, and properties, *ACI Materials Journal*, vol.97: 172–181.
196. Pedeferri P, 1996, Cathodic protection and cathodic prevention, *Construction and Building Materials*, vol.10(5): 391–402. http://dx.doi.org/10.1016/0950-0618(95)00017-8
197. Stratfull R F, 1974, Experimental cathodic protection of a bridge deck, *Transportation Research Record*, vol.500: 1–15
198. Cañón A, Garcés P, Climent M A, *et al*., 2013, Feasibility of electrochemical chloride extraction from structural reinforced concrete using a sprayed conductive graphite powder-concrete paste as anode, *Corrosion Science*, vol.77: 128–134. http://dx.doi.org/10.1016/j.corsci.2013.07.035
199. Yehia S and Host J, 2010, Conductive Concrete for Cathodic Protection of Bridge Decks, *ACI Materials Journal*, vol.107.
200. Sobolev K G and Batrakov V G, 2007, Effect of a polyethylhydrosiloxane admixture on the durability of concrete with supplementary cementitious materials, *Journal of Materials in Civil Engineering*, vol.19(10): 809–819. https://doi.org/10.1061/(ASCE)0899-1561(2007)19:10(809)
201. Koch K, Bhushan B and Barthlott W, 2008, Diversity of structure, morphology and wetting of plant surfaces, *Soft Matter*, vol.4: 1943–1963. https://doi.org/10.1039/b804854a
202. Liu Y, Chen X and Xin J H, 2006, Super-hydrophobic surfaces from a simple coating method: a bionic nanoengineering approach, *Nanotechnology*, vol.17(13): 3259. https://doi.org/10.1088/0957-4484/17/13/030
203. Ganesh V A, Raut H K, Nair A S, *et al*., 2011, A review on self-cleaning coatings, *Journal of Materials Chemistry*, vol.21: 16304–16322. https://doi.org/10.1039/c1jm12523k
204. Popovics S, 1982, Fundamentals of Portland Cement Concrete—a Quantitative Approach: Fresh concrete: John Wiley & Sons 10: 332.
205. Hekal E E, Abd-El-Khalek M, El-Shafey G M, *et al*., 1999, Mechanical and physico-chemical properties of hardened Portland cement pastes containing hydrophobic admixtures. Part 1: Compressive strength and hydration kinetics, *ZKG International*, vol.52: 697–700.
206. Fratesi R, Moriconi G, Tittarelli R, *et al*., 1997, The influence of hydrophobized concrete on the corrosion of rebars, *ACI Special Publication*, vol.173: 105–122.
207. Tittarelli F, Moriconi G and Fratesi R, 2000, Influence of silane-based hydrophobic admixture on oxygen diffusion through concrete cement matrix, *ACI Special Publication*, vol.195: 431–446.
208. Batrakov V G, 1998, Modified concrete–Theory and practice, *Tekhnoproekt*, Moscow.
209. Ramachandran R, Sobolev K and Nosonovsky M, 2015, Dynamics of droplet impact on hydrophobic/icephobic concrete with potential for superhydrophobicity. Langmuir, 31(4):1437-1444. http://pubs.acs.org/doi/abs/10.1021/la504626f
210. J. de Vries I and Polder R B, 1997, Hydrophobic treatment of concrete. Construction and Building Materials, 11(4): 259-265.
211. Ding X, Zhou S, Gu G, *et al*., 2011, A facile and large-area fabrication method of superhydrophobic self-cleaning fluorinated polysiloxane/TiO2 nanocomposite coatings with long-term durability, *Journal of Materials Chemistry*, vol.21: 6161–6164. https://doi.org/10.1039/c0jm04546b
212. Mills A and Le Hunte S, 1997, An overview of semi-

conductor photocatalysis, *Journal of Photochemistry and Photobiology A: Chemistry*, vol.108(1): 1–35. http://dx.doi.org/10.1016/S1010-6030(97)00118-4

213. Oh W S, Xu C, Kim D Y, *et al*., 1997, Preparation and characterization of epitaxial titanium oxide films on Mo(100), *Journal of Vacuum Science and Technology-Section A-Vacuum Surfaces and Films*, vol.15: 1710–1716. https://doi.org/10.1116/1.580925
214. Fujishima A, Hashimoto K and Watanabe T, 1999, TiO_2 photocatalysis: fundamentals and applications: BKC Incorporated.
215. Tung W S and Daoud W A, 2011, Self-cleaning fibers via nanotechnology: A virtual reality, *Journal of Materials Chemistry*, vol.21: 7858–7869. https://doi.org/10.1039/c0jm03856c
216. Wang R, Hashimoto K, Fujishima A, *et al*., 1997, Light-induced amphiphilic surfaces, *Nature*, vol.388: 431–432. https://doi.org/10.1038/41233
217. Hashimoto K, Irie H and Fujishima A, 2005, TiO_2 photocatalysis: A historical overview and future prospects, *Japanese Journal of Applied Physics*, vol.44(1): 8269. https://doi.org/10.1143/JJAP.44.8269
218. Sakai N, Fujishima A, Watanabe T, *et al*., 2003, Quantitative evaluation of the photoinduced hydrophilic conversion properties of TiO_2 thin film surfaces by the reciprocal of contact angle, *The Journal of Physical Chemistry B*, vol.107(4): 1028–1035. https://doi.org/10.1021/jp022105p
219. Cassar L, 2004, Photocatalysis of cementitious materials: clean buildings and clean air, *MRS Bulletin*, vol.29(5): 328–331.https://doi.org/10.1557/mrs2004.99
220. Chen J and Poon C, 2009, Photocatalytic construction and building materials: From fundamentals to applications, *Building and Environment*, vol.44(9): 1899–1906. http://dx.doi.org/10.1016/j.buildenv.2009.01.002
221. Guerrini G L, Plassais A, Pepe C, *et al*., 2015, Use of photocatalytic cementitious materials for self-cleaning applications, *Newsletter*: 219–226.
222. Poon C S and Cheung E, 2007, NO removal efficiency of photocatalytic paving blocks prepared with recycled materials, *Construction and Building Materials*, vol. 21(8): 1746–1753. https://doi.org/10.1016/j.conbuildmat.2006.05.018
223. Dylla H, Hassan M M, Schmitt M, *et al*., 2010, Laboratory investigation of the effect of mixed nitrogen dioxide and nitrogen oxide gases on titanium dioxide photocatalytic efficiency in concrete pavements, *Journal of Materials in Civil Engineering*, vol.23(7): 1087–1093. https://doi.org/10.1061/(ASCE)MT.1943-5533.0000248
224. Guerrini G L and Peccati E, 2015, Photocatalytic cementitious roads for depollution, *Newsletter*: 179–186.
225. Maggos T, Plassais A, Bartzis J G, *et al*., 2008, Photocatalytic degradation of NO_X in a pilot street canyon configuration using TiO_2-mortar panels, *Environmental Monitoring and Assessment*, vol.136(1): 35–44. https://doi.org/10.1007/s10661-007-9722-2
226. Lackhoff M, Prieto X, Nestle N, *et al*., 2003, Photocatalytic activity of semiconductor-modified cement-influence of semiconductor type and cement ageing, *Applied Catalysis B: Environmental*, vol.43(3): 205–216. http://dx.doi.org/10.1016/S0926-3373(02)00303-X
227. Auvinen J and Wirtanen L, 2008, The influence of photocatalytic interior paints on indoor air quality, *Atmospheric Environment*, vol.42(18): 4101–4112. http://dx.doi.org/10.1016/j.atmosenv.2008.01.031
228. Buswell R A, Soar R C, Gibb A G, *et al*., 2007, Freeform construction: mega-scale rapid manufacturing for construction, *Automation in Construction*, vol.16(2): 224–231.http://dx.doi.org/10.1016/j.autcon.2006.05.002
229. Buswell R A, Thorpe A, Soar R C, *et al*., 2008, Design, data and process issues for mega-scale rapid manufacturing machines used for construction, *Automation in Construction*, vol.17(8): 923–929. http://dx.doi.org/10.1016/j.autcon.2008.03.001
230. Le T T, Austin S A, Lim S, *et al*., 2012, Mix design and fresh properties for high-performance printing concrete, *Materials and Structures*, vol.45(8): 1221–1232. https://doi.org/10.1617/s11527-012-9828-z
231. Perrot A, Rangeard D and Pierre A, 2015, Structural built-up of cement-based materials used for 3D-printing extrusion techniques, *Materials and Structures*: 1–8.
232. Le T T, Austin S A, Lim S, *et al*., 2012, Hardened properties of high-performance printing concrete, *Cement and Concrete Research*, vol.42(3): 558–566. http://dx.doi.org/10.1016/j.cemconres.2011.12.003
233. Feng P, Meng X, Chen J, *et al*., 2015, Mechanical properties of structures 3D printed with cementitious powders, *Construction and Building Materials*, vol.93: 486–497.http://dx.doi.org/10.1016/j.conbuildmat.2015.05.132
234. Gibbons G J, Williams R, Purnell P, *et al*., 2010, 3D Printing of cement composites, *Advances in Applied Ceramics*, vol.109(5): 287–290. https://doi.org/10./174367509X12472364600878
235. Lim S, Buswell R A, Le T T, *et al*., 2012, Developments in construction-scale additive manufacturing processes, *Automation in Construction*, vol.21: 262–268. http://dx.doi.org/10.1016/j.autcon.2011.06.010
236. Charron K, 2015, WinSun China builds world's first 3D printed villa and tallest 3D printed apartment building, viewed January 18 2015, http://www.3ders.org/articles/20150118-winsun-builds-world-first-3d-printed-villa-and-tallest-3d-printed-buildi

ng-in-china.html/

237. Khoshnevis B, Thangavelu M, Yuan X, *et al.*, 2013, Advances in contour crafting technology for extraterrestrial settlement infrastructure buildup, *AIAA*, vol.5438: 10–12. http://dx.doi.org/10.2514/6.2013-5438
238. Cesaretti G, Dini E, De Kestelier X, *et al.*, 2014, Building components for an outpost on the Lunar soil by means of a novel 3D printing technology, *Acta Astronautica*, vol.93: 430–450. http://dx.doi.org/10.1016/j.actaastro.2013.07.034
239. Neithalath N, Bentz D P and Sumanasooriya M S, 2010, Advances in pore structure characterization and performance prediction of pervious concretes, *Concrete International*, vol.32: 35–40.
240. Ghafoori N and Dutta S, 1995, Laboratory investigation of compacted no-fines concrete for paving materials, *Journal of Materials in Civil Engineering*, vol.7(3): 183–191. https://doi.org/10.1061/(ASCE)0899-1561(1995)7:3(183)
241. Zheng M, Chen S and Wang B, 2012, Mix design method for permeable base of porous concrete, *International Journal of Pavement Research and Technology*, vol.5: 102–107.
242. Nguyen D H, Sebaibi N, Boutouil M, *et al.*, 2014, A modified method for the design of pervious concrete mix, *Construction and Building Materials*, vol.73: 271–282. http://dx.doi.org/10.1016/j.conbuildmat.2014.09.088
243. ACI committee 522, 2006, Pervious concrete, Report No. 522R-10, American Concrete Institute (ACI), Detroit, USA.
244. Schaefer V R, Wang K and Suleiman M T, 2006, Mix Design Development for Pervious Concrete in Cold Weather Climates, Technical report, National Concrete Pavement Technology Center, Iowa State University, USA.
245. Weller C, 2015, This 'thirsty' concrete absorbs 880 gallons of water a minute-here's how it works, viewed September 28 2015, http://www.techinsider.io/how-magical-concrete-absorbs-water-2015-9/.
246. Malhotra V M, 1976, No-fines concrete-its properties and applications, In Journal Proceedings, 628–644.
247. Ghafoori N and Dutta S, 1995, Development of no-fines concrete pavement applications, *Journal of Transportation Engineering*, vol.121(3): 283–288. https://doi.org/10.1061/(ASCE)0733-947X(1995)121:3(283)
248. Scholz M and Grabowiecki P, 2007, Review of permeable pavement systems, *Building and Environment*, vol.42(11): 3830–3836. http://dx.doi.org/10.1016/j.buildenv.2006.11.016
249. Yang J and Jiang G, 2003, Experimental study on properties of pervious concrete pavement materials, *Cement and Concrete Research*, vol.33(3): 381–386. http://dx.doi.org/10.1016/S0008-8846(02)00966-3
250. Kevern J T, 2008, Advancement of pervious concrete durability. Ames, IA, USA: Iowa State University.
251. Energy Matters, 2016, Solar Powered, Light Emitting Cement, viewed May 11, 2016, http://www.energymatters.com.au/renewable-news/solar-light-cement-em5466/
252. News Nation, 2016, Scientists develop solar-powered light-emitting cement with a life of 100 years, viewed May 11, 2016, http://www.newsnation.in/article/130313-scientists-create-light-emitting-cement-that-has-a-life-of-100-years.html/.

RESEARCH ARTICLE

Framing a satellite based asset tracking (SPARTACUS) within smart city technology

Fabio Casciati[1], Sara Casciati[2], Clemente Fuggini[3], Lucia Faravelli[1], Ivan Tesfai[3] and Michele Vece[1*]

[1] DICAr, University of Pavia, Via Ferrata 3, Pavia 27100, Italy
[2] DICAr, School of Architecture, University of Catania at Siracusa, P.za Federico di Svevia, Siracusa 96100, Italy
[3] D'Appolonia S.p.A., Piazza Duca D'Aosta 14, Milano 20124, Italy

Abstract: "Smart city" is a term currently used to denote cities moved by the opportunity to enhance the quality of life and the security of their citizens. Attention is here focused on the concept that the development of smart cities can also be achieved by improving the efficiency of civil infrastructures through a real-time monitoring. This is the specific target of the European Union FP7 project (SPARTACUS), moved from the parallel chance to develop industry pull applications for the European EGNOS and GALILEO satellite systems. In this paper, laboratory tests are carried out to provide specific devices the ability to run while satisfying the requirements of the incoming GALILEO system. Moreover, some of the targets are achieved within the current GPS system. An extensive experimental campaign is offered to validate the units in such a scenario.

Keywords: smart cities, asset tracking, security, positioning, data transmission, GNSS

*Correspondence to: Michele Vece, DICAr, University of Pavia, Via Ferrata 3, Pavia 27100, Italy; Email: miche.vece@gmail.com

Received: October 30, 2016; **Accepted:** November 17, 2016; **Published Online:** December 30, 2016
Citation: Casciati F, Casciati S, Fuggini C, *et al.*, 2016, Framing a satellite based asset tracking (SPARTACUS) within smart city technology. *Journal of Smart Cities*, vol.2(2): 40–48. http://dx.doi.org/10.26789/JSC.2016.02.003.

1. Introduction

"Smart city" is a term recently introduced to denote a city that uses Information and Communication Technologies (ICTs) in order to enhance the quality of life of the citizens and to contribute to its sustainable development. Smart city initiatives attracted the attention of many researchers and politicians on issues such as mobility, security, environment, or any combination of them, since they are driven by the goal of serving citizens in a better way[1]. Moreover, smart cities facilitate the government to monitor, understand, analyze, and plan the city in order to improve the equity, efficiency, and quality of life[2,3].

The attention of the research activity summarized in this paper is focused on the concept that the smart city development provides opportunities to enhance the quality of civil infrastructures as well. Indeed, smart cities lead to a significant evolution of roads, bridges, tunnels, and rail through a real-time monitoring for maximizing the services security of the residents while optimizing the use of resources.

Within this framework, special care is paid to the European Union FP7 project named SPARTACUS (Satellite Based Asset Tracking for Supporting Emergency Management in Crisis Operations), currently in progress[4]. It is moved from the parallel opportunity to develop industry pull applications and solutions for the European EGNOS and GALILEO satellite systems. Within the project, satellite-based positioning units, also mounting Inertial Navigation Systems (INS),

are tested in order to track critical transport assets, relief goods distribution, and first responders in disaster management operations[5]. The idea is not new, but its extensive use in full-scale tests makes the dissemination of interest.

One of the main challenges is related to the security issues. Indeed, smart cities require access to cost effective, high performance security services, and sophisticated control systems, which ensure the higher network reliability. Therefore, it is important to instil awareness that digital infrastructures may be subjected to information thefts and thus results in an increase in cyber-crimes. Potential can be undermined in case of unauthorized electronic access, and technological issues can arise from hardware/software incompatibility because everything in smart cities has to be automated and any fragmentation may lead to serious failures and accidents.

This paper starts from the current state of the art in order to understand the need of the proposed system. After an overview of the adopted system architecture, the integration of some devices is discussed. A broad experimental campaign of field tests follows to validate the units in the presented scenario. Simulations of test results are also carried out in order to provide an already running system exploiting features of the incoming GALILEO.

2. Governing Relations

Before detailing the innovative aspects of the solution proposed within the abovementioned FP7 project (SPARTACUS), it is convenient to show the current drawbacks faced daily by rescue teams, which need to be informed in time when a catastrophic event occurs.

2.1 Transportation and Security

Throughout the world, the transport of goods is greatly increased in terms of volume and variety over the last decades. This growth is the main cause of some substantial costs such as cumulative congestion levels and associated environmental pollution, but especially in term of accidents risk and time wastage during traveling[6]. Traditional approaches failed to solve issues like these.

New ways are currently under investigation with the aims to develop an effective system able to increase network efficiency, without compromising safty, and to provide accurate and reliable data for maintenance and planning purposes in case of emergency.

A real case is used to highlight current operational challenges and technology gaps occurring in a disaster situation. It is used to emphasize how the SPARTACUS architecture has to operate.

Trains in Italy frequently use the rail system in the Piedmont region, where several areas are exposed to erosion. During the winter period, the situation is aggravated by severe weather. In late February 2016, it was reported that there was an alert status due to occasional storms, abundant rains, and flooding until, on February 28, a passenger train from Biella to Novara derailed after a landslide from the rock overlying the retaining wall that caused its collapse (Figure 1). Fortunately, the thirteen travelers on board were unharmed, but the effects were dramatic because the rail links were blocked over a large period of time due to the complexity of the rescue and restoration operations.

Figure 1. Disaster scenario of the railway system in Piedmont region.

The case illustrated above shows that, every time and anywhere, such events can happen and vehicles have to be equipped with a satellite-based tracking unit in order to know exactly where the train is located at the moment of a disaster. This bit of information is also a must to stop other trains traveling to the affected area. Indeed, the effects for the mentioned case become catastrophic if another train hits the one that is obliged to stop. A real-time positioning is also required for transport of critical goods. Moreover, since surveillance of data (temperature, humidity, etc.) within each wagon is also necessary during the travel, data on local conditions should also be collected.

2.2 Global Navigation Satellite Systems: A Brief Overview

Consolidated and available technologies for a precise

location are based on Global Navigation Satellite Systems (GNSS). The navigation systems provided by engineering advances in satellite technologies were initially the NAVSTAR GPS (Navigation System with Time and Ranging - Global Positioning System) developed and maintained by the U.S. Department of Defense and Transportation, and the Russian Global Navigation Satellite System GLONASS (Globaluaya Navigatsionnaya Sputnikovaya Sistema)[7]. Although both are national military systems, they were available for use by the international private and commercial communities[8,9].

Recently a Chinese system (BeiDou) was completed as well as two of them designed and implemented by India, the Indian Regional Navigational Satellite System (IRNSS) and Japan, the Quasi Zenith Satellite System (QZSS), respectively[10,11].

In Europe, concern was voiced about dependence on a foreign military system and thus plans for a civilian global navigation satellite system were put in place.

GPS employs two fundamental observables for positioning and navigation, the pseudo-ranges and the carrier-phase. The first one is a measure of the distance between the satellite at the time of transmission and the receiver when receives the signal. When used in instantaneous stand-alone mode, one obtains an accuracy of 10–20 m after the removal of selective availability. The second one can be used to determine ranges with millimetric accuracy, provided the integer ambiguity problem is solved[12-14].

The system was divided in an overlay for the existing systems (GNSS-1), and a completely autonomous one with a separate space segment (GNSS-2). Further, the drop of equipment prices over the past ten years led to an enormous growth in the number of GPS users and new applications emerged such as car navigation systems, fleet management, aircraft approach, bridge deformation monitoring, and the navigation of agricultural field machinery. These multiple applications increased the necessity to improve accuracy, availability, and integrity in the systems.

Currently, Differential GNSS (DGNSS) represents a solution for these user requirements, where correctional data are emitted from a reference system placed in a known position and sent to a receiver. In differential positioning, a minimum of two receivers, named Base Station and Rover, are involved. The Base Station occupies a known position during the session, and the determination of the Rover related to the base represents the target of the work. Both receivers observe the same constellation of satellites at the same time, and since the base position is known, corrections may be generated in order to improve the solution at the Rover, as shown in Figure 2.

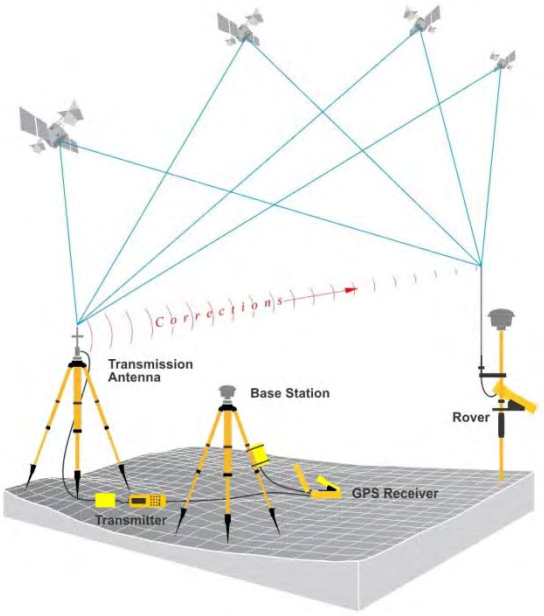

Figure 2. Differential GNSS with RTK Positioning.

The GPS signal is affected by a number of error sources including orbital and atmospheric propagation errors[15]. An improvement in the GPS performance can take the form of enhancements in the geometry of data sources (satellites), measurement quality, or both. It is wellknownthat GPS is also unable to measure low velocity, therefore, radar odometer or wheel sensors can be adopted in order to measure speed and improve the position accuracy in transport applications, as fully described in Section Four.

3. The European Challenge

The strategy for the European involvement in the next generation of Global Navigation Satellite Systems (GNSS-2) consists of an independent navigation space-segment and respective ground infrastructure under the designation of GALILEO[16–18]. The aim of this decision is to overcome the unacceptable dependency on third-party states, which is directly linked to the sovereignty issues emerging if Europe uses foreign-controlled navigation systems for critical security applications. Moreover, the possible introduction of user-fees for GPS infrastructure and services has to be considered as well as the drawback of having

no access to the technical development of the system, in order to ensure the participation of European industry in the fast-growing market of satellite navigation.

The first two satellites, which are part of the operational system, were launched in October 2011 and are denoted as ProtoFlight Model (PFM) and Flight Model 2 (FM2), reported as E11 and E12 in RINEX observation files. The second pair of IOV satellites (FM3 and FM4) was launched on October 2012, and started signal transmission in December of the same year. All IOV satellites are equipped with two Passive Hydrogen Masers (PHMs) and two Rubidium Atomic Frequency Standards (RAFSs) which are used as quality indicator for the orbits.

As of December 2015, GALILEO counts 12 satellites in orbit, but the implementation of the complete 30-satellite constellation (24 operational and 6 active spares) continues to be postponed so that the Full Operational Capability (FOC) is currently planned for year 2020.

3.1 Simulations of Realistic Scenarios

The delay of the European release, which is expected to have an open architecture, completely independent of the current navigation systems, forced the consortium involved in the research activity reported in this paper to use the GPS signals for testing the implemented prototype. Nevertheless, laboratory tests with the help of a multi-GNSS simulator provided by Spectracom Corp. (GSG-62) were also carried out at the University of Pavia in order to design, develop, and validate GALILEO-ready solutions, i.e., solutions with functionalities able to exploit the features of the innovative satellite system[19].

The opportunity to use systems that simulate satellite constellations arises from the need for all the providers of GNSS receivers to test their devices and ensuring or improving their capabilities in term of accuracy and reliability. A GSG-62 multi-channel simulator generates the same RF signals that are broadcast by either GALILEO or GPS navigation satellites. Indeed, it offers multiple simulation of constellation with a base of 32 channels, expandable up to 64, and allows the building of real time trajectories within the StudioView™ software environment. In this way, the GPS signals are used to check the position accuracy of the receiver chosen by the consortium for the SPARTACUS project (Ellipse-N)[20]. Simultaneously, the trajectory provided by the GALILEO satellites may be used to upgrade the system in the acquisition and transmission of the message from the data collector to a control center. After that, the path is compared with the GPS reference track within Google Earth through the NMEA standard format[21], as shown in Figure 3.

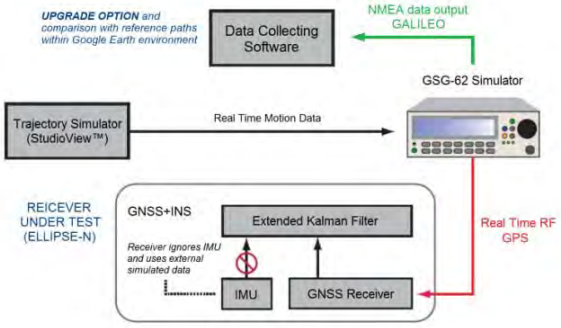

Figure 3. Scenario of a real time trajectory simulation for laboratory test.

The experimental results proposed in this section aim to estimate the value of the upgrade option of the software expected for the collection of positioning data with the upcoming European Satellite System (GALILEO) in the urban canyon of Pavia, Italy. For this reason, two different trajectories respectively with 4 and 8 satellites are carried out, both starting from the Department of Civil Engineering and Architecture (DICAr), up to the Campus Aquae, placed nearby (Via Cascinazza 15) and the Railway Station (located in Via Brichetti 40), respectively. The latitude and longitude can be extracted by NMEA strings and imported in Google Earth to provide a visual comparison of the performed track (Figure 4A). Azimuth and elevation are also handled in Matlab® software environment in order to offer a GALILEO satellites view (Figure 4B).

The described approach was essential first for the hardware integration required by the design of the proposed tracking system. Moreover, it made the software updating possible in two aspects: (i) the local storage of the needed positioning information, and (ii) its sending to the operative center using a low-power wireless communication. Once the GALILEO signal simulator has been set for the transfer of NMEA sentences, to configure the acquisition code for the oncoming European Satellite Navigation System was eventually done.

4. The SPARTACUS Solution

GALILEO intends to provide a more robust positioning capability enhancing the adoption of satellite

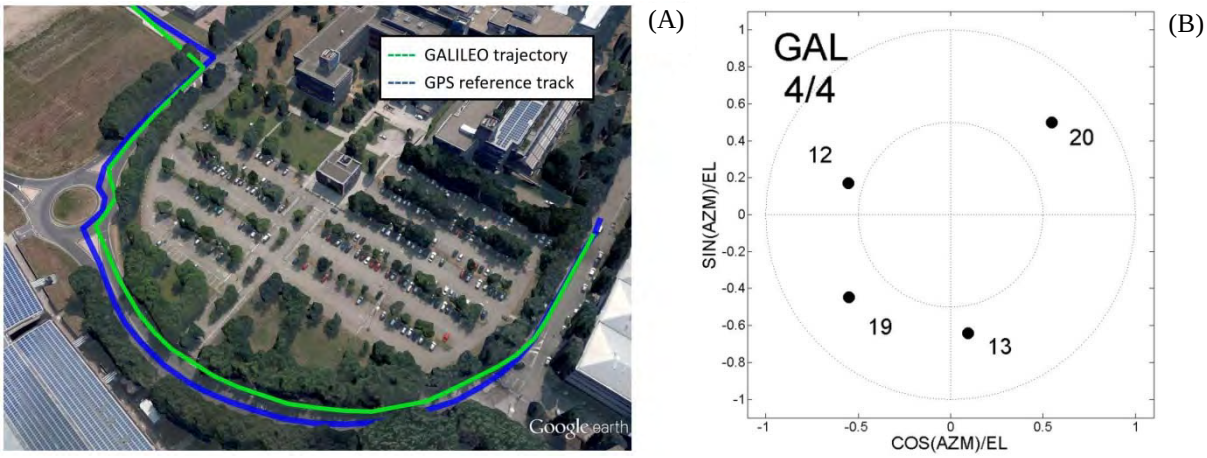

Figure 4. Trajectories comparison in Google Earth **(A)** and GALILEO satellites view **(B)**.

technologies for solutions that requires signal continuity and integrity. The impact is on various application areas, including emergency and disaster management, rescue tasks and location-based services supporting responders in critical operations. The ongoing SPARTACUS project started to develop new EU-specific services for the following three application areas: (i) critical transport assets in case of major failure of existing networks, (ii) flow of relief support goods from the sending side to the receiving place, and (iii) first responders ensuring their safety in crisis management operations.

These application areas are in line with the overall scope of the project, that is to design, realize, test and validate GALILEO-ready tracking/positioning solutions in simulated and real world for critical asset tracking and crisis management. The output is the definition of system architectures and components with features targeted to satisfy the needs of the users involved.

The solutions designed are based on providing precise localization of goods in harsh environment during absence of signal (canyons, tunnels etc.), guaranteeing effective local storage with a communication point from multiple tracking units to a remote site, and ensuring communication network over the failure of the existing terrestrial infrastructures in disaster situations.

The research activity carried out in this paper is focused on the positioning of all components concerning the freight transport, such as containers, wagons and locomotives (Figure 3). Particular attention is paid to the data transmission from each GNSS based tracking units to the collecting centre, since the conventional cabling method suffers problems due to inflexible installation and negative impact on the transportation vehicle.

As shown in Figure 5, the local wireless network for transport application consists of several GNSS sensors integrated with a ZigBee Node through RS232 serial port (*tracking units*), and each of them communicates with the *collecting unit* integrated with a ZigBee Base Station. The GNSS sensors acquire the wagons/container position from the GNSS satellites signal with a frequency of 1 Hz and send the position data to a centralized unit, which is located on board the locomotive through the multi-hop ZigBee mesh network. Finally, the collecting unit is linked to a remote centre through a satellite backhauling device (*communication unit*), avoiding the existing terrestrial communication infrastructure.

Figure 5. Case under study: transport application.

4.1 Features of a Single Board Tracking Unit

Reliability, accuracy, low cost and low power are the main qualities required by a positioning system for the infrastructure monitoring of a smart city. The selected devices for the development of a single board tracking unit consist of an inertial sensor with internal GNSS

receiver, a credit-card sized computer, and a GBAN ZigBee Wireless Data Transmission Device. The specific functions for each component of the tracking unit are listed in Table 1.

Table 1. Technical specifications and functions of the tracking unit

Hardware	Function
Ellipse-N	Exploit INS capabilities without navigation satellites signal
GNSS antenna	Acquire GNSS positioning data with quality field (accuracy/precision)
Raspberry Pi 2	Collect positioning information to allows local storage and post-processing
PiFace Shim RTC	Provide a continuous timing through an external local clock
External sensors	Supply information on temperature, humidity, and limit switch
GBAN ZigBee	Send information to the collecting unit using Wireless Transmission Devices

Therefore, in order to achieve data post-processing, the system has to be equipped with a data collector (Raspberry Pi) able to manage a local storage of the information to be transmitted to the remote control. Figure 6 shows all the hardware components for the final prototype used for the testing activity. The Raspberry Pi 2 is based on the Broadcom BCM2835 system on a chip (SoC). It is supplied with 512MB of RAM, four Universal Serial Bus (USB), and Micro Secure Digital (Micro SD) sockets for boot media and persistent storage. Figure 6 also shows the Ellipse N with its GNSS antenna provided by SBG Systems, which is a miniature sensor with high-performance Micro Electro-Mechanical Systems (MEMS). It also includes an Inertial Measurement Unit (IMU), an on-board enhanced Extended Kalman Filter (EKF),

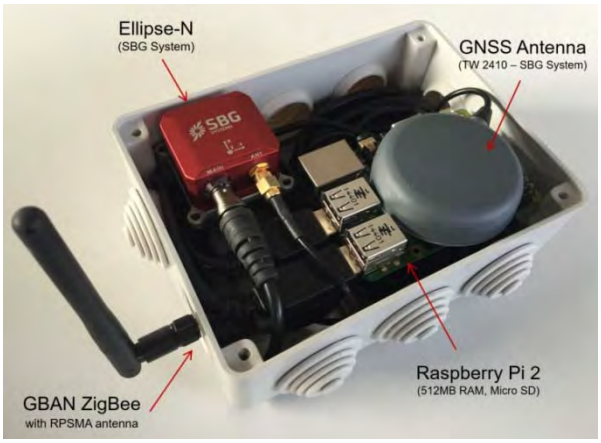

Figure 6. Hardware components of the positioning system.

and supports standard protocols such as the NMEA-0183 for direct integration into existing applications[22].

Once the positioning data are correctly stored inside the memory of the data collector, the information is sent by ZigBee devices to a collecting unit placed on board the locomotive in order to be transmitted via satellite to a remote centre for monitoring in real-time goods and vehicles. Among those available ZigBee technology offers a great trade-off in terms of power, range, data rate, and security. The ZigBee organizes multi-hop network and imposes that two devices exchange data depending on other intermediate forwarding devices. Further, the nature of this system requires that each device perform a specific networking function that determines its role within the network. The developed network consists of a Coordinator, Router and End device nodes, but the device type does not restrict the type of application that may run on the particular device because it is usually determined at compile-time[23].

4.2 System Performance in Harsh Environment

The SPARTACUS tracking system is designed to work anywhere in the same way, regardless of GNSS signal availability. Currently, Europe's Transport positioning applications are based on Radio-Frequency Identification (RFID) and European Rail Traffic Management System (ERTMS). For this kind of applications the absence of signal coverage cannot occur because the position is determined by a set of precise points located along train paths.

SPARTACUS proposes to determine the position independently from external infrastructures ensuring low cost and dead reckoning capabilities. Indeed, the adopted sensor integrates an Extended Kalman Filter (EKF) to estimate the real time position, velocity and orientation of the train. Figure 7 shows the acceleration response produced by the three-axial Crossbow CXL01F3[24] and the EKF integrated into the inertial navigation system.

When aiding data such as GPS positions are available, the EKF corrects the current state preventing drifts, but when the measurement is not received, the estimation error tends to increase.

In this case, the system only relies on the inertial sensor in order to continuously track position, velocity and orientation. Since cost constraints are strict within the project, MEMS technology represents the most suitable solution, but sometimes the position drift can

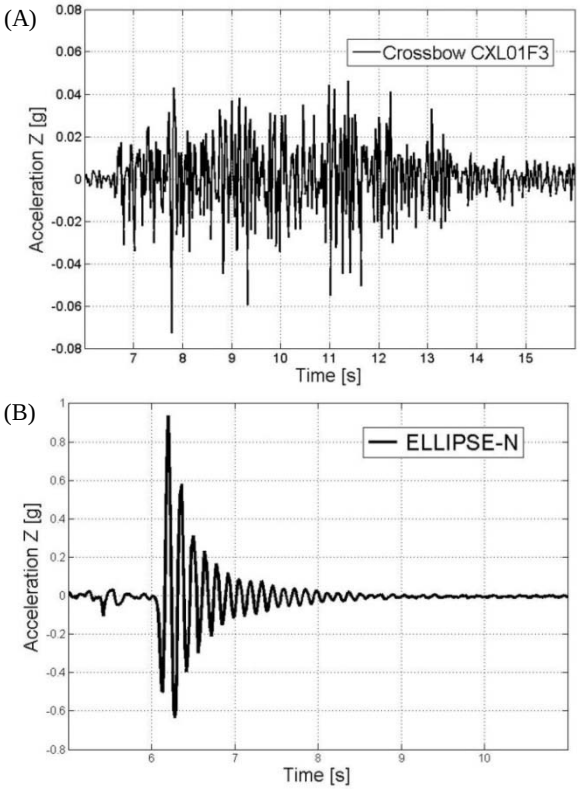

Figure 7. Crossbow accelerations **(A)** and EKF effect on the adopted sensor **(B)**.

reach meters after just few seconds of free inertial navigation. For this reason, additional information to maintain proper accuracy are needed, even during long term GNSS drop outs. An odometer (GSS25 provided by Pegasem Messtechnik GmbH) is adopted[25]. The GSS25 has to be placed on the wheel of the vehicle and can be used to measure its average velocity when GNSS are not available. The odometer aiding reduces the position drift. The sensor can be simply added at the head of the train. Possible performance differences are explained by avoiding a thermal calibration on wagons and containers in order to save production time and cost.

5. Experimental Data Set

The field tests reported in this section cover the area around the urban canyon of Pavia (Italy) in order to ensure anytime/anywhere the positioning accuracy of the adopted system. Because it is designed to transport applications, the navigation system has to satisfy requirements for the urban environment. The precision of the signal can be mined by the characteristics of the urban areas, where physical restrictions are imposed such as buildings, narrow streets, tunnels or bridges, and for this reason is necessary to validate also the system capabilities in dead reckoning mode[26].

The tracking unit is placed inside a car to reply the train motion profile and the entire system is supplied directly from the power supply of the vehicle. The paths with GNSS satellite signal coverage are repeated detaching the external GNSS antenna during the test. In this way, the satellite signal cannot be received by the sensor and the condition of a train inside a tunnel is obtained.

The two parameters used to measure the position accuracy of the system are the Average Positioning Error (μ) and its Standard Deviation (σ), expressed in Equation 1.

$$\mu = \sum_{i=1}^{N} \frac{x_i}{N} \qquad \sigma = \sqrt{\sum_{i=1}^{N} \frac{(x_i - \mu)^2}{N-1}} \tag{1}$$

where x_i is the i-th positioning error, and N is the total number of data. The robustness of the entire system has to be checked in case of disturbances or whatever changing of boundary conditions for very long period as well. Table 2 summarizes the results from the field test sessions carried out at several speeds in harsh environments.

Table 2. Experimental results obtained for the field test sessions

Set	μ(m)	σ(m)	v_m(m/s)	Positioning error after 60s (m)
T01	1.172	0.788	8.30	0.320
T02	2.924	2.505	9.70	4.019
T03	4.240	3.564	15.0	2.030
T04	8.406	5.675	15.8	2.560
T05	0.996	0.597	varying	0.219
T06	6.670	6.212	20.0	13.34
T07	1.710	0.939	21.2	3.554
T08	9.546	4.069	27.8	17.75
T09	7.271	5.498	30.5	11.53
T10	3.264	1.144	varying	5.259

The tests from T01 until to T05 are carried out in the urban environment, whilst those from T06 to T10 are addressed to the extra-urban one. The tracking system behavior is affected by the density of surrounding trees and buildings. The results in Table 2 are computed only on the time window when the GPS antenna is detached. The wished positioning error threshold is widely fulfilled in all of them, provided the GSS25 sensor is connected to the receiver. Collected data are also imported within Matlab® software

environment where, after one minute from the detachment moment, accuracy is investigated by means the positioning error (Figure 8).

The case studies reported in Figure 8 show the odometer impact when stops (3 in the tests) are included along the trajectory without GNSS satellite signal coverage.

At last, the data integrity of the data acquisition software was investigated in order to check the performance of the described system. The correctness of the message acquired by the tracking unit is achieved through the percentage of the uncorrupted NMEA sentences, and a detailed analysis demonstrated that they are totally stored into the memory of the data collector.

6. Conclusions

The first 24 hours of an incident are the most critical in view of saving human lives. This aspect is crucial in the urban design of a smart city.

Past experiences proved that the availability of real time information is necessary to promptly inform the rescue teams and to protect the people suffering the natural disaster. This research activity details the development of a portable and modular system to provide non-terrestrial based crisis management support. Improving efficiency and saving costs are the two main issues. One of the most important services that can be offered to the citizen of a smart city is the capability of an independent network with satellite backhaul, which is always able to connect, even independently of availability of local infrastructure, providing access to large user groups (i.e. rescue teams as well as victims). The result of a broad experimental campaign is here reported to validate the inertial platform of the system in order to provide dead zone reckoning. Indeed, GNSS dead zones such as valleys, tunnels, and building interiors have to be overcome for critical assets and crises. Moreover, the involved technology envisages future use of the GALILEO signal, exploiting the important benefit of the integrity information which is of highest importance in the Public Protection and Disaster Relief (PPDR) scenarios. It goes much beyond the possibilities of current GPS offer.

Conflict of Interest and Funding

No conflict of interest was reported by the authors. The research leading to these results has received

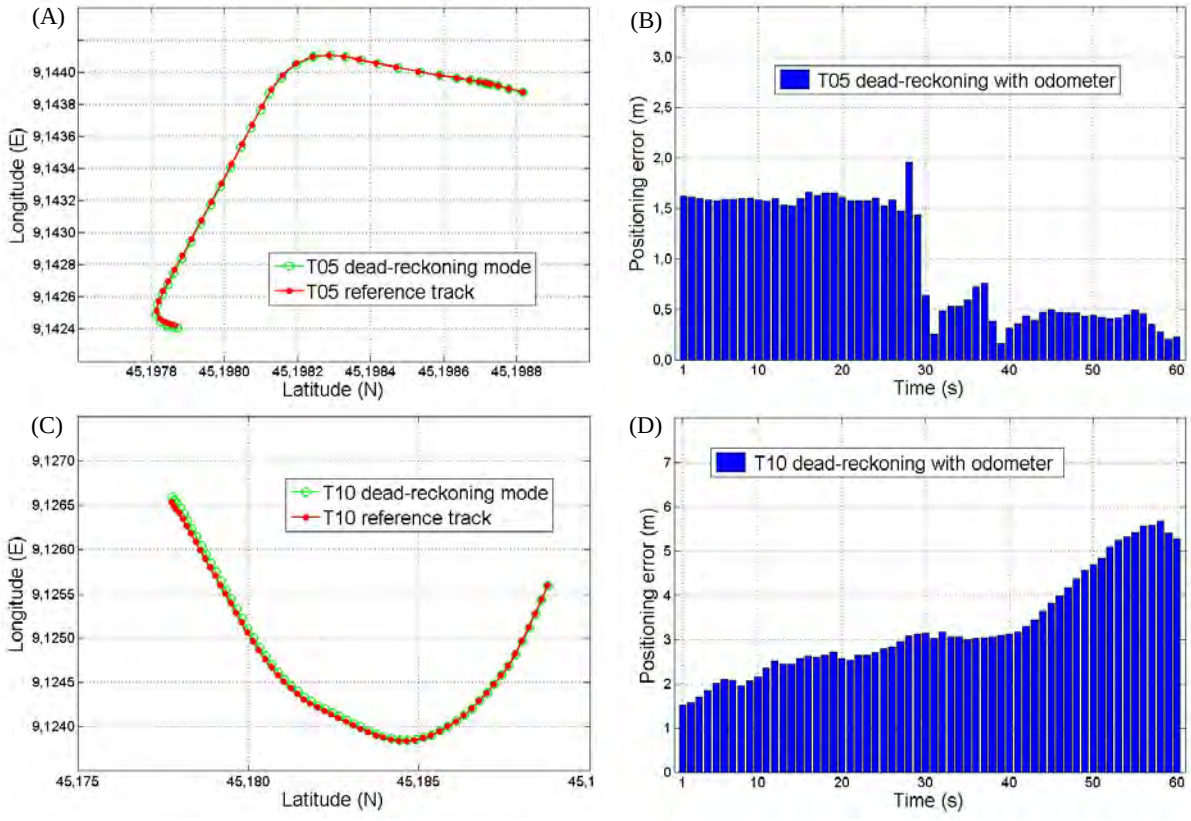

Figure 8. Case studies **(A–C)** and positioning error **(B–D)**.

funding from the European Union Seventh Framework Programme (FP7/2007-2013) under grant agreement n° [313002].

References

1. Casciati F, Casciati S, Faravelli L, *et al.* 2015, Development of an Outline Detection Tool in QGIS environment for risk mitigation applications, *Journal of Smart Cities*, vol.1(1): 59–67.
2. D'Alessandro A, Ubertini F, Laflamme S, *et al.* 2015, Towards smart concrete for smart cities: Recent results and future application of strain-sensing nanocomposites, *Journal of Smart Cities*, vol.1(1): 3–14. https://doi.org/10.18063/JSC.2015.01.002.
3. Komninos N, Bratsas C, Kakderi C, *et al.* 2015, Smart City Ontologies: Improving the effectiveness of smart city applications, *Journal of Smart Cities*, vol.1(1): 31–46. https://doi.org/10.18063/JSC.2015.01.001.
4. Spartacus Project, 2016, *Satellite Based Asset Tracking for Supporting Emergency Management in Crisis Operations (SPARTACUS)*, viewed October 29, 2016, <http://www.spartacus-project.eu/home>
5. Casciati F, Casciati S, Chen Z-C, *et al.* 2014, Development of a eeliable wireless GNSS sensor network. *Proceedings of EWSHM 2014, 7th European Workshop on Structural Health Monitoring*, Nantes, France.
6. Ochieng W Y and Sauer K, 2002, Urban road transport navigation: performance of the global positioning system after selective availability. *Transportation Research Part C*, vol.10(1), 171–187. https://doi.org/10.1016/S0968-090X(02)00008-6.
7. Lechner W and Baumann S, 2000, Global navigation satellite systems, *Computers and Electronics in Agriculture*, vol.25(1): 67–85. https://doi.org/10.1016/S0168-1699(99)00056-3.
8. Leick A, 1995, *GPS Satellite Surveying*, 2nd edn, John Wiley & Sons, Inc., USA.
9. Parkinson B W, Spilker J J Jr, Axelrad P, *et al.* 1996, Global Positioning System, Volume I, American Institute of Aeronautics and Astronautics, Inc., USA.
10. Odijk D, Nadarajah N, Zaminpardaz S, *et al.* 2016, GPS, Galileo, QZSS and IRNSS differential ISBs: estimation and application, *GPS solutions,* in press. https://doi.org/10.1007/s10291-016-0536-y.
11. Quan Y, Lau L, Roberts G W, *et al.* 2016, Measurement signal quality assessment on all available and new signals of multi-GNSS (GPS, GLONASS, Galileo, BDS, and QZSS) with real data, *Journal of Navigation*, vol.69(2): 313–334. https://doi.org/10.1017/S0373463315000624.
12. Vittuari L, Gottardi G and Tini M A, 2015, Monumentations of control points for the measurement of soil vertical movements and their interactions with ground water contents, *Geomatics, Natural Hazards and Risk*, vol.6(5–7): 439–453. https://doi.org/10.1080/19475705.2013.873084.
13. Zanutta A, Vittuari L and Gandolfi S, 2008, Geodetic GPS-based analysis of recent crustal motions in Victoria Land (Antarctica), *Global and Planetary Change*, vol.62(1): 115–131. https://doi.org/10.1016/j.gloplacha.2008.01.001.
14. Abbondanza C, Altamimi Z, Sarti P, *et al.* 2009, Local effects of redundant terrestrial and GPS-based tie vectors in ITRF-like combinations, *Journal of Geodesy*, vol.83(1): 1031–1040. https://doi.org/10.1007/s00190-009-0321-6.
15. Fuggini C, 2010, *Using satellites systems for structural monitoring: accuracy, uncertainty and reliability*. Ph.D. dissertation, University of Pavia, Pavia, Italy.
16. Hackel S, Steigenberger P, Hugentobler U, *et al.* 2015, Galileo orbit determination using combined GNSS and SLR observations. *GPS Solutions*, vol.19(1): 15–25. https://doi.org/10.1007/s10291-013-0361-5.
17. Fernández-Hernández I, Rijmen V, Seco-Granados G, *et al.* 2016, A navigation message authentication proposal for the Galileo Open Service, *Navigation: Journal of the Institute of Navigation*, vol.63(1): 85–102. https://doi.org/10.1002/navi.125.
18. Borio D, Gioia C, 2016, Galileo: the added value for integrity in harsh environments, *Sensors*, vol.16(1): 1–23. https://doi.org/10.3390/s16010111.
19. Spectracom, 2013, GSG-5 / 6 Series GPS and GLONASS Simulator - User Manual, NY, USA.
20. Guinamard A, 2014, *Ellipse AHRS & INS - High Performance, Miniature Inertial Sensors User Manual*, SBG Systems, Rueil-Malmaison, France.
21. Trimble, 2004, NMEA-0183 Messages Guide for AgGPS Receivers, *Trimble Navigation Limited*, Kansas, USA.
22. Casciati F, Casciati S, Chen Z-C, *et al.* 2015, Collecting data from a sensor network in a single-board computer. *11th International Conference on Damage Assessment of Structures (DAMAS 2015). Journal of Physics: Conference Series,* vol.628(1):1–8.
23. Texas Instruments, 2009, CC2530 Software Examples User's Guide, *Texas Instruments Incorporated*, Dallas, Texas, USA.
24. Crossbow Technology Inc, 2016, *CXL-LF Series - High Sensitivity Accelerometers, Document Part: 6020-0002-01 Rev E*, San Jose, California, USA.
25. Pegasem Messtechnik GmbH, 2015, *GSS Series Ground Speed Sensor — User Manual* V 1.38, Noerdlinger, Germany.
26. Casciati S, Chen Z-C, Faravelli L *et al.* 2016, Synergy of Monitoring and Security. *Smart Structures and Systems,* vol.17(5): 743–751. https://doi.org/10.12989/sss.2016.17.5.743.

RESEARCH ARTICLE

Feasibility study of a grid-tied 2MW floating solar PV power station and e-transportation facility using '*SketchUp Pro*' for the proposed smart city of Pondicherry in India

Ankit Kumar Singh[1], Dwipen Boruah[2], Lakshey Sehgal[3] and Ramaswamy Arun Prasath[1*]

[1] Laboratory for Energy Materials and Sustainability, Centre for Green Energy Technology, Pondicherry University, Puducherry 605014, India

[2] GSES India Sustainable Energy Pvt. Ltd., New Delhi 110019, India

[3] BA-PAN Engineering Co., New Delhi 110020, India

Abstract: The race of smart cities in India places Pondicherry at 75th position. To improve its ranking position for smart city race, we propose the implementation of 2MW Floating Solar Photovoltaic (FSPV) system where a large water body could be used for generation of solar power. The floating PV system can be used to attain much higher efficiency compared to its counterpart on land based PV system. The proposed FSPV system could cover solar panel of 1/3rd area of the proposed lake to generate 2685 MWh annually. A geo-synchronized layout has been prepared using 3D *SketchUp Pro* with Google maps. The FSPV system could cost USD 1.6 million with a payback period of 6 years. In addition, the implementation of e-transport facility by utilizing e-rickshaws with a battery capacity of 90Ah with 15 Amps DC charging facility has been proposed with an investment of USD 30000, with payback period of just 5 months. The bright side being improved overall payback due to money inflow with the implementation of e-rickshaws; greater job opportunities with benefits to physically challenged persons to improve their overall socio economic status. It is viewed that the proposed FSPV and e-transport could increase the chance to secure smart city plan for Pondicherry.

Keywords: smart city, power plant, floating solar photovoltaic, grid-tied, e-transportation facility, e-rickshaws

*Correspondence to: Ramaswamy Arun Prasath, Laboratory for Energy Materials and Sustainability, Centre for Green Energy Technology, Pondicherry University, Puducherry 605014, India; Email: raprasath.get@pondiuni.edu.in

Received: September 27, 2016; **Accepted:** November 17, 2016; **Published Online:** December 30, 2016

Citation: Singh A K, Boruah D, Sehgal L, *et al*., 2016, Feasibility study of a grid-tied 2MW floating solar PV power station and e-transportation facility using *'SketchUp Pro'* for the proposed smart city of Pondicherry in India. *Journal of Smart Cities*, vol.2(2): 49–59. http://dx.doi.org/10.26789/JSC.2016.02.004.

1. Introduction

1.1 General Overview

The 21st century is regarded as the century of cities. According to the recent report by UN Department of Economic and Social Affair, more people live in urban areas than in the rural areas. This population shift has grown from 30 percent (746 million) in 1950 to 54 percent (3.9 billion) and is expected to be 66 percent by 2050, adding around 2.5 billion to the present figures. For developing countries like India, the growth rate is more rapid compared to the American and European continent. India is expected to add 404 million urban dwellers to

its cities in the next 30 years[1]. The unprecedented rate of urban growth has imposed risks and concerns such as: congestion, pollution, burdened resources, lack of energy, mismanagement. This has been seen very clearly in the case of the December 2015 flood in Chennai city and open areas. Thus, it came up as a motivation for a new idea of 'SMART CITIES'. The idea entails the concept of self-developing and people friendly environment using the advance technologies, management and feedback systems for a sustainable and energy independent city. The motivation to transform the present cities to more liveable ones, the government of India has taken an initiative of converting 100 cities into 'smart cities' to provide core infrastructure and sustainable environment that needs the application of sustainable management and promotion of territory with a bottom up approach to subside the crisis and concerns faced by the present cities. The Oulgaret municipality of Pondicherry is among one of those. A proposal for the smart city was put forward by the city and town planning department of Puducherry. The municipality has proposed the framework development approach of RRG (Retrofitting, Redevelopment, and Greenfield) that will be implemented under different strategies of development and integrated vision using innovative planning and smart solutions[2].

One of the major key factors to make a city-smart is by tackling the energy demand through smart and innovative means. At present, the use of renewable energies is regarded as the perfect solution for growing energy demand as they are pollution free and economical. In the guidelines provided for the smart city development, one of the essential features mentioned is: assured electricity supply and 10% of the total consumption of the smart city to be produced from solar[3]. This feature is a step forward towards attaining energy independence and will be a guiding light for the upcoming cities in the race to become smart. Solar energy has gained an upper hand in the race of renewable technologies due to the long term research and development in this field. The technology today has become not just cheaper but also more effective and feasible in the equatorial countries where the solar irradiance is high. Government of India has aimed to achieve 100 GW through solar under JNNSM [Jawaharlal Nehru national solar mission] till 2022[4]. Under this mission government is planning to set up power plants throughout the country using solar thermal and solar photovoltaic technologies. The solar photovoltaic technology is comparatively more feasible and effective in most of the areas it is easy to install in the remote locations and solar panels itself converts the sunlight directly to electricity (photovoltaic conversion). The major drawback with the solar technology is that it requires a large area, *i.e.*, a 1MW power plant requires about 4–5 acres of land which cannot be further utilized for other purposes. Another such drawback is the increase in temperature of the solar cell. The paper focuses on proposing a floating solar photovoltaic system that can be installed on the water body present in the Karasur village.

1.2 Why Floating Solar Photovoltaic (FSPV)?

The FSPV system has the following advantages over the land based solar power plants. The land has become a shrinking commodity due to the rising population. This has exponentially increased the cost of the land thereby increasing the project cost; land utilized for the solar plants cannot be utilized for the other purpose, particularly in urban areas. These issues can be sorted out in FSPV system as it will utilize the water body. In addition, the land based systems are also prone to high temperature. The temperature has an indirect relation with the efficiency of solar power plants[5,6]. This means that the increase in the solar panel temperature decreases the power out efficiency in solar plant. Whereas in the floating system, the temperature around the panel reduces due to the evaporation and hence maintaining higher efficiency of generation than the land based system. The floating system also reduces the evaporation rate, maintaining the water level and also restricts the algal bloom by blocking out the sunlight[7]. The FSPV also embellishes the site making it a public attraction and can also be synced with a solar charging station at the site for the electric vehicles in the smart city area. This can be a very attractive means for the smart city as the proposal for solar PV over the canals helped the Coimbatore city to secure 13th position in the race of smart city proposal in India. The Oulgaret municipality of Puducherry, which is ranked 75th, has been listed among the cities that have to upgrade in a special fast track initiative. There are 23 cities which have been included in this list and have been given a chance to upgrade their proposal to make it more attractive and smart. Among these 23 cities, the cities which achieve the benchmark set by the present top 20 cities will be funded on accelerated basis in 2016–2017 to achieve its goal of becoming a smart city[8].

The rapid growth in transportation sector has con-

tributes pollution in manifolds. The rise is due to the dependency of transportation sector over the non-renewable resources. The present Indian government has come up with different schemes and benefits like "Deendayal E-Rickshaw Scheme" to promote the use of greener means of transportation and reduce the emission levels which renders us a smart solution to fight the serious issues like pollution and poverty trap[9]. A study shows that 80% of the e-rickshaw drivers have felt an increase in their daily wages and betterment in their living condition after shifting into the profession from their previous ones[10]. At present, India is highly dependent on non-renewable resources for its energy requirements. Thus, the charging facilities for electric vehicles would not entirely benefit until and unless they use renewable source to power the battery bank or for feeding the grid as otherwise it will only shift the site of pollution from the city to the outskirts, where these coal/diesel fired power plants are installed. Taking this into consideration, we included the charging facility in the vicinity that will be powered by the grid which is being fed by the floating solar PV system in the proposal. Hence, we propose a floating solar photovoltaic system along with a charging facility for the e-rickshaws for the location, helping the municipality to secure the position in the race of becoming a smart city.

1.3 FSPV Systems across the Globe

Choi has studied various factors such as wind, water flow, irradiation, shadowing, *etc*. to determine the suitability of the reservoir of Hapcheon Dam, South Korea for the floating system[11]. The comparison of power generation and environmental impact between the floating and land based PV system was discussed. The results showed that the power generation efficiency is higher in the floating system because of evaporation from water bodies and it also has a lesser environmental impact compared to land based system[12]. Lee *et al.* explored about the pultruded fibre reinforced polymeric plastic (FRP), which is a low-density, durable and recyclable material required to develop a light weight structure which can float over water and provides strength comparable to the conventional floating structure used for the PV system. Mechanical tests determine its appropriateness as a floating structure to support the PV system which was installed at a sea site in Korea[13]. The issues faced by land based solar PV systems and its elimination in the floating systems has been reported. It has been noted that the design parameters of a 10 kW floating solar PV system stating its cost to be 1.2 times more than the land based system[7]. Korean Water Resources Corporation (K-water) has completed the installation of two floating solar PV power plants at 100 kW and 500 kW respectively. Analysis and comparison of these two systems to their counterparts on land was done and found that the floating system had 10% greater generation efficiency than their counterparts on land[14]. The new Photovoltaic Floating Cover System (PFCS) for the agricultural reservoirs to minimize evaporation loss along with generating income in the form of electricity. This makes the system an efficient tool for agriculture industry[15]. The floating solar photovoltaic system proposed by Polienergie is suitable for any type of water surface. The system can accommodate any size of panel, highly adaptable to changes in water level and they used micro-inverter technology which eliminates the need of structures around water bodies for inverters. All the materials are recyclable and can also be installed over drinkable water reservoirs[16].

A novel idea for the offshore PV system achieved by placing flexible thin film PV that floats on the surface. The cost and performance analysis was performed to compare to offshore wind installations. The results show that the PV system was economically competitive and the specific yield was higher for the thin film system than for other offshore technology when assessed in terms of GWh/km^2[17]. The Maltese island can exploit its solar potential through the offshore (floating) PV technology and integrate it to the conventional electric generation system to attain cost benefits and CO_2 savings[18]. The offshore applicability of the solar technology also helps to exploit the opportunity to use it with other complimentary energy sources like wind and wave[19]. A water-saturated microencapsulated phase change material (MEPCM) has been studied in the water surface floating PV panels to show the effect on its temperature and power generation efficiency during summer. The results show that the power generation efficiency improved by 2.1% when the panels were treated with a 5cm MEPCM[20]. The design feature, CO_2 analysis, economic and other benefits of the FPCS (floating photovoltaic cover system) using a 20 kWp prototype was studied in detail by Redón *et al.* The results observed led to increase the installation by covering the entire area of the reservoir (4490 m^2 and 300 kWp) generating 425,000 kWh/year, saving 5000 m^3 of water annually and 2048.5 tonnes of CO_2 for a service life of 20 years[21]. Meanwhile, the PV inte-

grated floating surface that is technically feasible and economically viable was analysed[22]. A study for the use of floating PV in Brazil was conducted. A fraction of three selected reservoir was occupied by the system for the study and the results flashed an increase in average conversion efficiency of 12.5%. PVSYST software was used to construct the electric production scenario which on comparison showed that energy produced by the PV system when spread over the entire area of the three reservoirs will be 18.8% of the electricity demand of its largest city Fortaleza[23]. A 100 kWp capacity floating solar PV system has been proposed for Loktak Lake, Manipur. The project was initiated by Manipur Renewable Energy Development Agency (MANIREDA)[24]. The Damodar Valley Corporation has also planned to setup 1000 MW worth solar system covering 2500 km of irrigation canal. Kerala is planning for another 1MW pilot project over Meenkara dam in Palakkad district. NHPC (National Hydroelectric Power Corporation) is also planning to set up a 50 MW floating solar PV project in Kerala[25].

1.4 Project Location

Figure 1 shows the site map of green field development, whereas Figure 2 is a detailed map of the location with the proposed structural layout[26]. The hatched area shown in Figure 1 can be developed right from the scratch under the Greenfield development strategy, covering Sedarapet and Karasur village. The earmarked site is the southernmost lake present in the proposed smart city map, in the Karasur village of Pondicherry, India. The latitude and longitude of the location is: 11.98° N and 79.74° E. At this particular location, we get a high amount of solar irradiation; thereby making it a very attractive site for the proposal of solar PV systems.

2. Methodology and Materials

The detailed literature search on the topic 'FSPV systems' was done using search engines such as web of knowledge, Scopus, and Google scholar. Free software 3D SketchUp 2015 modelling was used to prepare the geo-synchronized layout with Google map for the proposed water body. Basic survey accessories were used for manual survey of the site and compared with geo-synchronized layout. Solar irradiation, wind and temperature data were derived from NASA website.

2.1 Methodology

A manual survey on the proposed site was performed to determine the shadow casted by the structures present around the lake and orientation of the site. As the area comes under the Greenfield development policy,

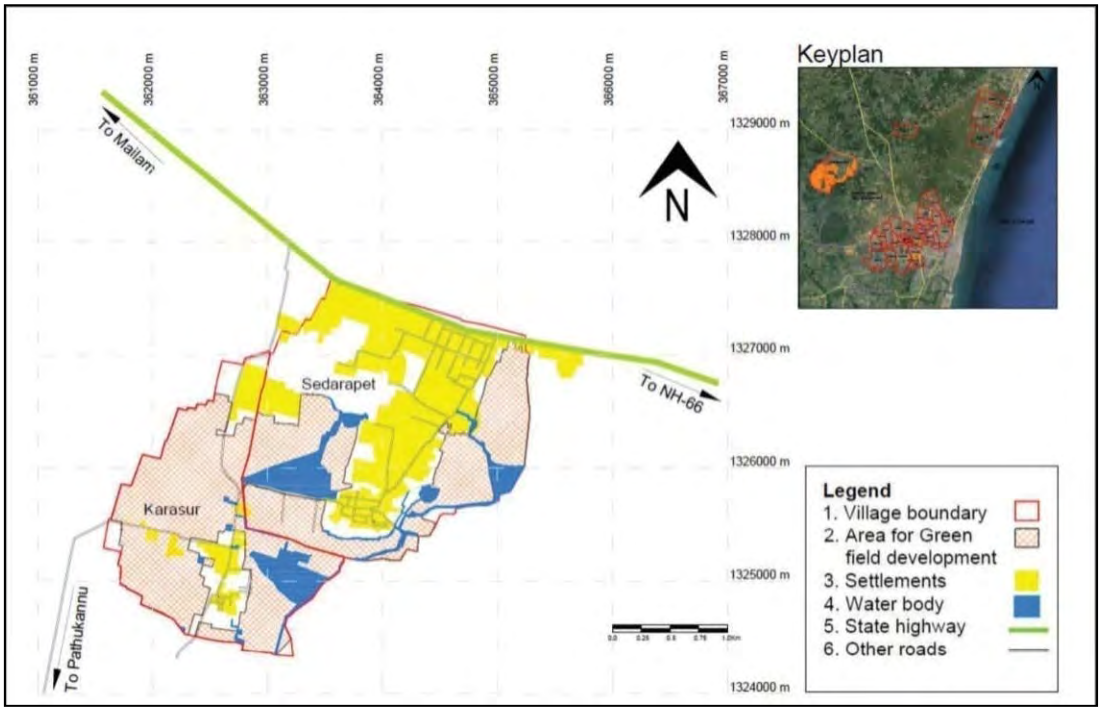

Figure 1. The site map for Greenfield development.

Figure 2. Site map with the proposed structural layout.

there is no construction work done around the location at present. With reference to the draft of the Oulgaret Smart city[26] and the town planning authorities, there will be no shadow formed over the lake surface as the planned structure are on the south- western side of the lake and are not high enough to generate shadow on our proposed system. At present, the trees around the location which are 20–30 feet high cast shadow at the location but this can be eliminated at the time of installation for the smooth function of FSPV system.

Solar radiation data: The location receives a good amount of annual solar radiation with an average of 5.145kWh/m²/day. This amount of radiation is more than the average solar radiation and hence, it is an appropriate site for our system. Solar radiation data for the site has been derived from NASA website (http://eosweb.larc.nasa.gov/cgi-bin/sse). The monthly average solar radiation is shown in Figure 3.

Temperature data: The average monthly temperature of the site is 27.14°C. The average monthly variation in ambient temperature profile for the site is shown in the Figure 4. As this temperature profile is measureed over land, there might be some variation when we consider the system over water body. This variation will always

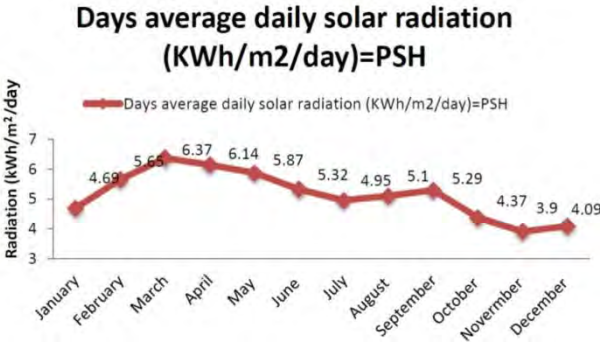

Figure 3. Monthly average solar radiation.

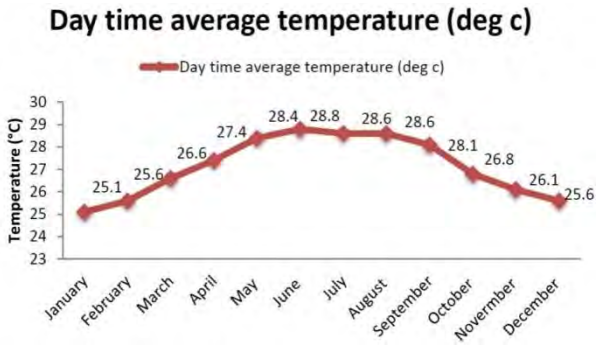

Figure 4. Monthly average temperature (°C).

be less than the temperature measured over land due to the evaporation of water and thus there will be no requirement of artificial cooling system.

Wind data: According to the data obtained for the wind velocities, the average annual wind velocity at the site is around 2.5 m/s. The monthly variation in the wind velocity is shown in Figure 5. The wind velocity is an important factor to be considered in our system as the wind might cause the change in the orientation of our system leading to decrease in the energy yield. As the site is close to the coast, conditions like storm and cyclone might prevail. For this, the system can be designed with appropriate materials such that it can withstand high wind velocities and reduce the damage imposed by the cyclonic winds.

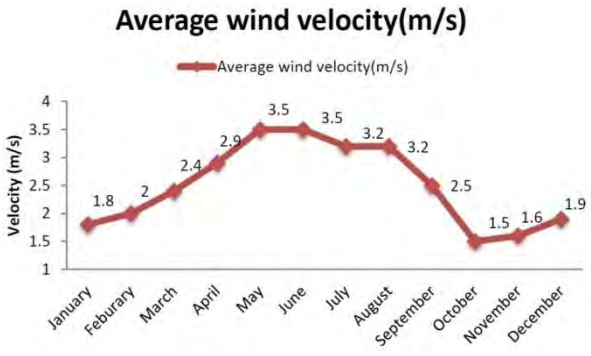

Figure 5. Monthly average wind velocity.

2.2 Proposed Structural Materials

Floating Solar PV Systems

Floating system: The first and foremost component required for our system is a floating structure which should be light weight, able to withstand the load of the setup and can be formed at a large scale. A site specific planning was done to determine the structure of floating system that can be designed to keep the setup afloat. We propose a hexagonal structure with each side of 60 m covering an area of 12471 m². A total of three such hexagonal structures are proposed for the site which makes a total of 37412 m². A pontoon type or a buoyant system has been suggested to achieve buoyancy and stability for this setup and arrangements should be made to accommodate the grids of panels designed (structural safety assessment of ocean-floating photovoltaic structure model)[27]. A light weight, high strength durable, fireproof material[28] such as reinforced concrete shell with a core of expanded polystyrene (EPS) can be used. Pultruded fibre reinforced polymeric plastic (PFRP) is one such material which is superior to the conventional materials used for structural fabrication for a better result in floating PV[13].

Mooring system: A mooring system is very important part of the system. The wind and other natural and man-made factors might cause a drift or change in the position of our system; this will result in decrease in our system efficiency due to change in orientation and might also result in physical damage to our system. To avoid these issues, an anchoring system using a high tensile strength material is to be devised so that it can fix the position of our system and also be useful to make adjustments during the variation in water level in the water body. The material preferred must have high Young's modulus, low density and high strength, such as polyester fibre.

Photovoltaic system: A photovoltaic system comprises of all the equipment that are required for the generation of electricity using the solar irradiation. In this section, we will discuss about the different equipment and their setup. For the proposal, we have considered a module with multi-crystalline technology. The modules generate 300Wp DC output, high torsion and corrosion resistance and high resistance to moisture ingress. Here, we have framed 4 panels together in a 2 × 2 arrangement for our purpose. The detailed specifications are as follows: maximum power = 300 Wp, open circuit voltage (V_{oc}) = 44.8V, short circuit current (I_{sc}) = 8.71A, module efficiency (η) = 15.10%, dimensions (L × W × H) = (1984 × 1000 × 40) mm. The technical drawing of the module is given in Figure 6.

Electrical system: The electrical system is considered as the soul of the system, it comprises of different devices and their connections which is vital for the functioning of a power plant. An inverter is regarded as the heart of the power plant; it is the device that regulates the voltage fluctuations and converts this fluctuating voltage into a single or three phase output which can be fed into the grids or stored into the storage devices. We have considered a water-proof micro-inverter as it optimizes each panel alone instead of doing it for the complete system as in case of a central inverter, which may be a weak link for the system and also causes decline in the output. The micro-inverters also reduce the need of a land based setup for the installation of a conventional central inverter. They also have a longer life than the conventional systems and in case of failure; it will not stall the production of the complete plant. The specifications of a grid tie micro-inverter are as follows: DC input with max. power input 310W, max. input DC voltage = 48V and max.

DC short circuit current = 15A, MPPT efficiency (η) = 99.4%. The panel ratings lie within the range of the given three phase micro inverter rating. It produces an AC output which is synchronized to the grid frequency range and able to work under the atmospheric condition prevalent at the site of installation. The output of the three phase micro inverters is connected in parallel. This output can be further enhanced using a three phase step-up transformer 440V/11kV depending upon the requirement of the utility grid.

Other electrical accessories: The cables must conform to the marine grade and need to be selected accordingly to keep the voltage drop and losses to minimum. Interconnections, combiner boxes, junction boxes *etc*. should be selected properly according to the regional standard. All the accessories have to work under the prevalent atmospheric condition and electrical rating. A net-metering device needs to be installed to keep a check on the inflow and outflow of the power to and from the grid. It provides an insight of the generation. The electrical layout of the floating SPV system is shown in Figure 7.

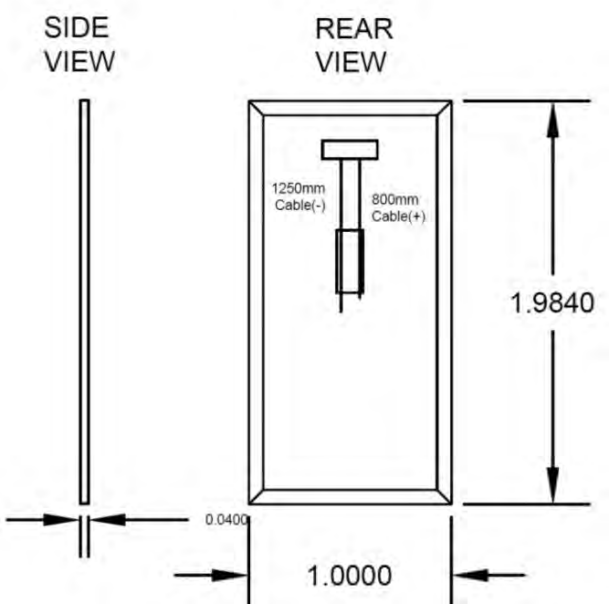

Figure 6. Technical drawing of the module.

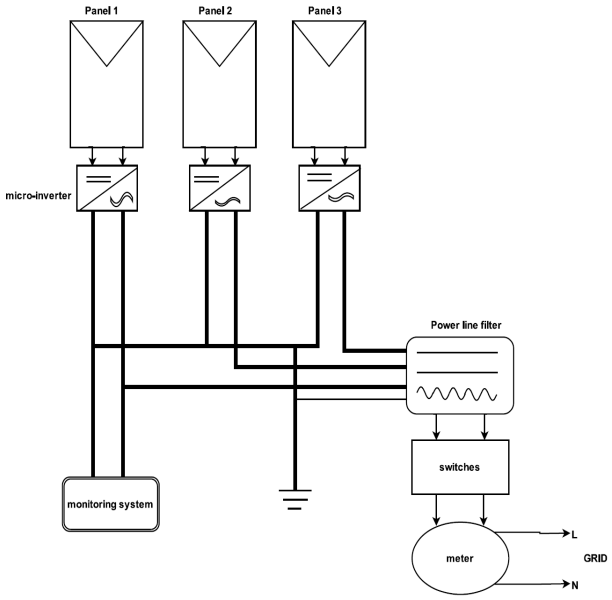

Figure 7. Electrical layout of floating SPV system.

3. Project Implementation Array Spacing and Layout

The proposed site for our floating solar PV power plant is the southernmost water body in the proposed smart city map. According to the town planning officials, the proposed map shows low rise settlements on the south-western side of the site and it might merely cast a noon shadow on our system. A set of four modules were framed together in 2 × 2 configurations with a total of 4 panels together in a portrait layout. This frame gives a clearance of 0.152 m to the module from the ground. The modules are tilted at an angle of 12° from the base. Figure 8 shows the layout of individual module. This was performed by using 3D modelling software *SketchUp Pro* 2015 along with the array-o-matic_v1.11 component plugin to 0.95 m between the modules in the same row and 2.83 m spacing between adjacent rows. This spacing also includes the gap for maintenance and cleaning purposes.

The active area, *i.e.,* the total area estimated in electricity generation by incident solar irradiation, is 13416 m² out of 37412 m². An area of 2065 m² was provided on the right end of the floating structure to accommodate the junction boxes and other electrical devices. Figure 9 to Figure 11 shows the proposed layout of the plant, front view and side view of the floating SPV power plant.

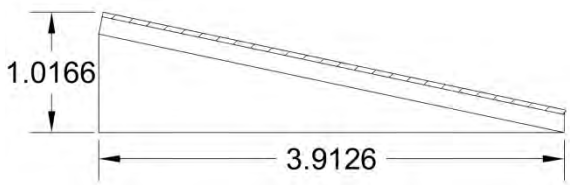

Figure 8. Layout of individual module.

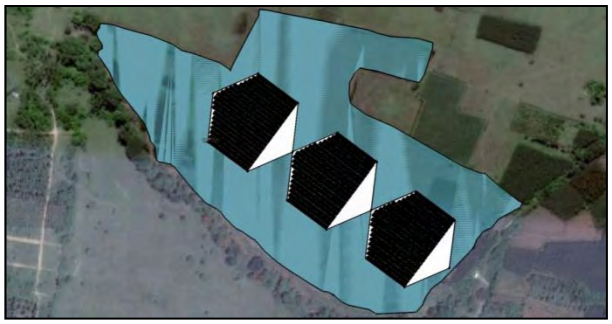

Figure 9. Layout of the floating SPV power plant.

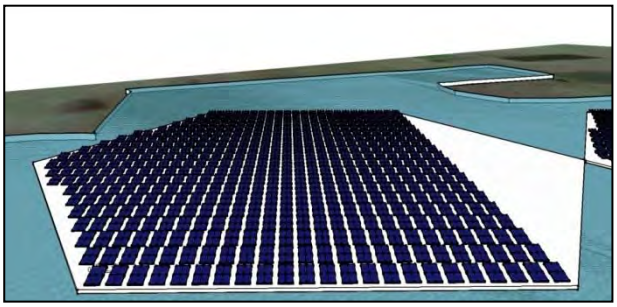

Figure 10. Front view of the floating SPV power plant.

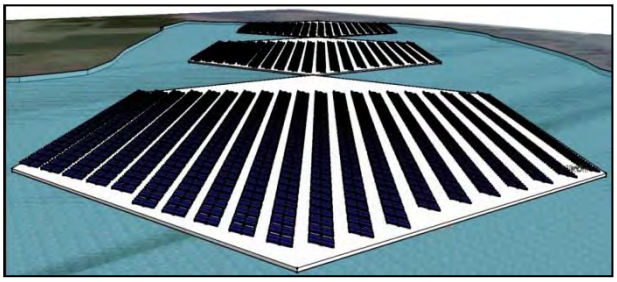

Figure 11. Side view of the floating SPV power plant.

Estimation for Annual Yield

To obtain the annual energy yield, various standard parameters such as daytime temperature, NOCT, annual degradation, *etc*., are considered. A total of 6708 panels of 300 Wp each are considered for our system, making it a 2MW system. By utilizing the parameters, losses and other factors we estimate the total annual yield of 2946.5 MWh for the first year and 2433.5 MWh for the 25th year. The average energy yield of the plant taking the life time to be 25 years is 2658 MWh annually. This yield will be about 7.5% greater than the land based system.

4. E-Transport Facility and Its Trend

The electric vehicles or EV's can be classified depending upon the technology being used to provide energy to the electrical drive. Mainly two technologies are being focused on, namely fuel cell and battery. Battery technology is being used for the analysis in this report as it is being widely used at a commercial level[29]. Emphasis on a major concern that EV integration will put burden on grid and thus, many studies have been conducted to mitigate the impacts of EV onto grid[30]. The researchers believed that there will be more pollution if energy from non-renewable sources of energy is fed into the grid; thus, it is better to have more share of renewable energy power plants integrated with the grid[31]. The present difficulties with EV technology is battery cost and range anxiety that it gives while in use; thus causing a concern on reliability and it cannot be ignored that even if EV range exceeds or is equal to gasoline vehicle, it will add to increase the weight and size of the vehicle, thus making the vehicle less efficient and more expensive[32].

The EV industry is going to pick up growth only if major areas like government policy and regulation, technology, customer power are worked on by the private sector in tandem with the public sector[33]. The study highlighted the points that governments around the world are providing subsidy on EV's is acting as a boon to the industry; this trend should continue and more tax incentives should be provided to EV manufacturers and EV owner[34]. The integration of renewable energy into the residential grids will pave way for electric vehicles[35]. A comparison between the economic status, showing that 80% of the e-rickshaw drivers have felt an increase in their daily wages and betterment in their living condition after shifting into this profession from their previous ones[7]. According to the press release by the ministry of road transport and highways in June 2014, the union minister has proposed a scheme to the prime minister that might be called 'Deendayal E-Rickshaw Scheme' to empower the use of e-rickshaws and also using it as a means to overcome the poverty[9].

4.1 E-Rickshaw Specification

The e-rickshaw is a battery powered vehicle that can be used for commuting for short distances of 5–10 Kms. The e-rickshaws being proposed in our project has the following specifications:

(i) It is powered by a 800W brushless DC motor which is supported by 90Ah/48V battery bank incorporating lead-acid technology.

(ii) The batteries used are deep discharge batteries with 80% depth of discharge (DOD). Their complete

charging of the battery will require almost 8.817 kWh.

(iii) It has a frame/chassis of steel with a differential transmission mode.

(iv) It has rear wheel drive and can carry up to 6 passengers at a time.

(v) It covers a distance of 70 Kms in one complete charge.

4.2 Charging Facility Specification

The charging facility is proposed to be established at parking facility in the vicinity of the proposed floating solar PV power plant. This is to extend the benefits of the solar PV plant to support the purpose of efficient urban mobility and public transport. The charging facility will have 15 Amps DC charging facility with 48V output. We propose to install 20 such points at the parking facility to support 20 e-rickshaws as a pilot initiative. Similar facilities can be replicated at different part of the city where the route is most suitable and on which these vehicles could be used to maximize the commercial benefit. Energy storage capacity of the battery bank is estimated as 8817 Wh, *i.e.*, 8.817 kWh. Hence, we require a total of 176.3 kWh of energy charge 20 e-rickshaws per day. The 2MW plant can be expected to generate 8000 kWh of energy per day. The energy extracted from the grid will be 176.3 kWh of energy per day for the charging station. This will amount to 2.20% of energy produced by the solar PV plant every day. The charging time could vary from 6–7 hours to completely charge each rickshaw as we have plans to charge the battery at C/6 rate.

5. Cost Estimation and Payback Period

As per literature review, the cost of the floating system is about 1.2 times greater than the conventional land based system[5] but in this cost, the land cost is not considered which is required for a land based system. The cost of the floating solar PV system can be estimated around USD 1.6 million. The payback period is the time span in which the cost of the yield becomes equal to the capital invested in installation. According to the current solar tariff of USD 0.10 per kWh for floating system, the payback period is expected to be less than 6 years without the subsidy provided by different state and national funding agencies. As per the market research, the total capital expenditure for the e-rickshaw and its charging facility is estimated to be USD 30,000. Considering that the maximum operating days to be 300, the cost of electricity taken from the grid will be around USD 5500 per annum at USD 0.10 per kWh electricity rate (in Pondicherry, India). Electricity cost per e-rickshaw per day will be close to USD 1. The maintenance cost will be around USD 75 per annum. This will make the operational expenditure per vehicle per day to be around USD 1.2. According to the market data available, the earnings per day from the single vehicle will be around USD 11. Therefore, the profit earned from 20 e-rickshaws will be around USD 196. The payback period for the system will be just 5 months approximately.

6. Conclusion

The proposal for a 2MW floating solar photovoltaic power plant can be implemented in different phases as it requires a decent capital cost including the maintenance cost. The challenges to be dealt are the fabrication of huge floating structure, protection during cyclones and other such natural calamities, high grade waterproof cabling, high tensile strength and corrosion resistance anchoring cables, water ingress resistant modules and other electrical devices. The high average solar irradiation of 5.145 kWh/m²/day received in the proposed location makes it a perfect location for installation of solar photovoltaic technology. We performed shadow analysis by using 3D modelling software *SketchUp Pro* 2015 along with the array-o-matic_v1.11 component plug in to be 0.95 m between the modules in the same row and 2.83 m between the adjacent rows. The FSPV system consists of three hexagonal structures of 12470 m² each with the active area of 4472 m² accommodating 559 modules of 4 panels each, making the system to be a total area of 37412 m², with the total active area to be 13416 m² consisting a total of 1677 modules of 6708 panels of 300 kW each. The high average annual energy yield of 2658 MWh will make it better with around ~7.5% higher efficiency than the land based system. Three phase grid tied micro-inverters has been proposed. The output will be stepped up further using a step up transformer of 440V/11kV or others as per the utility grid requirement. It has been calculated that the payback period will of less than 6 years without the subsidy provided by the related agencies. Once commissioned fully, it can save 6000 tonnes of CO_2 during its life span of 25 years. The proposed e-rickshaw and its charging facility required a capital cost of USD 30,000 and the operational cost to be around USD 1.2 per e-rickshaw per day. The profit earned per day on the capital expenditure will be

USD 196 and the payback period will be around 5 months. The fleet of e-rickshaw will replace a fleet of diesel run vehicle, thereby offsetting 56.3 tonnes of CO_2 per year from direct exposure on roads. This together will make our proposal of USD 1.6 million and the payback period of less than 5 years with reduction of 7400 tonnes of CO_2 emission in the atmosphere.

Conflict of Interest and Funding

No conflict of interest was reported by all authors. One of the authors (A.K.S) acknowledges MNRE (Ministry of New and Renewable Energy, India) for providing the scholarship to support his studies at Centre for Green Energy Technology, Pondicherry University.

References

1. United Nations, Department of Economic and Social Affairs, Population Division, 2014, *World urbanization prospects*, viewed September 10, 2016, <https://esa.un.org/unpd/wup/Publications/Files/WUP2014-Highlights.pdf>
2. *Strategy*, viewed January 30, 2015, <http://www.smartcities.gov.in/writereaddata/Strategy.pdf>
3. Ministry of Urban Development Government of India, 2015, *India smart city mission*, viewed September 3, 2016, <http://smartcities.gov.in/writereaddata/winningcity/DavanagereSCP.pdf>
4. Cseindia.org, 2015, *GEF national workshop in India (MNRE), May 13, 2015: Renewable energy in India: Growth and targets*, viewed August 30, 2016, <http://cseindia.org/docs/photogallery/ifs/Renewable Energy in India Growth and Targets.pdf>
5. Swapnil D, Jatin N S, and Bharath S, 2013, Temperature dependent photovoltaic (PV) efficiency and its effect on PV production in the world — A review. *Energy Procedia*, vol.33: 311–321. https://doi.org/10.1016/j.egypro.2013.05.072
6. Subhash C, Purohit A, Anshu S, *et al*., 2015, A study on photovoltaic parameters of mono-crystalline silicon solarcell with cell temperature. *Energy Reports*, vol.1: 104–109. http://dx.doi.org/10.1016/j.egyr.2015.03.004
7. Paritosh S, Bharat M, and Debojyoti S, 2015, Design parameters of 10kw floating solar power plant. *International Advanced Research Journal in Science, Engineering and Technology*, vol.2: 85–89. http://dx.doi.org/10.17148/IARJSET
8. Ministry of Urban Development, Government of India, 2016, *Smart city mission*, viewed September 16, 2016, <http://smartcities.gov.in/writereaddata/Ranking_of_Smart%20Cities.pdf>
9. Press Information Bureau, Ministry of Road Transport and Highways, Government of India, 2014, *Proposed Deendayal e-rikshaws scheme*, viewed July 30, 2016, <http://pib.nic.in/newsite/PrintRelease.aspx?relid=105700>
10. Shashank S, 2014, *A study of the battery operated e-rickshaws in the state of Delhi: Researching Reality Summer Internship Report*, Centrefor Civil Society, <https://ccsinternship.files.wordpress.com/2014/06/323_study-of-the-battery-operated-erickshaws-in-the-state-of-delhi_shashank-singh.pdf>
11. Choi Y-K, 2014, A case study on suitable area and resource for development of floating photovoltaic system. *International Journal of Electrical, Computer, Energetic, Electronic and Communication Engineering*, vol.8: 828–832. <http://scholar.waset.org/1999.5/9999567>
12. Choi Y-K, 2014, A study on power generation analysis of floating PV system considering environmental impact. *International Journal of Software Engineering and Its Applications*, vol.8: 75–84. https://doi.org/10.14257/ijseia.2014.8.1.07
13. Lee Y-G, Joo H-J, and Yoon S-J, 2014, Design and installation of floating type photovoltaic energy generation system using FRP members. *Solar Energy*, vol.108: 13–27. https://doi.org/10.1016/j.solener.2014.06.033
14. Choi Y-K, Lee N-H and Kim K-J, 2013, *Proceedings, The 3rd International conference on circuits, control, communication, electricity, electronics, energy, system, signal and simulation: Empirical research on the efficiency of floating PV systems compared with overland PV systems*. vol.25: 284–289. <http://onlinepresent.org/proceedings/vol25_2013/66.pdf>
15. Ferrer-Gisbert C, Ferrán-Gozálvez J J, Redón-Santafé M, *et al*., 2013, A new photovoltaic floating cover system for water reservoirs. *Renewable Energy,* vol.60: 63–70. http://dx.doi.org/10.1016/j.renene.2013.04.007
16. Polienergie s.r.l, 2012, *Floating photovoltaic system*, viewed September 15, 2016, <http://polienergie.com/img/floating_photovoltaic_system_ENG.pdf>
17. Trapani K, Millar D L, and Smith H C M, 2013, Novel offshore application of photovoltaics in comparison to conventional marine renewable energy technologies. *Renewable Energy*, vol.50: 879–888. http://dx.doi.org/10.1016/j.renene.2012.08.043
18. Trapani K and Millar D L, 2013, Proposing offshore photovoltaic (PV) technology to the energy mix of the Maltese islands. *Energy Conversion and Management*, vol.67: 18–26. https://doi.org/10.1016/j.enconman.2012.10.022
19. Fiaschi D, Manfrida G, Secchi R, *et al*., 2012, A versatile system for offshore energy conversion including diversified storage. *Energy*, vol.48: 566–576. https://doi.org/10.1016/j.energy.2012.10.006
20. Ho C J, Chou W, Lai C, 2014, Thermal and electrical

performance of a water-surface floating PV integrated with a water-saturated MEPCM layer. *Energy Conversion and Management*, vol.89: 862–872. https://doi.org/10.1016/j.enconman.2014.10.039

21. Redón Santafé M, Soler J B T, Romero F J S, *et al*., 2014, Theoretical and experimental analysis of a floating photovoltaic cover for water irrigation reservoirs. *Energy*, vol.67: 246–255. http://dx.doi.org/10.1016/j.energy.2014.01.083
22. Redón Santafé M, Ferrer Gisbert P S, Romero F J S, *et al*., 2014, Implementation of a photovoltaic floating cover for irrigation reservoirs. *Journal of Cleaner Production*, vol.66: 568–570. https://doi.org/10.1016/j.jclepro.2013.11.006
23. Sacramento E M do, Carvalho P C M, Araújo J C de, *et al*., 2015, Scenarios for use of floating photovoltaic plants in Brazilian reservoirs. *IET Renewable Power Generation*, vol.9: 1019–1024. https://doi.org/10.1049/iet-rpg.2015.0120
24. Chakraborti S, 2015, *Country's biggest floating solar plant to come up at Manipur's Loktak Lake,* viewed September 7, 2016, <http://timesofindia.indiatimes.com/city/kolkata/Countrys-biggest-floating-solar-plant-to-come-up-at-Manipurs-Loktak-Lake/articleshow/47576349.cms>
25. D'Monte D, 2015, *Maharashtra races to build India's first solar farm on dam wall*, viewed September 8, 2016, <http://www.huffingtonpost.com/entry/maharashtra-races-to-buil_b_6343148.html?section=india>
26. Government of India, Ministry of Urban Development, n.d., *Draft Smart City Proposal – Oulgaret*, viewed September 8, 2016, <http://www.smartcitieschallenge.in/files/dmfile/Draft-Smart-Cities-Proposal-oulgaret1.pdf>
27. Choi Y-K and Lee J-H, 2015, Structural safety assessment of ocean-floating photovoltaic structure model. *Israel Journal of Chemistry*, vol.55: 1081–1090. https://doi.org/10.1002/ijch.201400197
28. Koekoek M J, 2010, *Connecting modular floating structures: a general survey and structural design of a modular floating pavilion*, Master thesis, TU Delft University, viewed July 30, 2016, <http://repository.tudelft.nl/islandora/object/uuid:33b59201-1718-4dda-98f8-ee16d5b7c023?collection=education>
29. Wu H and Chang S, 2013, Exploration of a mobile service business model for electric vehicle charging stations. *Journal of Industrial and Production Engineering*, vol.30: 363–371. http://dx.doi.org/10.1080/21681015.2013.849765
30. Richardson D B, 2013, Electric vehicles and the electric grid : a review of modeling approaches, impacts, and renewable energy integration. *Renewable and Sustaiable Energy Reviews*, vol.19: 247–254. https://doi.org/10.1016/j.rser.2012.11.042
31. Tie S F and Wei C W, 2013, A review of energy sources and energy management system in electric vehicles. *Renewable and Sustainable Energy Reviews*, vol.20: 82–102. https://doi.org/10.1016/j.rser.2012.11.077
32. Colella W G, 2000, Market prospects, design features, and performance of a fuel cell-powered scooter. *Journal of Power Sources*, vol.86: 255–260. https://doi.org/10.1016/S0378-7753(99)00486-3
33. Becker D and Nagporewalla Y, 2010, *The Indian automotive industry: evolving dynamics*, KPMG International, viewed August 4, 2016, <https://www.kpmg.de/docs/Auto_survey.pdf>
34. Yap W K and Karri V, 2008, Modeling and simulation of a hybrid scooter. *International Journal of Electrical and Electronics Engineering*, vol.2: 693–698. https://doi.org/10.1504/IJEHV.2009.027676
35. Pillai J R, Huang S, and Bak-Jensen B, 2013, *Conference on Power and Energy Society General Meeting (PES) 2013 IEEE, July 21–25, 2013: Integration of solar photovoltaics and electric vehicles in residential grids*. http://dx.doi.org/10.1109/PESMG.2013.6672215

REVIEW ARTICLE

Policy-aware assessment of environmental impacts from transport in smart cities

Ioannis Kaparias[1*], Edouard Manassa[2], Niv Eden[3], Antonios Tsakarestos[4], Pierre Schmitz[5], Suzanne Hoadley[6] and Susanna Hauptmann[7]

[1] Transportation Research Group, Faculty of Engineering and the Environment, University of Southampton, Boldrewood Innovation Campus, Burgess Road, Southampton SO16 7QF, UK
[2] City University London, UK
[3] Technion – Israel Institute of Technology, Israel
[4] Technische Universität München, Germany
[5] Brussels-Capital Region, Belgium
[6] POLIS, Belgium
[7] Kapsch TrafficCom, Austria

Abstract: In recent research a performance evaluation framework for traffic management and Intelligent Transport Systems was developed, consisting of a set of Key Performance Indicators (KPIs) for the themes of traffic efficiency, safety, pollution reduction and social inclusion, all of which are key components of a smart city. One of the innovative elements of these KPIs is their ability to consider the transport policy layer, in the sense that the evaluation of the suitability and effectiveness of different strategies and ITS options is calculated in relation to the decision maker's high-level transport policy rather than objectively. This is achieved through weighting factors, whereby more important policy objectives are weighted more heavily in the calculation. But while the theoretical framework is ready to accommodate the policy layer, no methodology to determine the values of the weighting factors has been developed so far. The present study, therefore, concentrates on the development and testing of such a methodology, focusing on the environmental impact aspect of urban mobility management and ITS in the context of smart cities. The development is based on existing policy objectives and legislation in different cities and countries, while testing is carried out using the purpose-developed CONDUITS_DST software with data from microsimulation models before and after the implementation of a bus priority signalling system in Brussels, Belgium. The results show that the method captures the expected effects, but also that it is able to reflect policy objectives and deliver evaluation results in relation to their alignment with those.
Keywords: Key Performance Indicators, traffic management, pollution reduction

*Correspondence to: Ioannis Kaparias, Transportation Research Group, Faculty of Engineering and the Environment, University of Southampton, Boldrewood Innovation Campus, Burgess Road, Southampton SO16 7QF, UK; Email: I.Kaparias@southampton.ac.uk

Received: October 5, 2016; **Accepted:** November 17, 2016; **Published Online:** December 30, 2016

Citation: Kaparias I, Manassa E, Eden N, *et al.*, 2016, Policy-aware assessment of environmental impacts from transport in smart cities. *Journal of Smart Cities*, vol.2(2): 60–68. http://dx.doi.org/10.26789/JSC.2016.02.002.

1. Introduction

Cities today share common transport problems and objectives with respect to mobility management, and put great focus on Intelligent Transport Systems (ITS). The market offers decision makers a variety of ITS solutions, from which they are required to choose the most suitable and effective ones. Making this choice is a non-trivial task, however, especially given that transport problems are mul-

ti-dimensional by nature. Hence, a performance evaluation framework that addresses the various dimensions of transport problems, while at the same time reflecting the perspectives and priorities of decision makers, is required[1].

In recent research work (FP7 CONDUITS) such an evaluation framework was formulated, consisting of a set of Key Performance Indicators (KPIs) for four themes of mobility management: efficiency, safety, pollution reduction and social inclusion[2]. The KPIs were subsequently validated through before- and after-evaluation of real-world case studies in the cities of Paris, Rome, Tel Aviv and Munich, using real data supplied by the local authorities and transport operators[3–4]. Through the conduct of the case studies, it was concluded that the KPIs were easy to apply and required already available data, thus forming a very useful evaluation tool for assisting city decision makers of in the field of mobility management and ITS, and to some extent for identifying best practice and lessons learnt elsewhere.

Yet the necessity for extending the CONDUITS framework from its current state of a tool for evaluating existing systems to a tool for evaluating future systems becomes apparent, given the current economic climate and the increasing need of making as informed decisions as possible within the context of smart cities. Follow-up work within the framework of the CONDUITS-DST spinoff project, sponsored by Kapsch TrafficCom, has concentrated on integrating the CONDUITS KPIs with traffic microsimulation. The outcome has been a predictive evaluation tool for mobility management and ITS, called CONDUITS_DST, in which three of the four KPI categories have been integrated to date: the pollution generated by the various transport modes in the form of greenhouse gas emissions, the traffic efficiency, expressed through measures such as travel time and network reliability; and the traffic safety, represented by metrics such as accidents, and direct and indirect safety impacts. Preliminary testing of the tool in four European cities (Brussels, Stuttgart, Tel Aviv and Haifa) using existing microsimulation models has, again, confirmed the validity of the methodology and has demonstrated the viability, usefulness and timeliness of the approach[5–7].

One of the innovative elements of the CONDUITS approach is its ability to consider the transport policy layer, in the sense that the evaluation of the suitability and effectiveness of different mobility management strategies and ITS options is calculated in relation to the decision maker's high-level transport policy rather than objectively. In other words, the CONDUITS approach has the ability to capture the fact that a certain option that may be beneficial to one city (or country) may not be as beneficial to another, not because of the impact that it may have, but because it may not agree with the latter's high-level policy. For example, an option that delivers moderate benefits in terms of reducing particulate matter (PM) emissions but has great benefits in terms of improving traffic safety may not be the best solution for a city in which pollution reduction is a more important high-level policy objective than road safety.

From a decision maker's point of view this policy-awareness is invaluable, as it provides the means to present results to non-expert audiences (such as politicians) in a simple, fast and effective way. The policy layer is integrated in the CONDUITS KPIs through weighting factors, whereby more important policy objectives are weighted more heavily in the calculation. But while the theoretical framework is ready to accommodate the policy layer, no methodology to determine the values of these has been developed so far.

The present study, therefore, concentrates on the development and testing of a method for setting the weights in the CONDUITS KPIs. The focus here is the pollution aspect of mobility management and ITS in the form of pollutant emissions from vehicle traffic, and the relevant CONDUITS KPI is tackled. The method is based on existing policy objectives and legislation in different cities and countries with respect to the three main categories of air pollutants, namely carbon dioxide (CO_2), nitrogen oxide (NO_x) and particulate matter (PM). Testing is then carried out through the CONDUITS_DST software using data from microsimulation models before and after the implementation of a bus priority signalling system in Brussels, Belgium.

The paper is structured as follows: Section 2 introduces the background of the study, including the CONDUITS evaluation framework (KPI) for pollution reduction and a review of different air pollution policy objectives and legislation, which inform the development of the weighting methodology. Section 3 then goes on to formulate the methodology and to present the rationale behind it. The results of the testing of the method on the case study in Brussels are reported in Section 4, along with a discussion of the analysis car-

ried out. Finally, Section 5 concludes the paper and identifies areas of future work.

2 .Background

2.1 The CONDUITS Evaluation Framework

Performance measures have the ability to effectively evaluate the outputs of specific solutions. However, when attempting to conduct a higher-level evaluation through a multi-dimensional benchmarking scheme comparing different cities with each other, performance measures are generally not suitable. The reason is that such a task necessitates the systematic and synthetic description of the cities' transport policies and infrastructures and the analysis of their impacts, which can only be expressed by a set of measures reflecting each individual scheme evaluated[8]. This issue creates difficulties in the communication of the results to non-technical audiences, such as politicians and the general public, and a common way to deal with it is to combine individual performance measures into composite performance indices (KPIs)[9–10].

The main advantage of KPIs is simplicity, as it is much easier to understand and grasp a single number rather than a large collection of individual measures, whose meaning often requires trained insight and careful analysis. The disadvantage, nevertheless, is that an aggregate number does not provide immediate insight into which aspects of the performance are changing or why, making it difficult to distinguish the sensitivity of an index to changes in its component measures. However, this ambiguity may lead to some other advantages. The index increases the opportunity for all modes and markets to be included, conveys the idea that each service is important, and elevates the discussion about how to best measure and report system performance. This cooperation between modes and sectors enhances awareness, broadens perspectives and leads to more comprehensive solutions.

In line with the European Commission's strategy on the future of transport, as presented in the 2001 and 2011 white papers[11–12], a performance evaluation framework was defined by the FP7 CONDUITS project, consisting of a set of measures and KPIs for the four themes of traffic efficiency, traffic safety, pollution reduction, and social inclusion[2]. The most important KPIs for each of the four themes are listed in Table 1.

Among the KPIs of the complete framework, this study focuses on pollution reduction, and specifically the index of emissions from motor vehicles. The relevant KPI is defined[2] as the weighted sum of all distance-averaged emissions per vehicle and per vehicle type in the network, i.e.,

$$I_{pol} = \frac{\sum_{VT}\sum_{ET} w_{VT} w_{ET} Q_{VT,ET}}{\sum_{VT}\sum_{ET} w_{VT} w_{ET}} \quad (1)$$

where I_{pol} is the value of the KPI (with smaller values

Table 1. List of key CONDUITS KPIs for each of the four themes

Category	KPI	Description
Traffic efficiency	Mobility	Average travel time to different destinations in the highway and public transport networks, weighted by importance according to policy objectives
	Reliability	Average total duration of congestion on all links of the highway and public transport network, weighted by importance according to policy objectives
Traffic safety	Accidents	Average number of accidents at links and junctions of the transport network, weighted by mode (car, bus, pedestrian …) and severity (serious injury, fatality)
	Direct safety impacts	Average number of actions taken to avert safety-critical situations, weighted by mode and location according to policy objectives
	Indirect safety impacts	Total duration of safety-related critical occurrences, but not necessarily avoidances of safety hazards, weighted by mode and location
Pollution reduction	Motor vehicle emissions	Sum of all distance-averaged emissions per vehicle and per vehicle type in the network, weighted according to policy objectives
	Electric vehicle emissions	Sum of distance-averaged equivalent electricity generation emissions per electric vehicle in the network, weighted according to policy objectives
Social inclusion	Accessibility	Average number of activities (work, education, leisure, …) located within a certain travel time or distance threshold, weighted by importance according to policy
	Mobility of special groups	Proportion of trips undertaken by societal groups potentially facing social exclusion (elderly, disabled, …) for participating to activities, weighted by importance according to policy
	Public transport usage of special groups	Proportion of users of public transport services from societal groups potentially facing social exclusion, weighted by importance according to policy

Note: The values of the weights w_{VT} and w_{ET} are the policy-aware element of the KPI, and can be set by the decision maker to reflect high-level policy objectives, as will be seen next.

indicating less pollution, and hence better performance), w_{VT} denotes the weighting factor for each vehicle type in the network (passenger car, motorcycle, bus, Heavy Goods Vehicle (HGV), etc.), w_{ET} is the weighting factor for each pollutant emission type (CO_2, NO_x or PM), and $Q_{VT,ET}$ is the variable expressing the quantity of a certain pollutant emission from a certain vehicle type.

Depending on the type of evaluation, the data source of the $Q_{VT,ET}$ quantity varies. Specifically, in a before-and after-evaluation of an already realised/implemented ITS scheme, $Q_{VT,ET}$ can be obtained from actual pollutant emission data collected from the field through sensors. In the case of predictive evaluation of a proposed scheme, on the other hand, $Q_{VT,ET}$ can be calculated from the output of microscopic traffic simulation models (such as PTV VISSIM, PARAMICS or AIMSUN), combined with an appropriate pollutant emissions model (such as AIRE, COPERT or ENVIVER).

2.2 Overview of Air Pollution Policy Objectives

Road transport is widely recognised as a major contributor of adverse effects on the environment, with air pollution being an important global issue needing to be addressed, especially in urban areas. For this purpose, fairly strict standards and guidelines with respect to pollutant emissions have been adopted by the automotive industry, such that car manufacturers increasingly develop vehicles that avoid these emissions directly (e.g., electric and ultra-low emission vehicles). At the same time, pollutant emission threshold values have been adopted by governments and local authorities, which have been integrated in their high-level policy objectives, and with which any transport scheme is expected to comply. The present study focuses on the policy objectives of three pollutants, namely CO_2, NO_x and PM, which are to be used in the determination of the weighting factors in Equation (1) in relation to the importance of each one.

Governments and environmental bodies provide regulations for air pollution under various classifications. Limit values are the maximum acceptable concentrations that are provided for the protection of human health, while threshold values are defined as the levels at which the public must be informed of high concentrations of pollutants. Target values are the ones that should not be exceeded within a given time period, whereas critical levels refer to concentrations above which direct adverse effects may occur on trees or natural ecosystems, but not on humans.

As from the point of view of urban mobility and ITS the effects of pollutants on human health are of most importance, the limit values for the three pollutants tackled as set by a number of different countries are considered, and are shown in Table 2. It should be noted that limit values given in ppm (parts per million) have been converted to $\mu g/m^3$ based on the molecular weight of the respective pollutant. Also, as some limits are given as '24-hour' values with a certain number of allowed exceedances, 'annual' limit values have been devised for comparison purposes.

Table 2. Pollutant emission limit values for different countries ($\mu g/m^3$)

Country	CO_2	NO_x	PM
European Union[13]	810,000	40	40
USA[14]	810,000	99.74	12
Hong Kong[15]	810,000	40	50
Australia[16]	810,000	56.45	8
Thailand[17]	810,000	56.45	50

It can be seen from Table 2 that limit values for CO_2 are much higher than the other two pollutants. This is because CO_2 is a global pollutant rather than a local one, and therefore is not a direct concern to local air quality (and to human health) except when in very high concentrations. In fact, limit values for CO_2 only exist for indoor areas, and the only standard addressing CO_2 at the national level is the Kyoto Protocol[18], which foresees CO_2 percentage target reductions rather than actual limit values. However, given that common outdoor levels of CO_2 range between 350 ppm to 450 ppm, and that concentrations over 500 ppm usually suggest that a large combustion source is nearby[19], it is reasonable to adopt a value of 450 ppm (810,000 $\mu g/m^3$) as the equivalent CO_2 limit value for the purposes of this study.

3. Weighting Methodology

Having gathered information on high-level policy objectives for the three pollutants in question (PM, CO_2 and NO_x), the method for setting the weighting factors in the corresponding CONDUITS KPI is devised here. Focusing of the emission type weighting factors (w_{ET}), the first step is to consider the relative importance of the pollutants, which will give an indication of the order of difference between the weights. In this respect, if the severity of the effects on human health is

considered, PM should be weighted as most important, while CO_2 should be assigned the lowest weight. Specifically, intoxication of the blood is the most important adverse effect of CO_2, and this occurs almost exclusively in enclosed areas rather than outdoors. This order of difference is additionally confirmed by the limit values of the three pollutants, as outlined in Table 2; since PM generally has the strictest limit value, its weight in the KPI should be highest.

Nevertheless, there is a further consideration that needs to be made with respect to the weighting factors of the pollutants, and this is the fact that there is an order of magnitude of difference in the quantity of each pollutant emitted from traffic. For instance, Table 3 shows the total quantities of each of the three pollutants emitted from traffic on a road corridor in an urban area, as calculated using the AIRE emissions modelling tool in a previous related study by the authors[5], but in the same site as the one tackled in the present paper (Section 4). It is evident that CO_2 dominates both NO_x and PM in terms of quantity (which is expected given that CO_2 is naturally present in the atmosphere as part of the earth's carbon cycle), and also that NO_x dominates PM. In fact, it can be observed that the quantity of CO_2 is approximately 180.6 times higher than that of NO_x and approximately 4690.6 times higher than that of PM, and that the quantity of NO_x is approximately 25.97 times higher than that of PM.

Table 3. Pollutant quantities per vehicle type (mg)[5]

Vehicle type	CO_2	NO_x	PM
Bus	190,160,226	5,503,500	140,620
Articulated bus	356,682	8,302	301
Car	2,155,459,269	5,277,315	314,706
HGV	135,273,041	2,951,044	73,357
Total	**2,481,249,218**	**13,740,161**	**528,984**

As such, for the base scenario where the three pollutants are weighted as equally important to the decision maker, the NO_x weighting factor (w_{NOx}) should be approximately 180.6 times higher than the CO_2 weighting factor (w_{CO2}), and the PM weighting factor (w_{PM}) should be 4690.6 times greater than w_{CO2} and 25.97 times greater than w_{NOx}. Taking a base value of w_{CO2} = 100 for simplicity purposes, then the corresponding values for the other weighting factors will be w_{NOx} = 18060 and w_{PM} = 469 060; this is the base "unweighted" (UNW) scenario, where the weighting factors only balance out the order of magnitude differences between the pollutants.

Other weighting scenarios can be further defined on the basis of the pollutant emission limit values for the different countries, thus taking into account high-level policy objectives in that respect. These include the European Union (EU), USA, Hong Kong (HK), Australia (AUS) and Thailand (TH) scenarios and are shown in Table 4. It should be noted that while a base value of 100 is taken for w_{CO2}, this is not restrictive, and different values could be used, provided the values for w_{NOx} and w_{PM} are proportionally adjusted.

Table 4. Pollutant weighting scenarios

	Scenario name					
w_{ET}	UNW	EU	USA	HK	AUS	TH
w_{CO2}	100	100	100	100	100	100
w_{NOx}	18,060	2,025,000	812,111	2,025,000	1,434,898	1,434,898
w_{PM}	469,060	2,025,000	6,750,000	1,620,000	10,125,000	1,620,000

With respect to the weighting factors for the vehicle types (w_{VT}), these are set as the inverse of the Passenger Car Unit (PCU) equivalent value of each type, as defined in Transport for London's Traffic Modelling Guidelines[20]. It should be noted, though, that in the case of pollutant emissions, some vehicles, such as trams and bicycles, but also pedestrians, do not produce emissions, and are therefore assigned weighting factors of zero. The vehicle type weight values are shown in Table 5.

Table 5. PCU equivalents and vehicle type weighting values

Vehicle type	PCU [20]	w_{VT}
Car	1.0	1.0
Bus	2.0	0.5
Articulated bus	3.2	0.3125
HGV	2.3	0.4348

To test the weighting methodology, a real-world case study is employed, whereby an environmental impact assessment in terms of pollution of a proposed ITS scheme is carried out on using before- and after-data from a microscopic simulation model in the CONDUITS_DST software. This is described in the next section.

4. Application and Results

4.1 The CONDUITS_DST Software

Performance evaluation using the CONDUITS KPIs is facilitated by the CONDUITS_DST software, which

is a specialised tool working as an additional module to microsimulation software packages, such as PTV VISSIM. The tool selects and aggregates relevant output data from simulation models and uses it as input to the calculation of the KPIs. At the current stage the modules for traffic efficiency, pollution reduction and traffic safety evaluation have been developed, and a predictive social inclusion evaluation module is under development.

For the present study, the pollution reduction module of CONDUITS_DST is used. This combines the results estimated by the microsimulation and included in so-called "vehicle records" (i.e., files containing the simulation results per individual vehicle) with the output of an external emissions model (AIRE), and hence calculates the CONDUITS KPI for pollution reduction, as presented in Equation (1), according to different scenarios set up by the planner. The individual components of CONDUITS_DST and the flow of information between them are shown in Figure 1.

Valuable simulation results rely on the aggregation of many simulation runs with different seeds, and so CONDUITS_DST allows for more than a single mutation (seed) to be used to generate the input required by the KPI. The results generated by the tool enable easy comparison between different simulation runs and scenarios. Most importantly, CONDUITS_DST enables the conduct of policy-aware performance evaluation by providing an interface for setting the desired weighting factors. It is this interface that is used in the present study to enter the weighting scenarios defined in the previous section.

An important feature to note here is the transferability of CONDUITS_DST, as this is not bound to any particular microsimulation platform and can work equally well with available modelling tools providing vehicle logs, such as PTV VISSIM, PARAMICS, etc.

4.2 Application Case Study

The research described has been carried out in close cooperation with city authorities, with CONDUITS_DST being validated through an existing case study in the city of Brussels. Following the EU directive and the high interest of the Brussels-Capital Region to provide a better quality of life to its citizens, the city authority has been constantly seeking for ways to deliver a more efficient transport system on one hand, but a less polluting one on the other. One of the measures pursued involves increasing the share of public transport in the modal split, which requires making it more competitive compared to motorised private transport. With an already dense public transport network (70 public transport lines with a total length of more than 700 km), though, any improvements must be based on the existing system.

One of the means to introduce a more competitive public transport system is by reducing travel times. To achieve that, the Brussels-Capital Region has introduced a programme aiming at increasing the operational speed of most of its public transport lines. The programme focuses on reducing delays around signallised intersections by giving priority to public transport

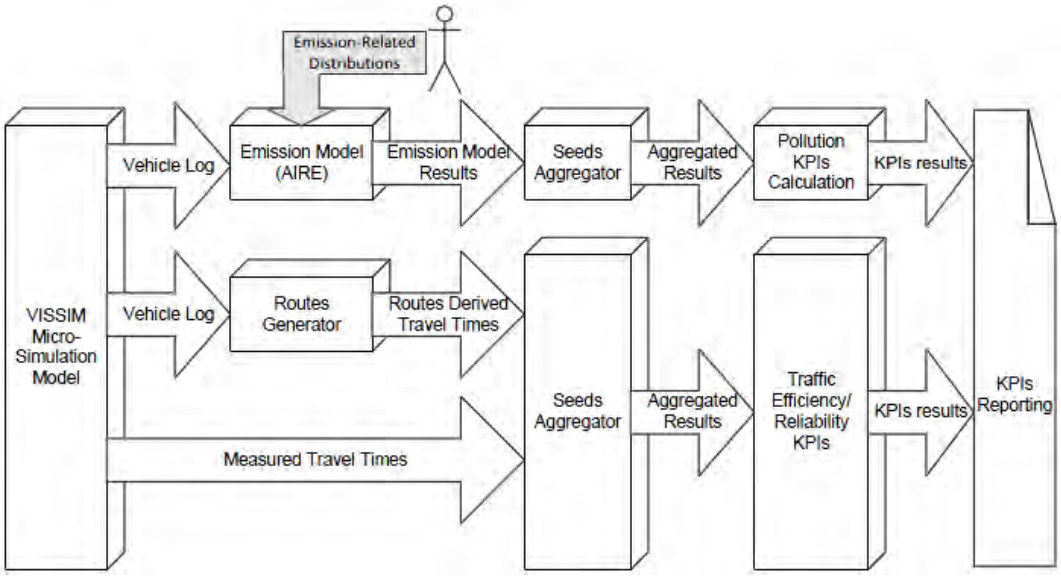

Figure 1. CONDUITS_DST structure and components[6].

vehicles over other traffic. This strategy promotes the attractiveness of public transport, both in the short- and the long-term, by offering lower travel times; however, it is also likely to have an undesired side-effect of increased pollution levels from traffic, especially in the short-term, due to increased waiting (idle) times and more stops and accelerations by private transport vehicles.

This side-effect is evaluated in the present study using CONDUITS_DST, in conjunction with relevant high-level policy objectives. More specifically, the prospective pollution impact of the introduction of priority signals along bus line no. 49 is analysed, taking into account the policy objectives as expressed by pollutant emission limit values. The study consists of four cases, representing the states before and after the implementation of the system in the morning and evening peak periods, respectively. From the planning phase of the signal control a calibrated VISSIM simulation network has been developed for all four cases (Figure 2).

4.3 Results

Several simulation runs are carried out over an evaluation period spanning three hours in the respective peak, extracting the necessary input data for the pollution KPI calculation in CONDUITS_DST. For each set of runs, the KPI calculation is carried out using each of the six pollutant weighting scenarios shown in Table 4, and the vehicle type weighting factors of Table 5.

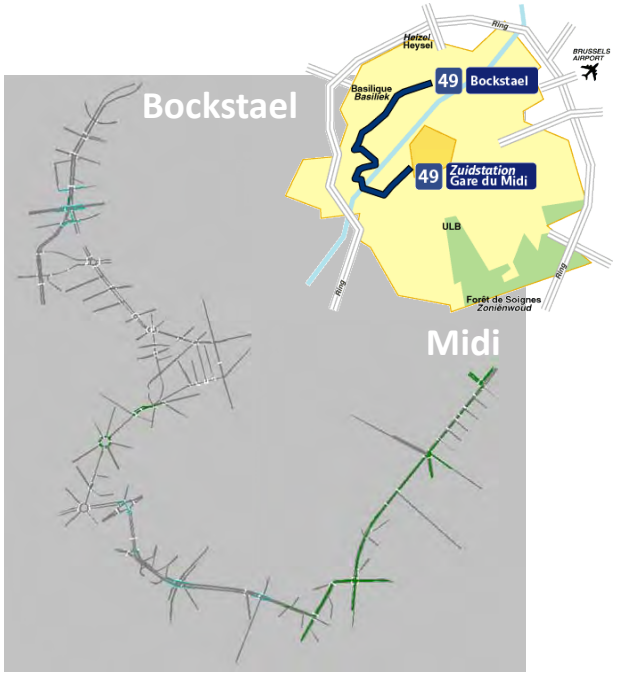

Figure 2. Line 49 and simulation network for the Brussels case study.

Table 6 shows the results of the KPI calculation for pollution in the four peak periods before and after the implementation of the priority measures, for each of the pollutant weighting scenarios, i.e., UNW, EU, USA, HK, AUS and TH. As can be immediately observed, the values for the after-case are higher than the before-case across all six weighting scenarios. Table 7 shows the corresponding percentage increase for each case and weighting scenario, where this finding is confirmed, as KPI increases of 6–9% and of 4–5.8% are observed for the morning and evening cases respectively. A brief comparison with other indicators of the simulation, such as the number of stops and delay times, both for private and public transport, confirm this outcome. The results, hence, show that, while public transport observes a decrease of 20–60% in the number of stops and an increase of the average speed of 3–6%, car drivers experience an increase of their journey time, along with an increase in the pollution levels.

Considering the percentage increase of the KPI between the different weighting scenarios, it can be clearly observed that the policy-aware KPI values (i.e., the ones based on the limit values of different countries) are higher than the respective increase in the UNW scenario (i.e. where pollutants are considered as equally important). This can be largely attributed to the fact that the PM and NO_x emissions are considered as more important by the authorities of the different countries and, as such, figure more prominently in their high-level policy objectives. In practical terms, this means that the foreseen "objective" 4–6% increase

Table 6. Pollution KPI values for each scenario (equivalent emissions units)

Scenario	UNW	EU	USA	HK	AUS	TH
Morning before	258.79	1373.36	368.93	1515.88	409.96	1299.00
Morning after	274.39	1498.49	397.98	1654.64	443.00	1416.88
Evening before	302.43	1562.24	420.99	1724.20	467.46	1478.00
Evening after	315.13	1647.12	441.48	1818.23	490.60	1558.09

Table 7. Percentage change in the pollution KPI values

Scenario	UNW	EU	USA	HK	AUS	TH
Morning before Morning after	+ 6.0%	+ 9.1%	+ 7.8%	+ 9.2%	+ 8.0%	+ 9.0%
Evening before Evening after	+ 4.0%	+ 5.4%	+ 4.8%	+ 5.4%	+ 5.0%	+ 5.4%

in pollution as a result of the implementation of the scheme may actually correspond to more severe increases from the point of view of decision makers.

A further observation that can be made is that four-digit KPI values are obtained for the EU, HK and TH weighting scenarios, while the USA and AUS ones are three-digit and closer to the UNW scenario values. This can be explained by the fact that the USA and Australia appear to have less strict legislation with regard to NO_x and PM emissions compared to the EU, Hong Kong and Thailand. Practically speaking, this means that the same ITS scheme or solution will have different perceived impact severity by decision makers in different countries as a result of the different high-level policy objectives. In other words, a scheme's adverse impacts may be acceptable in one city or country but unacceptable in another one, purely due to alignment or non-alignment with policy objectives respectively, which is exactly what the weights are supposed to capture.

5. Conclusions and Further Work

A method for policy-aware evaluation of urban mobility and ITS schemes was introduced in this paper, with the objective of being used in conjunction with the CONDUITS KPIs and the corresponding CONDUITS_DST software, in order to assist decision-making in smart cities. The method uses the pollutant emission limit values that are in effect in different countries' legislations to derive appropriate weighting factor values for three key pollutants, CO_2, NO_x and PM, in the calculation of the corresponding CONDUITS KPI for pollution from motor vehicle emissions. The results of the application on a real case study in the city of Brussels featuring the implementation of a system granting priority to public transport at signalised intersections showed that the method can not only capture the expected side-effect of the increase in pollution levels, but that it is also able to reflect policy objectives and deliver evaluation results in relation to their alignment with those.

From a decision maker's point of view, this policy-awareness is invaluable, as it provides the means to present results to non-expert audiences in a simple, fast and effective way. On the other hand, it should be acknowledged that through the allocation of weights in a manner ensuring full alignment with policy objectives, a certain degree of subjectivity is inevitably introduced in the results of the evaluation. In order to reduce this, hence, it could be appropriate to employ an expert-based methodological approach to fine-tune the weight values, such as the well-known Delphi method[21–22], which is based on a series of questionnaires with controlled feedback for the purpose of reaching a relatively narrow range of outcomes by comparing opinions in an iterative fashion.

While the present study has shed some light on the topic of policy-aware evaluation of the environmental impacts of mobility management and ITS schemes and solutions in smart cities, work in this direction continues. It is an essential next step to conduct more analyses and apply the method in different case studies. It is likely that a more thorough calibration of the weighting factors will be necessary, as the individualities of cities and regions will need to be considered, and so it is foreseen to develop an advanced calibration mechanism that planners can apply once to their specific settings so that they can then produce policy-aware evaluation results, tailored to their needs. It is also important to be able to systematically incorporate the views of experts in the evaluation procedure, and so work will continue along this direction in order to derive more robust weighting scenarios for the CONDUITS pollution KPI, which incorporate expert knowledge. Finally, it is foreseen to develop similar appropriate weighting methodologies for the other KPIs (traffic efficiency, traffic safety, social inclusion) and to incorporate them in CONDUITS_DST.

Conflict of Interest and Funding

No conflict of interest was reported by the authors.

Acknowledgements

The authors would like to thank Kapsch TrafficCom for sponsoring this work, as well as the Brussels-Capital Region for providing the necessary data for the conduct of the application case study.

References

1. Zavitsas K, Kaparias, I and Bell M G H, 2011, *Transport problems in cities*: *Deliverable No. 1.1*, CONDUITS, viewed November 3, 2016, <http://www.transport-research.info/sites/default/files/project/documents/20120402_173932_45110_D%201.1%20-%20Transport%20problems%20in%20cities%20-%20v3.pdf>
2. Kaparias I and Bell M G H, 2011, *Key Performance Indicators for traffic management and Intelligent Transport Systems: Deliverable No. 3.5*, CONDUITS, viewed No-

vember 6, 2016, <http://www.polisnetwork.eu/publicdocuments/download/516/document/d-3-5---key-performance-indicators-for-traffic-management-and-its-final.pdf>

3. Kaparias I, Eden N, Tsakarestos A, *et al*. 2012, Development and application of an evaluation framework for urban traffic management and Intelligent Transport Systems, *Transport Research Arena Europe 2012*, Athens, Greece.
4. Tsakarestos A, Nocera S, Kaparias I, *et al*. 2011, Performance evaluation of urban traffic management and ITS: the Rome case study, *SIDT National Conference and Scientific Seminar 2011*, Venice, Italy.
5. Eden N, Tsakarestos A, Kaparias I, *et al*. 2012, Using Key Performance Indicators for traffic management and Intelligent Transport Systems as a prediction tool, *19th ITS World Congress*, Vienna, Austria.
6. Eden N, Kaparias I, Tsakarestos A, *et al*. 2013, Using key performance indicators for multi-criteria traffic management strategic decisions, *9th ITS European Congress*, Dublin, Ireland.
7. Kaparias I, Liu P, Tsakarestos A, *et al*. 2015, Development and testing of a predictive traffic safety evaluation tool for road traffic management and ITS impact assessment, *International Scientific Conference on Mobility and Transport (Mobil.TUM 2015)*, Munich, Germany.
8. Cianfano M, Gentile G, Nussio F, *et al*. 2011, *Transport and mobility indicators based on traffic measures – Good Practices Guidebook*, CITEAIR II, viewed November 8, 2016, <http://www.citeair.eu/fileadmin/Deliverables_and_documents/Guidebook_Mobility_and_Exposure_Indicators_TEXT-_Final.pdf>
9. Cambridge Systematics Inc., PB Consult Inc. and System Metrics Group, 2005, *NCHRP Report 545: Analytical tools for asset management*, Transportation Research Board of the National Academies, viewed October 1, 2016, <http://www.lpcb.org/index.php/documents/road-management/rms-applications/11072-2005-usa-analytical-tools-for-asset-management/file>
10. Zhou P, Ang B W and Poh K L, 2006, Comparing aggregating methods for constructing the composite environmental index: an objective measure. *Ecological Economics*, vol.59(3), 305–311. https://doi.org/10.1016/j.ecolecon.2005.10.018.
11. European Commission, 2001, *White Paper — European transport policy for 2010: time to decide*, viewed November 10, 2016, <http://ec.europa.eu/transport/sites/transport/files/themes/strategies/doc/2001_white_paper/lb_com_2001_0370_en.pdf>
12. European Commission, 2011, *White Paper — Roadmap to a single European Transport Area: towards a competitive and resource efficient transport system*, viewed November 14, 2016, <https://sustainabledevelopment.un.org/content/dsd/csd/csd_pdfs/csd-19/learningcentre/presentations/May%204%20pm/3%20-%20Julius%20Langendorff%20-%20EU%20White%20Paper%20Single%20Zone.pdf>
13. European Commission, 2008, *Directive 2008/50/EC of the European Parliament and of the Council of 21 May 2008 on ambient air quality and cleaner air for Europe*, viewed November 11, 2016, <http://eur-lex.europa.eu/legal-content/en/ALL/?uri=CELEX:32008L0050>
14. US Environmental Protection Agency, 2015, *National Ambient Air Quality Standards (NAAQS)*, viewed November 13, 2016, <https://www.epa.gov/criteria-air-pollutants/naaqs-table>
15. Hong Kong Environmental Protection Department, 2015, *Hong Kong's Air Quality Objectives*, viewed November 13, 2016, <http://www.epd.gov.hk/epd/english/environmentinhk/air/air_quality_objectives/air_quality_objectives.html>
16. Australian Government, Department for the Environment, 2015, *Air Quality Standards*, viewed November 14, 2016, <https://www.environment.gov.au/protection/air-quality/air-quality-standards>
17. Thailand Ministry of Natural Resources and Environment, Pollution Control Department, 2015, *Air Quality and Noise Standards*, viewed November 14, 2016, <http://www.pcd.go.th/info_serv/en_reg_std_airsnd.htm>
18. United Nations Framework Convention on Climate Change, 2014, *Kyoto Protocol*, viewed October 31, 2016, <http://unfccc.int/kyoto_protocol/items/2830.php>
19. Minnesota Department of Health, 2014, *Carbon dioxide (CO_2): environmental health in Minnesota*, viewed October 29, 2016, <http://www.health.state.mn.us/divs/eh/indoorair/co2/>
20. Transport for London, 2010, *Traffic Modelling Guidelines: TfL Traffic Manager and network performance best practice*, version 3.0, viewed November 5, 2016, <http://content.tfl.gov.uk/traffic-modelling-guidelines.pdf>
21. Linstone HA and Turrof M, 1975, *The Delphi Method: Techniques and Applications*, Addison Wesley Publishing Company, 1975.
22. Nijkamp P, Rienstra S and Vleugel J, 1998, *Transportation Planning and the Future*, Wiley & Sons, Chichester, UK.

RESEARCH ARTICLE

Bayesian optimal sensor placement for modal identification of civil infrastructures

Costas Argyris[1], Costas Papadimitriou[*1] and Panagiotis Panetsos[2]

1. Department of Mechanical Engineering, University of Thessaly, Volos 38221, Greece
2. Capital Maintenance Department, Egnatia Odos S.A., Thermi 57001, Greece

Abstract: A Bayesian optimal experimental design (OED) method is proposed in this work for estimating the best locations of sensors in structures so that the measured data are most informative for estimating reliably the structural modes. The information contained in the data is measured by the Kullback-Leibler (K-L) divergence between the prior and posterior distribution of the model parameters taken in modal identification to be the modal coordinates. The optimal sensor placement that maximizes the expected K-L divergence is shown also to minimize the information entropy of the posterior distribution. Unidentifiability issues observed in existing formulations when the number of sensors is less than the number of identified modes, are resolved using a non-uniform prior in the Bayesian OED. An insightful analysis is presented that demonstrates the effect of the variances of Bayesian priors on the optimal design. For dense mesh finite element models, sensor clustering phenomena are avoided by integrating in the methodology spatially correlated prediction error models. A heuristic forward sequential sensor placement algorithm and a stochastic optimization algorithm are used to solve the optimization problem in the continuous physical domain of variation of the sensor locations. The theoretical developments and algorithms are applied for the optimal sensor placement design along the deck of a 537 m concrete bridge.

Keywords: Bayesian inference, Kullback-Leibler divergence, information entropy, structural dynamics

*Correspondence to: Costas Papadimitriou, Department of Mechanical Engineering, University of Thessaly, Volos 38221, Greece; Email: costasp@uth.gr

Received: October 10, 2016; **Accepted:** October 28, 2016; **Published Online:** December 30, 2016

Citation: Argyris C, Papadimitriou C, and Panetsos P, 2016, Bayesian optimal sensor placement for modal identification of civil infrastructures. *Journal of Smart Cities*, vol.2(2): 69–86. http://dx.doi.org/10.26789/JSC.2016.02.001.

1. Introduction

Experimental measurements from civil infrastructures, including buildings, bridges, offshore structures, wind turbines, and industrial facilities are often used to obtain the modes of these structures. The modes are useful in structural performance evaluation[1], finite element model updating[2-4], and model-based structural health monitoring[5,6]. A number of methodologies have been developed in the past to optimize the location of sensors in order to maximize the information contained in the measurements for identifying the structural modes. Among them, methods based on information theory are used to make rational decisions consistent with the information provided by the measurements. Non-information based methods have also been developed. A review of a number of non-information based methods can be found in a thesis by Li[7].

This work concentrates on optimal sensor placement design methods for modal identification based on information theory. In the past, notable contributions to the sensor placement problem for modal identification have been provided by the effective indepen-

dence (EFI) method[8] for uniaxial and triaxial sensors[9,10]. Information theory measures, based on scalar measures of the Fisher information matrix (FIM)[11,12] and on information entropy[13–15], proposed in the past for structural parameter estimation problems, have been extended to be used for modal identification[16] as well. An optimal sensor placement design for modal identification based on FIM was proposed by Kammer[17]. The information entropy measure for parameter estimation introduced by Papadimitriou *et al*.[13], was extended by Papadimitriou [18] to obtain useful expressions of the information entropy as a function of the number of sensors, and was applied to modal identification problems[16]. In particular, the information entropy measures the uncertainty in the posterior distribution of the model parameters to be identified. The posterior distribution is obtained from a Bayesian analysis that makes use of the prior distribution of the model parameters. Up to now, the effect of the prior distribution in the optimal design has not been adequately explored.

When applying the EFI and information entropy techniques to dense finite element models, the problem of sensor clustering is manifested. The source of the problem is the failure to take into account the redundant information provided from neighborhood sensor locations. The problem was adequately resolved using spatially correlated prediction error models in the Bayesian formulation to exclude redundant information from neighboring sensors[16]. Stephan[19] has also effectively tackled the issue of information redundancy between sensors by introducing a measure of information redundancy.

Optimization algorithms have also been proposed to find the optimal sensor locations. For structural parameter estimation problems multiple local/global optima make the solution of the optimization problem very challenging[20]. Heuristic algorithms such as the backward and forward sequential sensor placement (BSSP and FSSP) algorithms have been proposed to drastically reduce the computational effort[17,18]. The optimal sensor placement strategies based on the information entropy and FSSP was applied to bridge, towers, and timber structures for optimizing the location of uniaxial and triaxial sensors[21-23]. These algorithms are shown to be quite accurate. However, the use of the FSSP algorithm requires that identifiability issues are resolved for small number of sensors. Unidentifiability issues arise from the aforementioned methods for modal identification when the number of sensors placed in the structure is less than the number of identified modes. This is due to the fact that the FIM becomes singular. Yuen and Kuok[24] noted that introducing non-uniform priors in the Bayesian posterior used in the information entropy measures resolves the problem. For uniform priors, Papadimitriou and Lombaert[16] obtained reasonable sensor placement design by excluding the zero eigenvalues from the product of the eigenvalues of the FIM used for computing the determinant of the FIM that is required in information entropy formulations.

In this work we revisit the problem of sensor placement for modal identification. We formulate the optimal experimental design based on expected utility functions[25] and apply it to the case of optimizing the location of sensors for a real bridge. We use as utility function the relative entropy or, equivalently, the Kullback-Leibler divergence between the prior and the posterior distribution of model parameters[26]. For uniform or Gaussian priors and for models for which the output quantities of interest (QoI) depend linearly on the model parameters to be identified, as it is the case of modal identification, we demonstrate that the expected utility function is directly related to the minus of the information entropy of the parameters to be estimated plus a constant that does not depend on the sensor locations. Thus, the optimal design results in maximizing the expected log determinant of the sum of the FIM and the prior Hessian. As a result, with the aid of the information contained in the prior PDF of the model parameters, the combined matrix (FIM and prior Hessian) is non-singular for non-uniform priors and the optimal sensor placement problem can be carried out also for the case where the number of sensors is less than the number of modes.

A novelty in this work is to study the effect of Gaussian prior uncertainties on the optimal sensor design. For this, an insightful analytical expression is developed that shows the effect the prior uncertainties have on the optimal design. The importance of spatial correlation in the prediction error is also pointed out as the means of avoiding sensor clustering phenomena for finite element models used to simulate civil infrastructures.

Theoretical developments are demonstrated by designing the optimal locations of a number of sensors for a 537 m long concrete bridge using a dense finite element mesh of approximately 830,000 degrees of freedom (DOF). The optimization is formulated in the physical continuous space of the design variables.

This avoids the large discrete design space that arises from the extremely large number of possible nodal positions due to dense FE meshes. Multiple local optima are revealed that make the optimization problem very challenging. It is demonstrated that the computationally efficient heuristic FSSP algorithm provides accurate solutions when compared to stochastic algorithms such as the covariance matrix adaptation (CMA-ES)[27] able to estimate the global optimum with substantially higher computational cost. Useful results are obtained which help guide experimentalists as to how the proposed method can be used for designing the optimal sensor locations in practical applications. In particular, we demonstrate that designs are also obtained for the very important case of number of sensors which are less than the number of modes by using the information contained in the prior distribution. In particular, this is important in designing the location of the reference sensors in a multiple sensor configuration set up experiment conducted with limited number of reference and roving sensors in order to obtain the modal frequencies and reliably assemble the mode shapes from multiple setups. The effectiveness of the methodology is illustrated by designing the optimal location of two reference sensors (one transverse and one vertical) for the bridge. Finally, we draw attention to the sensor clustering issue and propose methods to avoid it and finally we show the effect of uncertainty in the prior distribution on the sensor placement designs.

2. Bayesian Parameter Estimation

The Bayesian framework for the estimation of the parameters of finite element models of structures based on experimental data is first outlined and the results are used in the optimal experimental design formulation presented in Section 3. Consider a model of a structural system and let $\underline{\theta} \in R^{N_\theta}$ be the vector of model parameters to be estimated using a set of measured data $\underline{y} \equiv \underline{y}(\underline{\delta}) \in R^{N_0}$ of output quantities that depend on experimental design variables $\underline{\delta}$, where N_0 is the number of sensors. Let $\underline{g}(\underline{\theta};\underline{\delta}) = A(\underline{\delta})\underline{\theta} \in R^{N_0}$ be the vector of the values of the output quantities predicted by a structural model for specific values of the parameter set $\underline{\theta}$, where it is assumed that there is a linear relationship between the output quantity of interest (QoI) and the parameter set $\underline{\theta}$ to be identified from the experiments, and $A(\underline{\delta}) \in R^{N_0 \times N_\theta}$ depends on the structure of the model and the experimental design variables $\underline{\delta}$. The design variables are related to the location of sensors placed in a structure. The location vector $\underline{\delta}$ contains the coordinates of the sensors with respect to a coordinate system.

The following prediction error equation is introduced to model the discrepancy between the measurements and the model predictions

$$\underline{y} = \underline{g}(\underline{\theta};\underline{\delta}) + \underline{e} = A(\underline{\delta})\underline{\theta} + \underline{e} \quad (1)$$

where $\underline{e}$ is the additive prediction error term due to model and measurement error. The prediction error $\underline{e}$ is usually modeled as a Gaussian vector, whose mean value is equal to zero and its covariance is equal to $\Sigma(\underline{\delta};\underline{\sigma}) \in R^{N_0 \times N_0}$, where $\underline{\sigma}$ contains the parameters that define the correlation structure $\Sigma(\underline{\delta};\underline{\sigma})$ of the prediction error. Applying the Bayesian theorem[2], the posterior probability density function (PDF) of the model parameter set $\underline{\theta}$, given the measured data $\underline{y}$, takes the form

$$p(\underline{\theta} \mid \underline{y},\underline{\sigma},\underline{\delta}) = c\frac{1}{(2\pi)^{N_0/2}\left[\det \Sigma(\underline{\delta};\underline{\sigma})\right]^{1/2}} \exp\left[-\frac{1}{2}J(\underline{\theta};\underline{y},\underline{\sigma},\underline{\delta})\right] \pi(\underline{\theta}) \quad (2)$$

where

$$J(\underline{\theta};\underline{y},\underline{\sigma},\underline{\delta}) = [\underline{y} - A(\underline{\delta})\underline{\theta}]^T \Sigma^{-1}(\underline{\delta};\underline{\sigma})[\underline{y} - A(\underline{\delta})\underline{\theta}] \quad (3)$$

quantifies the discrepancy between the measured and model predicted quantities, $\pi(\underline{\theta})$ is the prior distribution for $\underline{\theta}$, and c is a normalization constant guaranteeing that the posterior PDF integrates to one.

Due to the linear relationship between the output QoI and the model parameters, the function $J(\underline{\theta};\underline{y},\underline{\sigma},\underline{\delta})$ is quadratic in $\underline{\theta}$. Assuming a uniform prior with wide enough bounds or a Gaussian prior, the posterior PDF for the model parameters $\underline{\theta}$ is Gaussian, denoted by $N(\underline{\theta};\underline{\hat{\theta}},C)$, where $\underline{\hat{\theta}} \equiv \underline{\theta}(\underline{y};\underline{\sigma},\underline{\delta})$ is the most probable value obtained by minimizing the function $-\ln p(\underline{\theta} \mid \underline{y},\underline{\sigma},\underline{\delta})$, *i.e.*,

$$\underline{\hat{\theta}}(\underline{y};\underline{\sigma},\underline{\delta}) = \arg\min_{\underline{\theta}}[J(\underline{\theta};\underline{y},\underline{\sigma},\underline{\delta}) - \ln \pi(\underline{\theta})] \quad (4)$$

and the covariance matrix $C = C(\underline{\hat{\theta}};\underline{y},\underline{\sigma},\underline{\delta})$ equals to the inverse of the Hessian of $-\ln p(\underline{\theta} \mid \underline{y},\underline{\sigma},\underline{\delta})$, *i.e.*,

$$C^{-1}(\underline{\theta};\underline{y},\underline{\sigma},\underline{\delta}) = \underline{\nabla}_{\theta}\underline{\nabla}_{\theta}^{T}[-\ln p(\underline{\theta}\,|\,\underline{y},\underline{\sigma},\underline{\delta})] = Q_L(\underline{\delta},\underline{\sigma}) + Q_{\pi} \tag{5}$$

evaluated at the most probable value $\underline{\hat{\theta}}(\underline{y};\underline{\sigma},\underline{\delta})$, where $Q_L(\underline{\delta},\underline{\sigma})$ is the FIM obtained from

$$Q_L(\underline{\delta},\underline{\sigma}) = \frac{1}{2}\underline{\nabla}_{\theta}\underline{\nabla}_{\theta}^{T} J(\underline{\theta};\underline{y},\underline{\sigma},\underline{\delta}) = A^{T}(\underline{\delta})\Sigma^{-1}(\underline{\delta};\underline{\sigma})A(\underline{\delta}) \tag{6}$$

to be independent of $\underline{\theta}$ and the experimental values $\underline{y}$, and $Q_{\pi}(\underline{\theta}) = \underline{\nabla}_{\theta}\underline{\nabla}_{\theta}^{T}[-\ln \pi(\underline{\theta})]$ is the zero matrix $Q_{\pi} = 0$ for uniform prior and the constant matrix $Q_{\pi} = S^{-1}$ for a Gaussian prior PDF with covariance matrix S. The covariance matrix C of the Gaussian posterior PDF does not depend on the values of the parameters $\underline{\theta}$ and the experimental data $\underline{y}$. The dependence on the experimental design variables $\underline{\delta}$ comes from the information matrix $Q_L(\underline{\delta},\underline{\sigma})$.

3. Bayesian Optimal Experimental Design

3.1 Expected Utility Function

The expected utility function has been introduced by Lindley[25] to measure the information contained in the experimental data for estimating the parameters of the model. The expected utility function has the form

$$U(\underline{\delta}) = \int_{\Sigma}\int_{\Upsilon}\int_{\Theta} u(\underline{\delta};\underline{\theta},\underline{y},\underline{\sigma})\; p(\underline{\theta},\underline{y},\underline{\sigma}\,|\,\underline{\delta})\; d\underline{\theta}\; d\underline{y}\; d\underline{\sigma} \tag{7}$$

where $u(\underline{\delta};\underline{\theta},\underline{y},\underline{\sigma})$ is the utility function given a particular value of the model parameter set $\underline{\theta}$, the outcome $\underline{y}$ from the experiment, and the parameter set $\underline{\sigma}$, $p(\underline{\theta},\underline{y},\underline{\sigma}\,|\,\underline{\delta}) = p(\underline{\theta}\,|\,\underline{y},\underline{\sigma},\underline{\delta})\; p(\underline{y}\,|\,\underline{\sigma},\underline{\delta})\; p(\underline{\sigma}\,|\,\underline{\delta})$, $p(\underline{\theta}\,|\,\underline{y},\underline{\sigma},\underline{\delta})$ is the posterior uncertainty in the model parameters given the outcome $\underline{y}$, $p(\underline{y}\,|\,\underline{\sigma},\underline{\delta})$ is the uncertainty in the data, and $p(\underline{\sigma}\,|\,\underline{\delta}) = \pi(\underline{\sigma})$ quantifies the prior uncertainty in the parameter set $\underline{\sigma}$. Herein, the expected utility function in (7) has been extended to include the uncertainties in the model prediction error parameters $\underline{\sigma}$ by taking the expectation over the parameter space $\underline{\sigma}$ as well.

Based on information theory, the utility function can be chosen to be the relative entropy or the Kullback-Leibler divergence[25,26]

$$u(\underline{\delta};\underline{\theta},\underline{y},\underline{\sigma}) = p(\underline{\theta}\,|\,\underline{y},\underline{\sigma},\underline{\delta})\; \ln \frac{p(\underline{\theta}\,|\,\underline{y},\underline{\sigma},\underline{\delta})}{\pi(\underline{\theta})} \tag{8}$$

between the prior and posterior PDF of the model parameters $\underline{\theta}$ given an outcome $\underline{y}$ obtained from an experimental design $\underline{\delta}$. Substituting (8) into (7), one has that the expected utility function is an average of the K-L divergence over all possible values of the model parameters $\underline{\theta}$ as they are inferred from the data, all the possible outcomes $\underline{y}$ of the experiment, and all possible values of the model prediction error parameters $\underline{\sigma}$. For Gaussian posterior PDF in $\underline{\theta}$ that does not depend on the data $\underline{y}$, the inner double integral in the expected utility function simplifies considerably[28] and the expected utility function takes the form

$$U(\underline{\delta}) = -\int H(\underline{\delta},\underline{\sigma})\; \pi(\underline{\sigma})\; d\underline{\sigma} - c \tag{9}$$

where

$$H(\underline{\delta},\underline{\sigma}) = \frac{1}{2}N_{\theta}[\ln(2\pi)+1] - \frac{1}{2}\ln\det[Q_L(\underline{\delta};\underline{\sigma}) + S^{-1}] \tag{10}$$

is the information entropy of the model parameters $\underline{\theta}$ given $\underline{\sigma}$, while c is a quantity that does not depend on the design variables $\underline{\delta}$ so that it can be treated as constant. This integral in the right-hand-side of (9) represents the robust measure of the information entropy over all possible values of the prediction error parameters quantified by the prior PDF $\pi(\underline{\sigma})$. For a small number (one or two) of parameters in $\underline{\sigma}$, the integral can be carried out using a numerical integration algorithm. For the sake of simplicity, in this work the values of $\underline{\sigma}$ are assumed known (deterministic). The utility function then takes the form

$$U(\underline{\delta}) = -H(\underline{\delta},\underline{\sigma}) - c \tag{11}$$

It can be seen that the expected relative information or expected K-L divergence has a direct connection to the robust information entropy proposed by Papadimitriou *et al.*[13] and extended by Yuen and Kuok[24] for non-uniform distributions.

3.2 Optimal Designs

The optimal experimental design problem is formulated as finding the values $\underline{\delta}_{opt}$ of the design variables

$\underline{\delta}$ that maximize the utility function $U(\underline{\delta})$ or, equivalently, minimize the information entropy $H(\underline{\delta},\underline{\sigma})$, *i.e.*,

$$\underline{\delta}_{opt} = \arg\max_{\underline{\delta}} U(\underline{\delta}) = \arg\min_{\underline{\delta}} H(\underline{\delta},\underline{\sigma}) \qquad (12)$$

Optimal experimental design problems involving the design of the position of sensors often result in multiple local and global solutions. This will be also evident in the results presented in the application section. Also the gradient of the objective function with respect to the design variables in most cases of practical interest cannot be evaluated analytically. To avoid premature convergence to a local optimum and the evaluation of sensitivities of the utility function with respect to the design variables, stochastic optimization algorithms can be used to find the optimum. Herein the CMA-ES algorithm[27] is used for solving the optimization problem, requiring only evaluation of the objective function at different values of the design variables. For this, the problem is formulated as a continuous optimization problem where the design variables are related to the coordinates of the sensors along the physical domain of the structure. To account, however, of curved and disconnected one-dimensional or two-dimensional domains, as well as to take into account the different types of sensors (vertical or transverse) that can be placed along the curved domain, a mapping technique can be used to map the physical design space into a regular one-dimensional parent domain. The optimization is then conveniently carried out in the parent domain. The method will be illustrated for one-dimensional curved domains in the application section.

Heuristic algorithms have also been proposed to provide sub-optimal solutions. Notable are the forward and backward sequential sensor placement algorithms (FSSP and BSSP) in which the optimization is carried out sequentially. In the FSSP algorithm[18] the optimization is carried out sequentially for a single sensor, say the $i+1$ sensor, given that i sensors have already been placed in their optimal locations. This procedure is repeated for $i=1,\cdots,N_0$, where N_0 is the total number of sensors to be placed in the structure. The heuristic algorithms have been shown to be effective and provided for several problems near optimal solutions[16]. The FSSP algorithm is used here for investigating its effectiveness for the optimal sensor placement problem for modal identification.

3.3 Properties of the Expected Relative Entropy or K-L Divergence

The robust information entropy involved in the expected utility function in (9) has exactly the same structure as the information entropy derived asymptotically by Papadimitriou[18] for nonlinear models. Based on the structure of the information entropy measure in (10) it was shown analytically that the information entropy follows certain properties[16,18]. Using the relationship (9) or (11) between the expected K-L divergence and the information entropy, one can easily extend the validity of these properties to the expected utility function. Specifically, following Papadimitriou's paper[18], one can confirm that the expected utility function for a given number of sensors placed in the structure increases when one or more additional sensors are placed in the structure. As a result, the maximum value of the expected utility function attained for a certain number of sensors is a non-decreasing function of the number of sensors. Thus the selection of the optimal number of sensors is based only on the level of the information that one can afford loosing when stops placing additional sensors in the structure. In addition, spatially correlated prediction error models avoid the problem of the redundant information that is usually provided by neighborhood sensors[16]. This is true when the distance of the sensors is less than a characteristic length of the contributing mode. In this case the spatial correlation length in spatially correlated prediction error models should be selected based on the characteristic length of the highest contributing mode. Spatially uncorrelated prediction error models fail to properly consider the redundant information and should be avoided since otherwise they result in sensor clustering.

4. Optimal Sensor Placement for Modal Identification

4.1 Formulation for Modal Identification

The optimal experimental design methodology is next implemented in structural dynamics for optimally placing the sensors in the structure for modal identification. Considering a linear finite element model of a structure, the equations of motion are given by

$$M\ddot{\underline{u}} + \tilde{C}\dot{\underline{u}} + K\underline{u} = \underline{f} \qquad (13)$$

where M, $\tilde{C}$ and $M \in \mathrm{R}^{n\times n}$ are the mass, damping and stiffness matrices, respectively, $\underline{u} \in R^n$ is the di-

splacement vector and $\underline{f}$ is the forcing vector. Using modal analysis and assuming classically damped modes, the response displacement and acceleration vectors are given by $\underline{u} = \Phi\underline{\xi}$ and $\underline{\ddot{u}} = \Phi\underline{\ddot{\xi}}$, respectively, where $\Phi = [\underline{\phi}_1, \cdots, \underline{\phi}_m] \in \mathrm{R}^{n\times m}$ is the matrix of mode shapes involving m contributing modes ($m \leqslant n$) that can be obtained by solving the eigenvalue problem $K\Phi = \Lambda M\Phi$, Λ is the diagonal matrix of eigenvalues, $\underline{\xi} = [\xi_1, \cdots, \xi_m]^T \in R^m$ is the vector of modal coordinates satisfying

$$\ddot{\xi}_r + 2\zeta_r\omega_r\dot{\xi}_r + \omega_r^2\xi_r = \underline{\phi}_r^T\underline{f} \tag{14}$$

$r = 1, \cdots, m$, and ζ_r is the modal damping ratio. The strain vector is given by a similar expression $\underline{\varepsilon} = E\underline{\xi}$, where E depends through the finite element modeling on the elements in the mode shape matrix Φ.

The problem of estimating the modal coordinate vector $\underline{\xi}$ or $\underline{\ddot{\xi}}$ using displacement/strain or acceleration measurements is investigated in this work. The modal coordinates $\underline{\xi}$ or $\underline{\ddot{\xi}}$ contain the modal properties (modal frequencies, modal damping ratios, participation factors). The objective in modal identification is to place sensors (displacement, acceleration and/or strain sensors) so that the information contained in the measured data is sufficient to estimate the modal coordinate vectors $\underline{\xi}$ or $\underline{\ddot{\xi}}$, depending on the sensor type used. Introducing the parameter set $\underline{\theta}$ to be either $\underline{\xi}$ or $\underline{\ddot{\xi}}$ and denoting by $\underline{g}(\underline{\theta};\underline{\delta}) \in R^{N_0}$ the response quantity that is measured by the sensors, one has the following equation between the modal model predictions and the parameter set $\underline{\theta}$

$$\underline{g}(\underline{\theta};\underline{\delta}) = \Phi(\underline{\delta})\underline{\theta} = L(\underline{\delta})\Phi\underline{\theta} \tag{15}$$

where the matrix $L(\underline{\delta}) \in R^{N_0\times n}$ is the observation matrix and maps the n model DOF to the N_0 measured positions. The matrix $L(\underline{\delta})$ depends on the location vector $\underline{\delta}$ defining the locations of the sensors in the structure. If the measured positions coincide with the DOF of the model then the matrix $L(\underline{\delta})$ is comprised of zeros and ones. For the general case for which the measured locations do not coincide with the DOF of the FE model, the matrix $L(\underline{\delta})$ depends on the interpolation scheme used to obtain the response within a finite element in terms of the finite element nodal responses. The above formulation allows sensors placed in any point in the structure, not only at nodal points. Also it gives the flexibility to covert the optimization problem for estimating the design variables to a continuous optimization problem over the physical domain of the structure. For strain measurements the aforementioned analysis is the same provided that the mode shape matrix Φ is replaced by the matrix E.

The model equation in (15) is the same as the one used in (1) so that the expected utility function (9) or (11) applies with the FIM given by

$$Q_L(\underline{\delta};\underline{\sigma}) = [L(\underline{\delta})\Phi]^T\Sigma^{-1}(\underline{\delta};\underline{\sigma})[L(\underline{\delta})\Phi] \tag{16}$$

in terms of the mode shape components at the measured locations.

Based on the form (16), and using the dimensions of the matrices $[L(\underline{\delta})\Phi]^T \in R^{m\times N_0}$, $\Sigma^{-1}(\underline{\delta};\underline{\sigma}) \in R^{N_0\times N_0}$ and $L(\underline{\delta})\Phi \in R^{N_0\times m}$ in (16), a non-singular FIM matrix $Q_L(\underline{\delta};\underline{\sigma})$ is obtained only if the number of sensors N_0 is at least equal to the number of contributing modes m ($N_0 \geqslant m$). For $N_0 < m$, the matrix $Q_L(\underline{\delta};\underline{\sigma})$ in (15) is by construction singular and for uniform prior PDF the determinant of the combined matrix $Q_L(\underline{\delta};\underline{\sigma}) + S^{-1}$ in (10) will be zero for any sensor configuration. Thus, for $N_0 < m$ the optimal sensor location problem cannot be performed for uniform prior PDF. This means that the information content in the measured data and the prior is not sufficient to estimate all the parameters simultaneously.

The Bayesian optimal experimental design formulation yields a nonsingular matrix for $N_0 < m$ only if the prior is non-uniform distribution. The non-uniform prior, say Gaussian, yields a Hessian matrix S^{-1} that is added to the Fisher information matrix $Q_L(\underline{\delta};\underline{\sigma})$ and makes the combined matrix $Q_L(\underline{\delta};\underline{\sigma}) + S^{-1}$ non-singular. The information matrix $Q_L(\underline{\delta};\underline{\sigma})$ in (16) has exactly the same form as the one proposed by Yuen[4] for designing the optimal sensor locations using the EFI algorithm. The difference of the present Bayesian formulation to the EFI algorithm is in the use of the prior information for the model parameters which permits the design of optimal sensor locations for the case of number of sensors which is less than the number of modes. The contribution from the prior is the result of the application of the Bayesian optimal

experimental design proposed herein based on optimizing the expected K-L divergence. Alternatively, Yuen and Kuok[24] have also proposed a non-uniform prior on the information entropy measure in order to solve this unidentifiability problem. For uniform prior and unidentifiable case, Papadimitriou and Lombaert[16] proposed the sum of the log of the non-zero eigenvalues in the FIM to be maximized instead of the sum of the log of all eigenvalues. Herein these results are generalized to incorporate prior uncertainty in the parameter estimates. This procedure allows to systematically place the sensors optimally in the structure even for the unidentifiable case that arises for a small number of sensors.

4.2 Effect of Prior Uncertainty

Next a diagonal covariance $S = diag(s_1^2, \cdots, s_m^2)$ for the Gaussian prior is assumed and the effect of the values of the variances is examined. These variances control the prior uncertainty in the values of the model parameters. A theoretical result is provided that shows the effect of the assigned prior uncertainties on the optimal design.

For simplicity, the case of optimally placing one sensor is considered first and then generalized for the multiple sensor case. In the case of a single sensor, the FIM reduces to the form $Q_L(\underline{\delta};\underline{\sigma}) = \sigma^{-2}\underline{\varphi}_i\underline{\varphi}_i^T$, where $\underline{\varphi}_i = [\Phi_{i1}, \Phi_{i2}, \cdots, \Phi_{im}]^T$ is a vector of dimension m that consists of the values of each mode shape at the sensor location denoted here as i. Note that for one sensor the prediction error covariance $\Sigma(\underline{\delta};\underline{\sigma})$ is scalar with $\Sigma(\underline{\delta};\underline{\sigma}) = \sigma^2$. Using the following known result for a square matrix B and two vectors $\underline{u}$ and $\underline{v}$

$$det(\underline{u}\underline{v}^T + B) = (1 + \underline{v}^T B^{-1}\underline{u})\, det(\mathrm{B}) \tag{17}$$

the $\det Q \equiv \det[Q_L(\underline{\delta};\underline{\sigma}) + S^{-1}]$ in (9) takes the form

$$\begin{aligned}\det[Q] &= det[\sigma^{-2}\underline{\varphi}_i\underline{\varphi}_i^T + S^{-1}] = \\ &[1 + \sigma^{-2}\underline{\varphi}_i^T S\underline{\varphi}_i]\, det(S^{-1}) = \\ &[1 + \sigma^{-2}\sum_{k=1}^{m} s_k^2\Phi_{ik}^2]\, det(S^{-1})\end{aligned} \tag{18}$$

Note that the variance s_k^2 of the k-th parameter (modal coordinate) weights the contribution in the sum of the value of the k-th mode shape at the sensor location. The higher the value of the variance s_k^2, the higher the contribution of the k-th mode shape on the $\det[Q]$. So it is evident that the optimal design will give preference to the modes that have higher prior uncertainty, *i.e.*, higher s_k^2 values.

Next we complete the proof for the general case of arbitrary number of N_0 sensors. For this, we use the following known result

$$\begin{aligned}&det(UWV^T + B) = \\ &\quad det(W^{-1} + V^T B^{-1}U)\, det(W)\, det(B)\end{aligned} \tag{19}$$

Setting for simplicity $\Psi = L(\underline{\delta})\Phi$ and using (16) and (10), the $\det Q = \det[Q_L(\underline{\delta};\underline{\sigma}) + S^{-1}]$ takes the form

$$\begin{aligned}\det[Q] &= \det[\Psi^T\Sigma^{-1}(\underline{\delta};\underline{\sigma})\Psi + S^{-1}] \\ &= \det[\Sigma(\underline{\delta};\underline{\sigma}) + \Psi S\Psi^T]\det[S^{-1}]\det[\Sigma^{-1}(\underline{\delta};\underline{\sigma})] \\ &= \det\left[\Sigma(\underline{\delta};\underline{\sigma}) + \sum_{k=1}^{m} s_k^2\psi_k(\underline{\delta})\psi_k^T(\underline{\delta})\right] \\ &\quad \det[S^{-1}]\det[\Sigma^{-1}(\underline{\delta};\underline{\sigma})] \\ &= \det\left[\Sigma(\underline{\delta};\underline{\sigma}) + \sum_{k=1}^{m} s_k^2 \,\|\psi_k(\underline{\delta})\|^2\, \tilde{\psi}_k(\underline{\delta})\tilde{\psi}_k^T(\underline{\delta})\right] \\ &\quad \det[S^{-1}]\det[\Sigma^{-1}(\underline{\delta};\underline{\sigma})]\end{aligned} \tag{20}$$

where $\psi_k(\underline{\delta})$ is the k-th mode shape evaluated at the sensor locations, $\tilde{\psi}_k(\underline{\delta})$ is the unit-normalized mode shape, $\|\psi_k(\underline{\delta})\|^2$ is the Euclidean norm square of the mode shape.

Equation (18) is a special case of equation (20) when only one sensor is used and Ψ becomes a row vector and its columns become scalars. In the multiple sensor case we are dealing with a sum of rank-one matrices over the model parameters, where each rank-one matrix $\psi_k(\underline{\delta})\psi_k^T(\underline{\delta})$ is formed from the k-th mode shape $\psi_k(\underline{\delta})$, weighted by the correspondding prior variance s_k^2 of that mode. So we see again that, similarly to the one sensor case, the Gaussian prior variance s_k^2 acts as weighting factor, this time by giving greater weight to the matrix $\psi_k(\underline{\delta})\psi_k^T(\underline{\delta})$ related to the k-th mode. The variance s_k^2 of the k-th mode weights the contribution in the sum of the value of the k-th rank-one matrix formed from the k-th mode shape that is evaluated at the sensor locations. The higher the value of the variance s_k^2, the higher the contribution of the rank-one matrix of the k-th mode shape on the $\det[Q]$. So the optimal de-

sign of sensor locations again gives preference to the modes that are assigned by a user to have higher prior uncertainty.

It should be noted that the idea of favoring one or more modes in the design of the optimal sensor configuration by appropriately selecting the prior variances can be useful in model updating and damage detection applications. Specifically, in damage detection and localization the proposed optimal sensor placement design can be used to increase the information about the damage location and size contained in the measured data by favoring, for example, local modes known to be more sensitive to local damage. To avoid reducing the robustness of the proposed optimal sensor placement algorithm for identifying the least favored modes, one may choose to optimally allocate a fraction of the available sensors in an effort to favor a small number of the contributing modes, ensuring that the optimal placement of the rest of the sensors maintain adequate levels of robustness.

5. Application

The proposed methodology is used to optimize the location of acceleration sensors placed at the deck level of the Metsovo Bridge. Numerical results are shown for up to 30 sensors for the spatially uncorrelated and spatially correlated prediction error models. The effect of the spatial correlation as well as the effect of the selection of the uncertainty in the prior distribution on the optimal designs is also investigated. Finally, the optimal design of a small number of reference sensors to be used as common sensors in multiple configuration setups is illustrated.

5.1 Bridge Description and FE Model

The Metsovo bridge of Egnatia Motorway, schematically shown in Figure 1, is crossing the deep ravine of Metsovitikos river, 150 m over the riverbed. This is the highest bridge of the Egnatia Motorway, with the height of the tallest pier equal to 110 m. The total length of the bridge is 537 m. The bridge has 4 spans of length 44.78 m, 117.87 m, 235 m, 140 m and 3 piers of which M1 (45 m) supports the boxbeam superstructure through pot bearings (movable in both horizontal directions), while M2 (110 m) and M3 (35 m) piers connect monolithically to the structure.

A detailed FE model of the bridge is created using 3-dimensional tetrahedron quadratic Lagrange finite elements. The mesh is chosen to accurately predict the lowest twenty modal frequencies and mode shapes of the bridge. The model also considers the interaction with soil by modeling the soil stiffness with solid blocks surrounding the piers and abutments. The FE model has 830,000 DOF. The size of the elements in the mesh is controlled by the thickness of the deck and piers box-like cross-sections. The typical element length is of the order of the thickness of the deck cross-section. The complex 3D geometry of the bridge was designed in SolidWorks and the FE model was created and solved in COMSOL Multiphysics by importing the 3D geometry from SolidWorks. The modulus of elasticity for the concrete was taken from design considerations to be 37×10^9 Pa and 34×10^9 Pa for the deck and the piers, respectively. The modulus of elasticity for the solid blocks was taken to be 9×10^9 Pa. The stiffness and mass matrices of the finite element model are used to obtain the mass normalized mode shapes to be used in the optimal sensor place ment methodology.

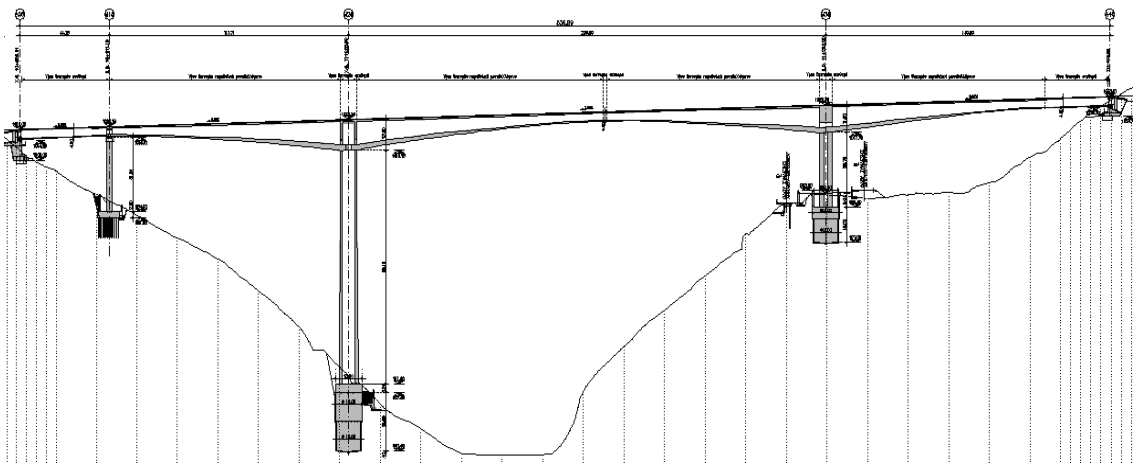

Figure 1. Longitudinal view of the Metsovo Bridge

5.2 Optimal Sensor Placement

The purpose of the OED is to optimally locate a number of acceleration sensors such that one gets the most informative data for identifying the lowest 10 modes. Using the FE model, the lowest 10 mode shapes needed in the design of the optimal sensor locations were computed and stored. These modes consist of 5 transverse modes, with mode shapes that deform the bridge and deck in the transverse direction, and 5 vertical modes mode, with mode shapes that bend the deck in the vertical direction. The transverse mode numbers are $\{1,2,4,6,8\}$, while the bending mode number are $\{3,5,7,9,10\}$. The optimal locations of sensors are obtained by maximizing the expected utility function or minimizing the information entropy. Herein, results will be presented in terms of the information entropy measure. It should be noted that in our case the number of parameters (modal coordinates) is $N_\theta = m = 10$.

5.2.1 Continuous Optimization in Parent Domain

Due to the fact that measurements on the bridge deck have to be taken without traffic interruptions, the sensors in the structure are only allowed to be placed along the pedestrian sidewalks (left and right). For demonstration purposes, in this study it will be assumed that sensors are placed along the one sidewalk marked in Figure 2 with red line. The line along the sidewalk over which sensors can be placed is a curved one and in order to perform the optimization problem along the curved line we develop a mapping of the curved line in a much simpler parent domain of a straight line. Each point in the physical curved line is mapped to a point in the straight parent line. To introduce such a mapping one can follow concepts developed in finite element analysis to map an arbitrary one-dimensional element in space in a parent element of specified length. It should be noted that the curved one-dimensional domains (red line) in Figure 2 consists of the straight elements that are the vertices of the neighbor tetrahedral finite elements used to model the bridge. So these straight vertices are mapped in the sequence that are encountered from left to the right edge of the bridge to a parent element so that the left corner of the red curve is mapped to the parent location 0, while the right corner of the red curve is mapped to the parent location 1. Specifically, the 0 m to 537 m curved line along the deck is mapped to the parent domain from 0 to 1.

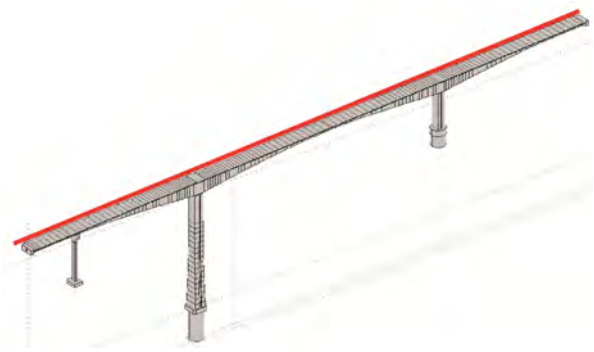

Figure 2. Optimization along pedestrian walkway of the deck

To account for the different type of sensors that can be placed on the physical structures, in our case sensors measuring in the vertical and the transverse directions, the physical curved line with transverse sensors placed on it is mapped to a parent element from 0 to 1, while the physical curved line with vertical sensors placed on it is mapped to a parent element from 1 to 2. In this way one can efficiently handle the two types of transverse and vertical sensors without the need to distinguish them during the optimization. The optimization is performed in the parent domain with the design variables, indicating the location of the sensors in the parent domain, to vary from 0 to 2. A design value inside the parent domain [0,1] corresponds to a transverse sensor which is mapped through the aforementioned mapping to a point on the physical domain (red curve) in Figure 2. Similarly, a design value inside the parent domain [1,2] corresponds to a vertical sensor which is mapped to a point on the physical domain (red curve) in Figure 2.

The mode shape value at a point in the parent domain is obtained by the mode shape value at the corresponding point in the physical domain. Consider the mapping of points from 0 to 1 in the parent domain to the physical domain. Since the mapped point in the physical domain might not correspond to a node of the finite element model, the mode shape value is obtained by interpolation using the mode shape values at the two neighboring nodes of that point in the transverse direction. A similar procedure is used for points between 1 and 2 in the parent domain to find the mode shape component in the vertical direction.

Using this mapping strategy the optimization is performed in a more sophisticated way than what was used in the past. Instead of performing multiple optimizations for one sensor at a time which is predetermined to be either a transverse or vertical sensor, now

it is allowed to optimize for several sensors simultaneously on the bridge pedestrian sideway, without predetermining the types of the sensors. Instead, it is left for the optimization to decide which of the sensors will be transverse and which will be vertical, depending on what region they lie in the parent domain.

So the optimization proceeds as follows. The design vector $\underline{\delta}$ is a vector with as many elements as the number of uniaxial sensors. Each element of this vector describes both the location and the type (transverse or vertical) of a sensor. Each element of the design vector $\underline{\delta}$ is a number on the interval [0 2]. This effectively allows for the optimization of many sensors simultaneously, which includes making the decision about the types of sensors as well along with their location. This is more realistic and gives more freedom to the approach than predetermining how many sensors of each type one should include in $\underline{\delta}$.

Note that the optimal sensor placement methodology can also be readily applied to design a set of triaxial instead of uniaxial sensors. In this case the information from each triaxial sensor will be the combined information obtained from the three sensor components in each direction. The aforementioned concept can also be extended to design a combination of uniaxial (*e.g.*, transverse and vertical) and triaxial sensors by mapping the physical curved line with triaxial sensors placed on it to a parent element from 2 to 3. In this way the three type of sensors can efficiently be handled. However, the triaxial sensors will always be preferred to the transverse or vertical uniaxial sensors since the information gain from a uniaxial sensor placed in an optimal position will always be less than the information gain from a triaxial sensor placed at the same position. To favor a uniaxial sensor in relation to a triaxial sensor one has to introduce additional constrains that penalize the placement of triaxial sensors by taking into account the extra cost of the sensor and the information gain a triaxial sensor will provide in relation to a uniaxial sensor. However, this complicates the optimization, with the subject falling outside the scope of the present work. The previous concepts can be extended to design a combination of different uniaxial and triaxial sensor types such as acceleration, displacement and strain sensors.

5.2.2 Numerical Results for Spatially Uncorrelated Prediction Error Model

An uncorrelated prediction error model is used with diagonal covariance matrix $\Sigma(\underline{\delta};\underline{\sigma}) = \sigma^2 I_{N_0}$, where $I_{N_0} \in R^{N_0 \times N_0}$ is the identity matrix, with the value of the single prediction error parameter chosen to be $\sigma = 0.01$. A Gaussian prior with relatively large uncertainties is used. As a result, the posterior covariance matrix $Q_L(\underline{\delta};\underline{\sigma})$ is non-singular and the design can proceed for any number of sensors. The covariance matrix of the Gaussian prior is set to $S = 10^3 I_m$, with $s_1^2 = \cdots = s_m^2 = 10^3$.

Results for up to $N_0 = 9$ sensors are first obtained. Note that in this case the number of sensors is less than the number of modes ($m = 10$) and so the FIM is singular. The FSSP method is used to obtain the optimal sensor locations. It should be noted, however, that the sensor locations obtained by the heuristic FSSP method are verified that are the global optima, also obtained by the CMA-ES global optimizer[27].

The optimal location of the first sensor corresponds to the minimum of the information entropy. The information entropy as a function of the location of the sensor is drawn in Figure 3(A) at the parent domain. It can be seen that there are 9 local minima. Figure 3(B) shows the contour plots of the information entropy as a function of two sensor locations in the parent domain. A large number of local optima is also observed (blue color). The number of optima are expected to increase as the dimension of the design space increases. Figures 3(A) and 3(B) confirm that there are a large number of local optima and so gradient-based optimization methods will be trapped to a local optimum and will not be able to obtain a global optimum. Stochastic algorithms such as CMA-ES have much higher chances to pinpoint the global optimum.

For the case of optimizing the location of the first sensor, a vertical sensor was obtained rather than a transverse one. The two minima at 1.58 and 1.91 in the parent domain in Figure 3(A) are smaller than all the rest, which implies that for the 1st sensor it is best to be a vertical sensor in one of these two locations which correspond to distances on the bridge of 310 m and 487 m, respectively, from the left end. The minimum at 1.91 (487 m) is slightly smaller, but the difference is negligible for practical purposes.

Another interesting observation in Figure 3(A) is that at the two ends of the bridge (at points 0, 1, and 2 in the parent domain) the value of the posterior entropy is 48.72, which is exactly the information entropy

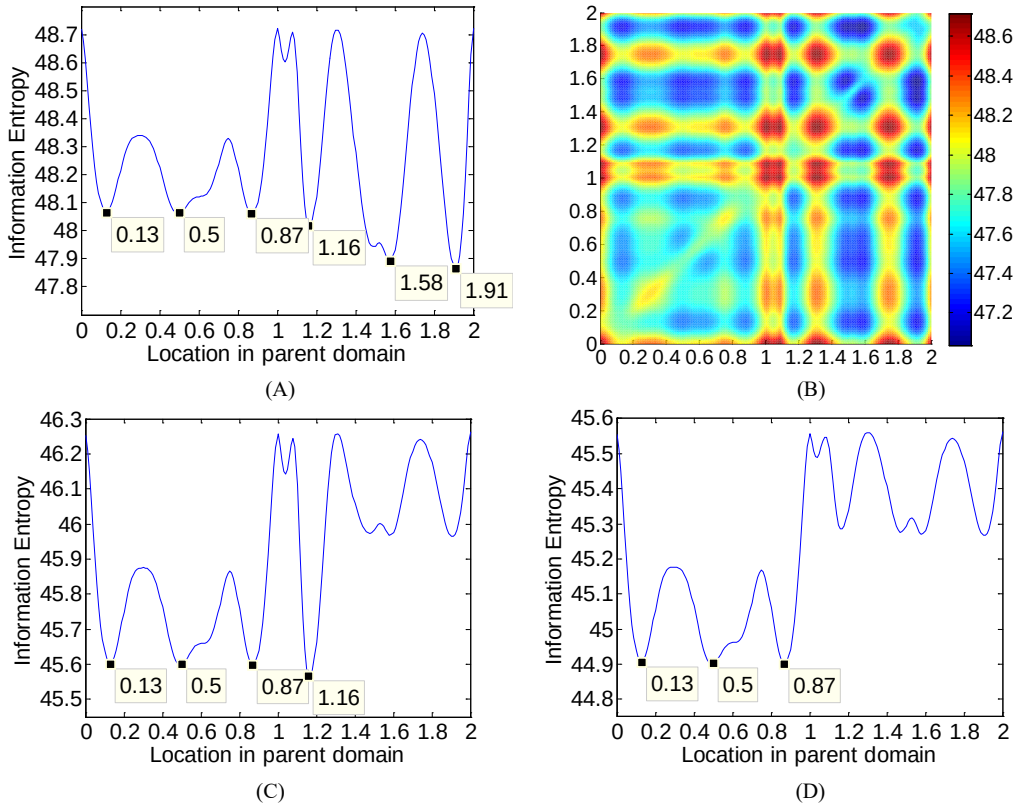

Figure 3. Information entropy vs. the location of a sensor in parent domain (A) 1st sensor, (B) 1st, and 2nd sensor (contour plots), (C) 4th sensor, and (D) 5th sensor.

of the Gaussian prior. This makes sense, because in these points the mode shapes have zero components and the FIM is zero, and therefore the only contribution to the posterior comes from the prior. There are also other points which result in the posterior entropy being almost equal to the prior entropy, which correspond to vertical sensors being placed in points of zero vertical response (locations 1.08, 1.3 and 1.74 in the parent domain) for all vertical mode shapes. These are points in the deck that are above the piers where the vertical motion of the bridge is almost restrained. As one would intuitively expect, the information gain from these designs (which is the difference between the prior and posterior entropies) is zero.

The information entropy as a function of the location of the fourth sensor in the parent domain given that the first three sensors have been placed in their optimal position is shown in Figure 3(C). Similar plot for the information entropy as a function of the position of the 5th sensor given that the first four sensors have been placed in their optimal position, is shown in Figure 3(D). The optimal locations of the first nine sensors are shown in Figures 4(A) and 4(B) for both the transverse and vertical sensors. Also, information of the optimal locations of sensors and the corresponding information entropy values is given in Table 1.

Note that the optimal location of the first two sensors is made up of the location of the global and the next local optimum predicted in Figure 3(A). Also, from the results in Figure 4(B) the first 4 sensors are vertical sensors. This is because, as can be seen from Figures 4(A) and 4(B), vertical modes have slightly higher displacements and therefore contribute more than the transverse modes to the FIM, and therefore to the posterior covariance matrix. Also the vertical modes have more "convenient" points where several modes have high responses compared to the transverse modes. These result in preferring the vertical modes compared to the transverse modes. Note that all modes are treated equally by selecting the prior uncertainty to be the same for all modal coordinates. Finally, results in Figure 4(A) suggest that the last 5 sensors (5th to 9th sensors) are selected to measure in the transverse direction.

From the results in Figure 3(C) of the information entropy as a function of the location of the 4th sensor, given that the first 3 sensors are placed at their optimal location, it is noticed that the vertical sensor at 85 m is

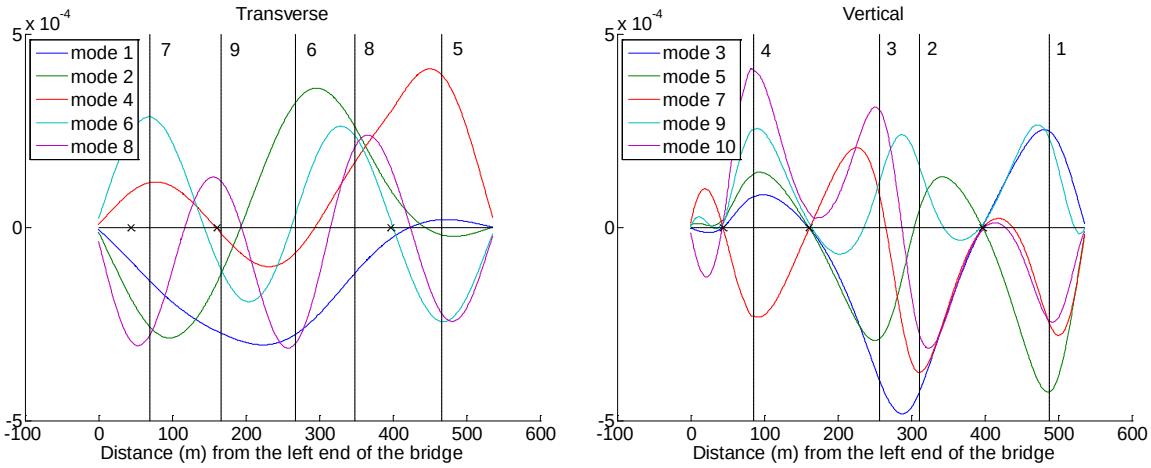

(A) (B)

Figure 4. Optimal locations of (A) transverse sensors, and (B) vertical sensors (Case of 9 sensors with uncorrelated prediction error). The symbol x denotes the location of the piers along the deck.

Table 1. Optimal location in the physical domain and minimum information entropy for the first nine sensors ($N_0 < m$). V = Vertical, T = Transverse.

Sensor	1	2	3	4	5	6	7	8	9
Type	V	V	V	V	T	T	T	T	T
Optimal Location (m)	487	310	257	85	466	267	69	348	166
Information Entropy	47.86	47.03	46.26	45.57	44.89	44.23	43.58	43.02	42.63

slightly preferred from the three transverse sensors at 69 m, 267 m, and 466 m since the minimum value of 45.57 in the information entropy for the vertical sensor is slightly smaller than the local minimum value of 45.58 for the information entropy for the three transverse sensors. From the results in Figure 3(D) of the information entropy as a function of the location of the 5th sensor, given that the first 4 sensors are placed at their optimal location, it can be observed that any of the locations 69, 267 and 466 m for a transverse sensor are candidates. These sensor locations are the optimal sensor locations for the 5th, 6th and 7th sensor. The optimal sensors for the 8th and 9th sensor are transverse ones, with optimal locations shown in Figure 4(A) and Table 1.

Observing the optimal sensor locations in relation to the mode shapes drawn in Figures 4(A) and 4(B), one should note that the results are reasonable for placing sensors in the suggested vertical or transverse locations since in these locations the mode shape components correspond, in general, to their higher values.

For up to nine sensors it is observed that placing two or more sensors in the same position corresponds to the worst sensor location. This is confirmed also by the contour plots in Figure 3(B) where the placing of the two sensors in the same position is not preferred (red colors). Also it is confirmed by the plots in Figure 3 where it is clear that when a new sensor location coincides with an already placed sensor location it gives large values of the information entropy as compared to the optimal one. So in the singular FIM case with $N_0 < m$, the problem of sensor clustering[16] due to uncorrelated prediction error does not occur.

The optimal location and type (transverse or vertical) of the next 11 sensors (10th to 20th) is also considered. The design is performed using the FSSP algorithm. However, for selected number of sensors, the accuracy of the results obtained from the FSSP algorithm is confirmed by running also the CMA-ES algorithm. Both algorithms provide the same estimates. The information entropy as a function of the location of the 10th sensor given that the first 9 sensors are placed at their optimal positions (shown in Table 1) is presented in Figure 5(A). Figure 5(B) gives similar information but for optimizing the location of the 19th sensor. The optimal sensor locations for the sensors from 10th to 20th, their type (vertical or transverse) and the minimum information entropy are also given in Table 2 and in Figure 6.

It is clear from Figure 5(A) that the optimal location of the 10th sensor coincides with the location of the 1st sensor. Actually the information entropy as a function of the location of the 10th sensor is qualitatively similar to the information entropy for one sensor in Figure 3(A)

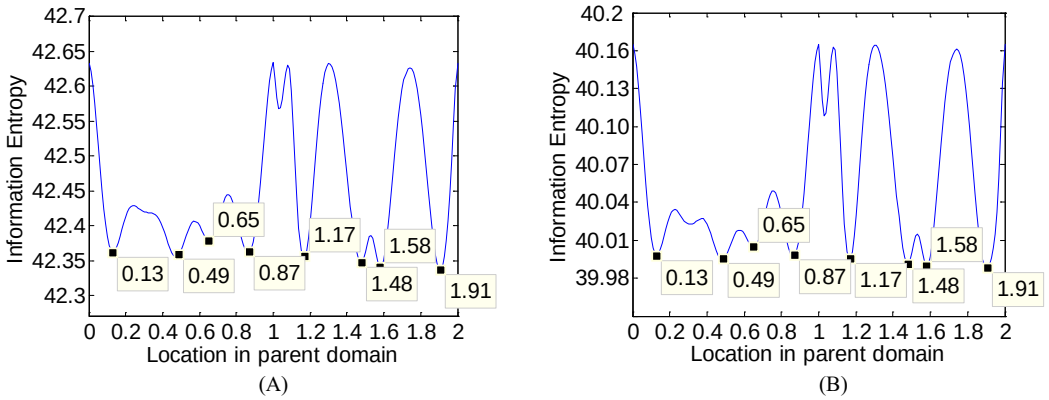

Figure 5. Information entropy vs. the location of a sensor in parent domain (A) 10th sensor, (B) 19th sensor.

Table 2. Optimal location in the physical domain and minimum information entropy for the 10th up to the 20th sensor ($N_0 \geqslant m$). V = Vertical, T = Transverse.

Sensor	10	11	12	13	14	15	16	17	18	19	20
Type	V	V	V	V	T	T	T	T	T	V	V
Optimal Location (m)	487	310	251	85	251	69	460	348	160	482	310
Information Entropy	42.33	42.04	41.75	41.47	41.19	40.91	40.64	40.39	40.17	39.98	39.80

as a function of its location. Comparing Figures 5(A) and 3(A), the local/global optimal appears at the same locations, suggesting that the optimal locations of the next nine sensors will be close to the optimal locations of the first nine sensors. This is confirmed by comparing also the results in Table 2 with the results in Table 1. Comparisons clearly demonstrate (see also Figure 6) that the optimal locations of the sensors 9th to 20th coincide or they are very close to the optimal locations estimated for the first 9 sensors. This sensor clustering is due to the incorrect assumption of the spatially uncorrelated prediction errors[16]. However, it seems that the sensor design obtained with uncorrelated prediction errors are very reasonable and intuitive for the first nine sensors which correspond to the case of singular FIM with $N_0 < m$. To correct the problem of sensor clustering for more than 9 sensors one has to introduce spatial correlation in the prediction errors.

5.2.3 Numerical Results for Spatially Correlated Prediction Error Model

A spatially correlated prediction error model is assumed next. For this the covariance $\Sigma(\underline{\delta};\underline{\sigma})$ of the prediction error at the sensor locations is selected to be non-diagonal with the (i,j) element of the form

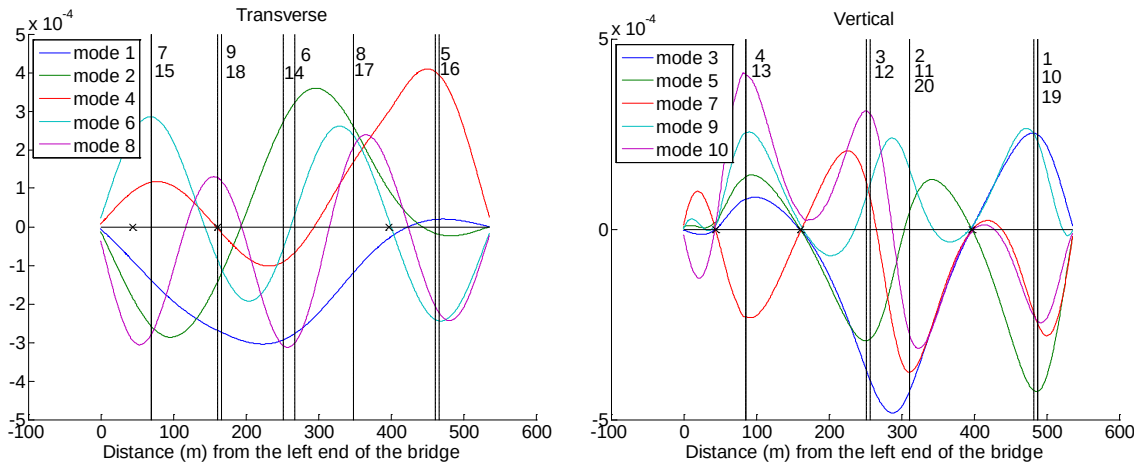

Figure 6. Optimal locations of (A) transverse sensors, and (B) vertical sensors (Case of 20 sensors with uncorrelated prediction error). The symbol x denotes the location of the piers along the deck.

$\Sigma_{ij}(\underline{\delta};\underline{\sigma}) = \sigma^2 R(\delta_i - \delta_j)$, where $R(\delta_i - \delta_j)$ is the spatial correlation structure of the prediction error, δ_i and δ_j are the locations of the i and j sensors, and σ^2 is the strength of the prediction error. An exponentially decaying correlation structure of the form $R(\delta_i - \delta_j) = \exp(-|\delta_i - \delta_j|/\lambda)$ is selected, where λ is the correlation length.

Since in this formulation we allow for each sensor to be either transverse or vertical, correlation is limited to sensors of the same type. That is, correlation exists between any two transverse sensors or any two vertical sensors, but not between a transverse and a vertical sensor. The described model allows for two different correlation length parameters (or correlation functions in general) to be used for the transverse and vertical sensors, respectively. In the numerical results that follow, the correlation parameters are chosen to be $\sigma = 0.01$ and $\lambda_{trans} = \lambda_{vert} = 10m$ or $\lambda_{trans} = \lambda_{vert} = 20m$.

Optimal sensor placement results for the correlated prediction error models are shown in Figure 7 for two different correlation length of 10 m and 20 m respectively. The Gaussian prior is selected to be the same as in the uncorrelated prediction error case. Results have been derived using the FSSP algorithm and their accuracy has been also confirmed for representative sensor cases using the CMA-ES algorithm. Comparing with the results of the uncorrelated case in Figure 6 it can be observed that the optimal sensor locations for the first 9 sensors are the same as the uncorrelated prediction error case. For more than 9 sensors, the sensor clustering problem is not present in the spatially correlated prediction error case. The optimal locations of sensors 10th to 20th are not close to the

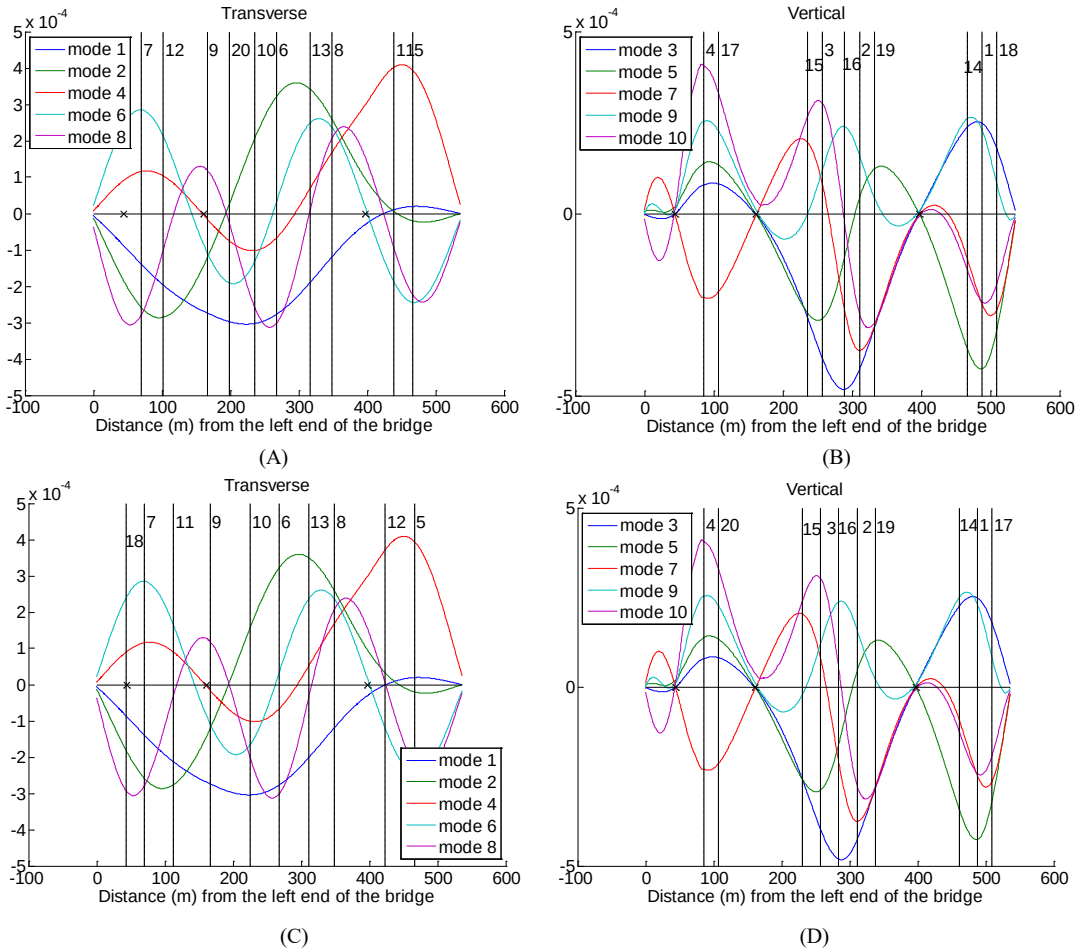

Figure 7. Optimal locations of (A) transverse sensors ($\lambda = 10m$), (B) vertical sensors ($\lambda = 10m$), (C) transverse sensors ($\lambda = 20m$), and (D) vertical sensors ($\lambda = 20m$) (Case of 20 sensors with spatially correlated prediction error). The symbol x denotes the location of the piers along the deck.

locations obtained for the first 9 sensors. In fact, they are more uniformly distributed in some of the areas of the bridge deck. Comparing Figures 7(A,B) with Figures 7(C,D) it can be observed that the spacing of the sensors tends to increase as one increases the correlation length from 10 m to 20 m. This is consistent with the theoretical results obtained by Papadimitriou and Lombaert[16].

In Figure 8 the optimal information entropy as a function of the number of sensors is shown for the uncorrelated and correlated prediction error cases and for 1 up to 30 sensors. The 0 sensor case corresponds to the case where no sensors are placed and so the information entropy is that of the Gaussian prior PDF. As expected, we notice that the optimal value of the information entropy for a given number of sensors decreases as the number of sensors increases. For up to 9 sensors the entropies are identical between the uncorrelated and correlated prediction error models. From the 10th sensor and on, the correlated prediction error models lead to more information entropy (less information) and this entropy increases with the correlation length. This is due to the fact that the information provided by neighbor sensors within the correlation length assumed is not significantly different and so this results in a drop of the total information for the same number of sensors. Also, the curves with high correlation suggest that the information provided by adding sensors in the structure is decreasing and eventually after a number of sensors there is no significant information offered by additional sensors. This plot can be used to decide on the number of sensors to be placed in the structure, given the correlation length. The uncorrelated prediction error models provide misleading results since continuing adding sensors in the structure has the effect of gaining additional information, independent of the number of added sensors, which is counter-intuitive. Finally, the CMA-ES algorithm is also used to design the optimal sensor locations and the resulting information entropy values for representative sensor cases, shown in Figure 8 for correlation length 20 m, match exactly the information entropy values obtained using the FSSP algorithm, confirming in this case the accuracy of FSSP algorithm.

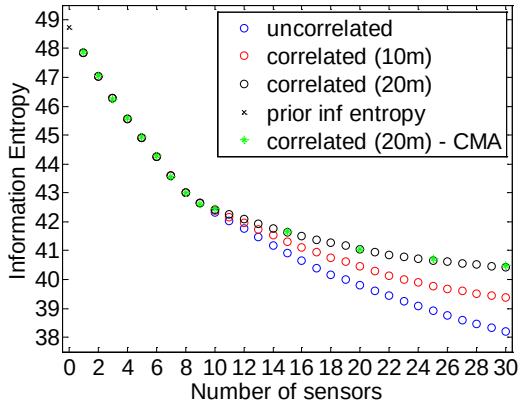

Figure 8. Optimal information entropy vs. number of sensors

5.3 Effect of Prior Uncertainty on Optimal Sensor Placement

The results obtained so far correspond to an isotropic Gaussian prior where all prior uncertainties in the parameters were selected to be the same. This gives equal weight to all parameters as far as the prior is concerned, so there is no preference of a specific mode over another. The Gaussian prior covariance matrix is a modelling choice that depends on user preference. Therefore, it can be fully manipulated according to the needs. Equation (19) suggests that by giving larger prior uncertainties to some specific modes we are essentially giving more weight in these modes in the selection of the optimal design. The insightful result from (19) states that a Gaussian prior can be used as a means to perform more sophisticated OED, where we give preference to some selected modes over others. Different Gaussian prior variances for the different modes get transferred to the posterior and result in different optimal designs, favoring the identification of modes with the largest prior variances. The Bayesian framework for OED provides the means to fully quantify this preference of some modes (or parameters for identification in general) over others through the prior.

In order to illustrate this, the simple case of one sensor is examined. We would like to give more weight to the identification of the modal coordinates of the transverse modes. For this we lower the variances of the bending modes from 1000 to 100, and we keep the variances of the transverse modes at 1000. The information entropy as a function of the position of the 1st sensor is shown in Figure 9(A). We see that the optimal design for the 1st sensor is now a transverse sensor in one of the already found optimal locations for transverse sensors, shown in Figure 3(D). In fact, the plot for one sensor in Figure 9(A) is now qualitatively very similar to the plot of the 5th sensor shown in Figure 3(D), where the first transverse sensor appears as optimal. With this change in the prior

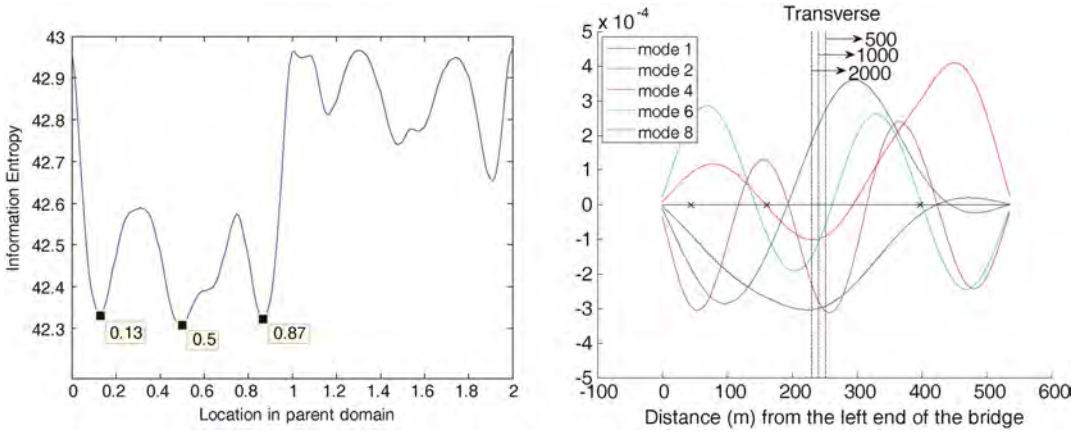

(A) (B)

Figure 9. (A) Information entropy of 1st sensor vs location in parent domain using Gaussian prior variance $s^2 = 1000$ for transverse modes and $s^2 = 100$ for vertical modes. (B) Optimal locations for 1st sensor for prior variance of 1st mode equal to 500, 1000 and 2000. All other prior variances equal to 100.

variances giving weight to the transverse modes, the optimal designs have a preference for the transverse sensors now to show up as the 1st sensor and not the 5th.

Consider next the case of giving preference to the first modal coordinate which is transverse. The design is performed by setting all prior variances, except the first, equal to 100, while we set the prior variance of the first modal coordinate to different values $s_1^2 = 300$, 500, 1000 and 2000. For $\sigma_1^2 = 300$ or for smaller values of s_1^2, the optimal sensor is selected to be a vertical sensor. For values of $s_1^2 = 500$, 100 and 2000, the transverse sensor is selected. The location of the transverse sensor for these higher values is shown in Figure 9(B). It is clear that increasing the value of s_1^2 the sensor is located closer to the location where the first mode has its maximum absolute deflection. This is consistent with the theoretical result in Section 4.2 which states that increasing the prior variance of the first mode gives more and more weight to the identification of the first mode, making it more important in the optimal sensor placement design.

5.4 Optimal Sensor Placement of Reference Sensors

The OED is next used to address the important problem of selecting the optimal location of a few reference sensors in a multiple sensor configuration set up experiment conducted with a limited number of reference and roving sensors in order to obtain the modal frequencies and assemble the mode shapes from the multiple setups. The number of reference sensors is in most cases significantly smaller than the number of modes to be identified. It is important in this case that the reference sensors, common in most setups, contain the maximum possible information for all modes that are planned to be identified. Wrong locations of the reference sensors may degrade the modal information for one or more modes, degrading the accuracy of the corresponding assembled mode shape since such accuracy is based solely on the information contained in the reference sensors.

The effectiveness of the methodology is illustrated by designing the optimal locations of one vertical and one transverse reference sensor for identifying the lowest 10 modes of the bridge. It is clear from the results in Figure 3(A) that the best location of the 1st sensor is at 487 m measuring along the vertical direction. This is also taken as the location of the vertical reference sensor. Figure 4(B) demonstrates that the design of the reference sensor at 487 m is rational since the deflection of all five vertical mode shapes is high. To design the location of the 1st transverse reference sensor one could use the results in Figure 9(A), obtained for the transverse modes after selecting the prior uncertainty to give in the optimal design preferential treatment to these modes over the vertical modes. It is clear that the transverse reference sensor can be selected as the location 268 m (parent location 0.5) that corresponds to the minimum information entropy in Figure 9(A). From Figure 4(A) it is seen that the transverse reference sensor location 268 m corresponds to high deflections of four out of the five transverse modes. One of the transverse modes has relatively small deflection, a problem that arises from the trade-off that has to be made in the design to get

maximum information from all five modes. A solution to this problem is to place a second transverse sensor on the structure at position 70 m (the second best local optimum in Figure 4(A)). In practice, using more reference sensors that the minimum required (two in this case) is a good way to make sure that important information from reference sensors will not be lost. Concluding, the vertical and transverse reference sensors in experiments with multi sensor configuration setups could be 487 m and 268 m (and/or 70 m), respectively.

6. Conclusions

An optimal sensor placement design for modal identification based on the expected K-L divergence as a measure of the information contained in the data is shown to be equivalent to the optimal sensor placement design based on the information entropy proposed by Papadimitriou[18]. Using non-uniform priors, the Bayesian OED allows for optimal sensor placement to be performed even for the case when the number of sensors is less than the number of identified modes. This is important when designing the optimal locations of a very small number of reference sensors for the purpose of assembling the mode shapes using reference and roving sensors in multiple sensor configuration setups. In this study the effect of the Gaussian prior on the optimal design was thoroughly investigated. Insightful analytical expressions were derived to show that larger uncertainty in the prior of a subset of modal coordinates can be used to give preference in this subset in the optimal design of the sensor locations. The prior variances for all modes to be identified can be altered to weight the importance of different modes in the design, favoring a number of modes against the rest of the modes. The prior is the users' choice and it can be used in different ways to achieve different results, which is one of the strengths of Bayesian OED.

The methodology was applied to a 537 m long reinforced concrete bridge in order to design the optimal sensor configuration for identifying the lowest 10 modes. The optimization was performed in the continuous space of the design variables, through appropriate mapping from the physical space to a parent domain. A large number of local optima were observed that result in a challenging optimization problem. The problem is overcome using computationally efficient heuristic FSSP algorithms. The accuracy of the FSSP algorithm was confirmed using the computationally demanding CMA-ES algorithm. A thorough investigation of the effect of correlated and uncorrelated prediction error models was also performed. The design for a smaller number of sensors than the number of modes was shown to be the same for spatially uncorrelated and correlated prediction error models. Rational and intuitive results were obtained. For more sensors than the number of modes the spatially correlated prediction error model gave intuitively reasonable results, avoiding sensor clustering observed for uncorrelated prediction error models.

The proposed method offers a useful decision tool for designing the sensor locations in a structure in order to obtain the maximum information for reliable modal identification of civil infrastructures and industrial facilities using vibration measurements.

Conflict of Interest and Funding

No conflict of interest was reported by the authors. This research has been implemented under the "ARISTEIA" Action of the "Operational Programme Education and Lifelong Learning" and was co-funded by the European Social Fund (ESF) and Greek National Resources.

References

1. Simoen E, Moaveni B, Conte J P, *et al*., 2013, Uncertainty quantification in the assessment of progressive damage in a 7-story full-scale building slice. *Journal of Engineering Mechanics – ASCE*, vol.139(12): 1818–1830. http://dx.doi.org/10.1061/(ASCE)EM.1943-7889.0000610
2. Beck J L and Katafygiotis L S, 1998, Updating models and their uncertainties. I: Bayesian statistical framework. *Journal of Engineering Mechanics – ASCE*, vol.124(4): 455–461. http://dx.doi.org/10.1061/(ASCE)0733-9399(1998)124:4(455)
3. Yuen K V, 2012, Updating large models for mechanical systems using incomplete modal measurement. *Mechanical Systems and Signal Processing*, vol.28: 297– 308. http://dx.doi.org/10.1016/j.ymssp.2011.08.005
4. Yuen K V, 2010, *Bayesian Methods for Structural Dynamics and Civil Engineering*, John Wiley and Sons: NJ. http://dx.doi.org/10.1002/9780470824566
5. Lam H, Katafygiotis L and Mickleborough N, 2004, Application of a statistical model updating approach on phase I of the IASC-ASCE structural health monitoring benchmark study. *Journal of Engineering Mechanics – ASCE*, vol.130(1): 34–48. http://dx.doi.org/10.1061/(ASCE)0733-9399(2004)130:1(34)
6. Vanik M, Beck J and Au S, 2000, Bayesian probabilistic approach to structural health monitoring, *Journal of En-*

gineering Mechanics – ASCE, vol.126(7): 738–745. http://dx.doi.org/10.1061/(ASCE)0733-9399(2000)126:7(738)
7. Li D, 2011, *Sensor placement methods and evaluation criteria in structural health monitoring*, PhD. thesis, University of Siegen, Siegen.
8. Kammer D C, 1991, Sensor placements for on-orbit modal identification and correlation of large space structures, *Journal of Guidance, Control and Dynamics*, vol.14(2): 251–259. http://dx.doi.org/10.2514/3.20635
9. Kammer D C, 1992, Effects of noise on sensor placement for on-orbit modal identification of large space structures, *Journal of Dynamic Systems, Measurements and Control*, vol.114(3): 436–443. http://dx.doi.org/10.1115/1.2897366
10. Li D S, Li H N and Fritzen C P, 2009, A note on fast computation of effective independence through QR downdating for sensor placement. *Mechanical Systems and Signal Processing*, vol.23(4): 1160–1168. http://dx.doi.org/10.1016/j.ymssp.2008.09.007
11. Shah P C and Udwadia F E, 1978, A methodology for optimal sensor locations for identification of dynamic systems, *Journal of Applied Mechanics*, vol.45(1): 188–196. http://dx.doi.org/10.1115/1.3424225
12. Udwadia F, 1994, Methodology for optimal sensor locations for parameter identification in dynamic systems, *Journal of Engineering Mechanics* (*ASCE*), vol.120(2): 368–390. http://dx.doi.org/10.1061/(ASCE)0733-9399(1994)120:2(368)
13. Papadimitriou C, Beck J L and Au S K, 2000, Entropy-based optimal sensor location for structural model updating, *Journal of Vibration and Control*, vol.6(5):-781–800. http://dx.doi.org/10.1177/107754630000600508
14. Yuen K V, Katafygiotis L S, Papadimitriou C, *et al*., 2001, Optimal sensor placement methodology for identification with unmeasured excitation. *Journal of Dynamic Systems, Measurement and Control*, vol.123(4): 677–686. http://dx.doi.org/10.1115/1.1410929
15. Ye S Q and Ni Y Q, 2012 Information entropy based algorithm of sensor placement optimization for structural damage detection. *Smart Structures and Systems*, vol. 10(4–5): 443–458. http://dx.doi.org/10.12989/sss.2012.10.4_5.443
16. Papadimitriou C and Lombaert G, 2012, The effect of prediction error correlation on optimal sensor placement in structural dynamics. *Mechanical Systems and Signal Processing*, vol.28: 105–127. http://dx.doi.org/10.1016/j.ymssp.2011.05.019
17. Kammer D C, 2005, Sensor set expansion for modal vibration testing. *Mechanical Systems and Signal Processing*, vol.19(4): 700–713. http://dx.doi.org/10.1016/j.ymssp.2004.06.003
18. Papadimitriou C, 2004, Optimal sensor placement methodology for parametric identification of structural systems. *Journal of Sound and Vibration*, vol.278(4): 923–947. http://dx.doi.org/10.1016/j.jsv.2003.10.063
19. Stephan C, 2012, Sensor placement for modal identification. *Mechanical Systems and Signal Processing*, vol.27: 461–470.http://dx.doi.org/10.1016/j.ymssp.2011.07.022
20. Papadimitriou D and Papadimitriou C, 2015, Optimal sensor placement for the estimation of turbulence model parameters in CFD. *International Journal for Uncertainty Quantification*, vol.5(6): 545–568. http://dx.doi.org/10.1615/Int.J.UncertaintyQuantification.2015015239
21. Leyder C, Ntertimanis V K, Chatzi E, *et al*., 2015, Optimal sensor placement for the modal identification of an innovative timber structure. *Volume 1st ECCOMAS Thematic Conference on Uncertainty Quantification in Computational Sciences and Engineering, UNCECOMP 2015*, pp. 467–476, National Technical University of Athens.
22. Leyder C, Chatzi E, Frangi A, *et al*., 2016, Comparison of optimal sensor placement algorithms via implementation on an innovative timber structure, IALCCE Conference, *Fifth International Symposium on Life-Cycle Civil Engineering (IALCCE 2016)*, 16–19 October, 2016, Delft, The Netherlands.
23. Chow H M, Lam H F, Yin T, *et al*., 2011, Optimal sensor configuration of a typical transmission tower for the purpose of structural model updating. *Structural Control and Health Monitoring*, vol.18(3): 305–320. http://dx.doi.org/10.1002/stc.372
24. Yuen K V and Kuok S C, 2015, Efficient Bayesian sensor placement algorithm for structural identification: a general approach for multi-type sensory systems. *Earthquake Engineering and Structural Dynamics*, vol.44(5):757–774. http://dx.doi.org/10.1002/eqe.2486
25. Lindley D V, 1956, On a measure of the information provided by an experiment. *The Annals of Mathematical Statistics*, vol.27: 986–1005. http://dx.doi.org/10.1214/aoms/1177728069
26. Huan X and Marzouk Y M, 2013, Simulation-based optimal Bayesian experimental design for nonlinear systems. *Journal of Computational Physics*, vol.232(1): 288– 317. http://dx.doi.org/10.1016/j.jcp.2012.08.013
27. Hansen N, Muller S D, and Koumoutsakos P, 2003, Reducing the time complexity of the derandomized evolution strategy with covariance matrix adaptation (CMA-ES). *Evolutionary Computation*, vol.11(1): 1–18. http://dx.doi.org/10.1162/106365603321828970
28. Chaloner K and Verdinelli I, 1995, Bayesian experimental design: a review. *Statistical Science*, vol.10(3): 273– 304. http://dx.doi.org/10.1214/ss/1177009939

Author Guidelines

Before your submission, please check that your manuscript has been prepared in accordance to the step-by-step instructions for submitting a manuscript to our online submission system. We recommend that you keep this page open for your reference as you move through the submission process.

If there are any differences in author guidelines between the print and online version, it is recommended that authors refer to the online version for use.

Manuscript Format

Your manuscript should be in MS Word format. You are advised to download the document, Instructions for Typesetting Manuscript, as a template or for more details on preparing your submissions for consideration.

All manuscripts must be written in clear, comprehensible English. Both American and British English are acceptable. Usage of non-English words should be kept to a minimum and all must be italicized (except for e.g. and i.e.) If you have concerns about the level of English in your submission, please ensure that it is proofread before submission by a native English speaker or a scientific editing service.

Cover letter

All submissions should include a cover letter as a separate file. A cover letter should contain a brief explanation of what was previously known, the conceptual advancement with the findings and its significance to broad readership. The cover letter is confidential and will be read only by the editors. It will not be seen by reviewers.

Title

The title should capture the conceptual significance for a broad audience. The title should not be more than 50 words and should be able to give readers an overall view of the paper's significance. Titles should avoid using uncommon jargons, abbreviations and punctuation.

List of Authors

The names of authors must be spelled out rather than set in initials with their affiliations footnoted. Authors should be listed according to the extent of their contribution, with the major contributor listed first. All corresponding authors (maximum 2) should be identified with an asterisk. Affiliations should contain the following core information: department, institution, city, state, postal code, and country. For contact, email address of only one corresponding author is expected within the manuscript. Please note that all authors must see and approve the final version of the manuscript before submitting.

Abstract

Articles must include an abstract containing a maximum of 200 words. The purpose of abstract is to provide sufficient information for a reader to determine whether or not to proceed to the full text of the article. After the abstract, please give 5-8 key words; please avoid using the same words as those already used in the title.

Section Headings

Please number all section headings, subheadings and sub-subheadings. Use boldface to identify major headings (e.g. 1, 2, 3, etc.) and subheadings (e.g. 1.1, 1.2, 2.1, 2.2 etc.) For the sub-subheadings, please distinguish it further using non-boldface numbers in parenthesis (e.g. (1), (2), (3), etc.)

Introduction

Introduction should provide a background that gives a broad readership an overall outlook of the field and the research performed. It tackles a problem and states its important regarding with the significance of the study. Introduction can conclude with a brief statement of the aim of the work and a comment about whether that aim was achieved.

Materials and Methods

This section provides the general experimental design and methodologies used. The aim is to provide enough detail to for other investigators to fully replicate your results. It is also required to facilitate better understanding of the results obtained. Protocols and procedures for new methods must be included in detail to reproduce the experiments.

Ethics

Ethics information, including IACUC permit numbers and/or IRB name, if applicable. This information should be included in a subheading labeled "Ethics Statement" in the "Methods" section of your manuscript file, in as much detail as possible.

Results

This section can be divided into subheadings. This section focuses on the results of the experiments performed.

Discussion

This section should provide the significance of the results and identify the impact of the research in a broader context. It should not be redundant or similar to the content of the results section.

Conclusion

Please use the conclusion section for interpretation only, and not to summarize information already presented in the text or abstract.

Conflict of Interest

All authors are required to declare all activities that have the potential to be deemed as a source of competing interest in relations to their submitted manuscript. Examples of such activities could include personal or work-related relationships, events, etc. Authors who have nothing to declare are encouraged to add "No conflict of interest was reported by all authors" in this section.

Funding

Authors should declare all financial and non-financial support that have the potential to be deemed as a source of competing interest in relations to their submitted manuscript in this section. Financial supports are generally in the form of grants, royalties, consulting fees and more. Examples of non-financial support could include the following: externally-supplied equipments/biological sources, writing assistance, administrative support, contributions from non-authors etc.

Appendix

This section is optional and is for all materials (e.g. advanced technical details) that has been excluded from the main text but remain essential to readers in understanding the manuscripts. This section is not for supplementary figures. Authors are advised to refer to the section on 'Supplementary figures' for such submissions.

Text

The text of the manuscript should be in Microsoft Word or Latex. The length of the manuscript cannot be more than 50000 characters (inclusive of spaces) or approximately 7000 words.

Nomenclature for genes and proteins

This journal aims to reach researchers all over the globe. Hence, for both reviewers' and readers' ease in comprehension, authors are highly encourage to use the appropriate gene and protein nomenclature. Authors may prefer to utilize resources such as http://www.ncbi.nlm.nih.gov/gene

Figures

Authors should include all figures into the manuscript and submit it as 1 file in the OJS system. Reference to the Instructions for Typesetting manuscript is strongly encouraged. Figures include photographs, scanned images, graphs, charts and schematic diagrams. Figures submitted should avoid unnecessary decorative effects (e.g. 3D graphs) as well as be minimally processed (e.g. changes in brightness and contrast applied uniformly for the entire figure). It should also be set against a white background. Please remember to label all figures (e.g. axis etc.) and add in captions (below the figure) as required. These captions should be numbered (e.g. Figure 1, Figure 2, etc.) in boldface. All figures must have a brief title (also known as caption) that describes the entire figure without citing specific panels, followed by a legend defined as description of each panel. Please identify each panel with uppercase letters in parenthesis (e.g. A, B, C, etc.)

The preferred file formats for any separately submitted figure(s) are TIFF or JPEG. All figures should be legible in print form and of optimal resolution. Optimal resolutions preferred are 300 dots per inch for RBG coloured, 600 dots per inch for greyscale and 1200 dots per inch for line art. Although there are no file size limitation imposed, authors are highly encouraged to compress their figures to an ideal size without unduly affecting legibility and resolution of figures. This will also speed up the process of uploading in the submission system if necessary.

The Editor-in-Chief and Publisher reserve the right to request from author(s) the high-resolution files and unprocessed data and metadata files should the need arise at any point after manuscript submission for reasons such as production, evaluation or other purposes. The file name should allow for ease in identifying the associated manuscript submitted.

Tables, lists and equations

Tables, lists and equations must be submitted together with the manuscript. Likewise, lists and equations should be properly aligned and its meaning clear to readers. Tables created using Microsoft Word table function are preferred. Place each table in your manuscript file right after the paragraph in which it is first cited. Do not submit your tables in separate files. The tables should include a concise but sufficiently explanatory title at the top. Vertical lines should not be used to separate columns. Leave some extra space between the columns instead. All tables should be based on three horizontal lines to separate the caption, header and body. A few additional horizontal lines MAY be included as needed (example below). Any explanations essential to the understanding of the table should be given in footnotes at the bottom of the table. SI units should be used.

Supplementary information

This section is optional and contains all materials and figures that have been excluded from the entire manuscript. These information are relevant to the manuscript but remains non-essential to readers' understanding of the manuscript's main content. All supplementary information should be submitted as a separate file in Step 4 during submission. Please ensure the names of such files contain 'suppl. info'.

In-text citations

Reference citations in the text should be numbered consecutively in superscript square brackets. Some examples:

1. Negotiation research spans many disciplines[3,4].

2. This result was later contradicted by Becker and Seligman[5].

3. This effect has been widely studied[1−3,7].

Personal communications and unpublished works can only be used in the main text of the submission and are not to be placed in the Reference section. Authors are advised to limit such usage to the minimum. They should also be easily identifiable by stating the authors and year of such unpublished works or personal communications and the word 'Unpublished' in parenthesis, E.g. (Smith J, 2000, Unpublished)

References

This section is compulsory and should be placed at the end of all manuscripts. Do not use footnotes or endnotes as a substitute for a reference list. The list of references should only include works that are cited in the text and that have been published or accepted for publication. Personal communications and unpublished works should be excluded from this section.

For references in reference list, all authors must be stated. Authors referenced are listed with their surname followed by their initials. All references should be numbered (e.g. 1. 2. 3. etc.) and sequenced according to the order it appears as an in-text citation. References should follow the following pattern: Author(s) followed by year of publication, title of publication, full journal name in italics, volume number, issue number in parenthesis, page range and lastly the DOI (if applicable). If the referred article has more than three authors, list only the first three authors and abbreviate the remaining authors to italicized 'et al.' (meaning: "and others").

The upper limitation of Reference total amount is 100, or author will be asked to revise and resubmit the manuscipt.

Journal

Journal article (print) with one to three authors
Younger P, 2004, Using the internet to conduct a literature search, Nursing Standard, vol.19(6): 45-51.

Journal article (print) with more than three authors
Gamelin FX, Baquet G, Berthoin S, et al. 2009, Effect of high intensity intermittent training on heart rate variability in prepubescent children, European Journal of Applied Physiology, vol.105: 731738.

Journal article (online) with one to three authors
Jackson D, Firtko A and Edenborough M, 2007, Personal resilience as a strategy for surviving and thriving in the face of workplace adversity: a literature review, Journal of Advanced Nursing, vol.60(1): 19.

Journal article (online) with more than three authors
Hargreave M, Jensen A, Nielsen TSS, et al. 2015, Maternal use of fertility drugs and risk of cancer in childrenA nationwide population-based cohort study in Denmark, International Journal of Cancer, vol.136(8): 19311939. http://dx.doi.org/10.1002/ijc.29235.

Book

Book with one to three authors
Schneider Z, Whitehead D and Elliott D, 2007, Nursing and midwifery research: methods and appraisal for evidence-based practice, 3rd edn, Elsevier Australia, Marrickville, NSW.

Book with more than three authors
Davis M, Charles L, Curry MJ, et al. 2003, Challenging spatial norms, Routledge, London.

Chapter or Article in Book
Knowles MS 1986, Independent study, in Using learning contracts, Jossey-Bass, San Francisco, 8996.

Others

Proceedings of meetings and conference papers
Chang SS, Liaw L and Ruppenhofer J (eds) 2000, Proceedings of the twenty-fifth annual meeting of the Berkeley Linguistics Society, February 1215, 1999: general session and parasession on loan word phenomena. Berkeley Linguistics Society, Berkeley.

Conference proceedings (from electronic database)
Bukowski RM, 2009, Prognostic factors for survival in metastatic renal cell carcinoma: update 2008, Innovations and challenges in renal cancer: proceedings of the third Cambridge conference, Cancer, vol. 115 (10): 2273, viewed 19 May 2009, Academic OneFile database.

Online Document with author names
Este J, Warren C, Connor L, et al. 2008, Life in the clickstream: the future of journalism, Media Entertainment and Arts Alliance, viewed 27 May 2009.

Online Document without author name
Developing an argument n.d., viewed March 30 2009, ¡http://web.princeton.edu/sites/writing/Writing_ Center/WCWritingResources.htm¿

Thesis/Dissertation
Gale L, 2000, The relationship between leadership and employee empowerment for successful total quality management, thesis, University of Western Sydney, viewed 31 March 2009, Australasian Digital Thesis database.

Standard
Standards Australia Online, 2006, Glass in buildings: selection and installation, AS 12882006, amended 31

January 2008, viewed 19 May 2009, SAI Global database.

Government Report
National Commission of Audit, 1996, Report to the Commonwealth Government, Australian Government Publishing Service, Canberra.

Government report (online)
Department of Health and Ageing, 2008, Ageing and aged care in Australia, viewed 10 November 2008.

No author
Guide to agricultural meteorological practices 1981, 2nd edn, Secretariat of the World Meteorological Organization, Geneva.

Note: When referencing an entry from a dictionary or an encyclopedia with no author there is no requirement to include the source in the reference list. In these cases, only cite the title and year of the source in-text. For an authored dictionary/encyclopedia, treat the source as an authored book.

Submission Preparation Checklist

As part of the submission process, authors are required to check off their submission's compliance with all of the following items, and submissions may be returned to authors that do not adhere to these guidelines.
1. I have read and understood all policies mentioned for this journal.
2. The submission has not been previously published, nor is it before another journal for consideration (or an explanation has been provided in Comments to the Editor).
3. Where available, URLs for the references have been provided.
4. The text is single-spaced; uses a 12-point font; and all illustrations, figures, and tables are placed within the text at the appropriate points, rather than at the end.
5.The text adheres to the stylistic and bibliographic requirements outlined in the Author Guidelines.
6. If submitting to a peer-reviewed section of the journal, the instructions in Ensuring a Blind Review have been followed.

Focus and Scope

The Journal of Smart Cities offers a multidisciplinary forum for publishing original research in the area of smart cities, bringing together scholars from the fields of engineering, urban planning, computer science, and information and knowledge management. The Journal will serve as an international platform by sharing the latest research achievements on smart cities globally, offering a comprehensive access to researchers and the academic communities.

The main objectives of the Journal are to promote research for the improvement of all sub-systems of cities, including urban infrastructure, construction, mobility, energy saving and renewable energy, health and social care, safety in the public space, work and innovation, and make the city easily accessible, effective, efficient, and an attractive place to live. Information and communication technologies, the Internet, and embedded devices into the physical space of cities is a means to achieve these objectives, which are mainly realized through the empowerment of city institutions, organizations, citizens, and end-users to make better, more informed, and intelligent decisions.

About the Publisher

Urban Development Scientific Publishing Pte. Ltd (UDS publishing). UDS publishing was founded in Singapore in 2017. With Branch Office located in Beijing, UDS publishing provides an international, pluralistic and globally viewpoint to focus on all related topics among urban construction and developing issues. At this moment, UDS Publishing operate six journals in urban construction category which acquired from Whioce (founded in 2014), Piscomed (founded in 2015) and Universe Publishing(founded in 2011).

Editorial Office

Urban Development Scientific Publishing Pte Ltd.

6 Eu Tong Sen Street #10-08. The Central Singapore 059817

Website: www.udspub.com

Journal of Smart Cities is an independent open access journal published by Urban Development Scientific Publishing Pte. Ltd.

URBAN DEVELOPMENT SCIENTIFIC PUBLISHING PTE. LTD.

ISSN 2382-641X

9 772382 641218

Print Version UDS 75.00